Nanoscale Electron, Phonon and Spin Transport in Thermoelectric Materials

by

Bolin Liao

Submitted to the Department of Mechanical Engineering in partial fulfillment of the requirements for the degree of

Doctor of Philosophy

at the

MASSACHUSETTS INSTITUTE OF TECHNOLOGY

June 2016

Author..... Signature redacted .....
Department of Mechanical Engineering
March 31, 2016

Certified by..... Signature redacted .....
Gang Chen
Carl Richard Soderberg Professor of Power Engineering
Thesis Supervisor

Accepted by..... Signature redacted
Rohan Abeyaratne
Chairman, Department Committee on Graduate Students

Nanoscale Electron, Phonon and Spin Transport in Thermoelectrics

by
Bolin Liao

Submitted to the Department of Mechanical Engineering
on March 31, 2016, in partial fulfillment of the
requirements for the degree of
Doctor of Philosophy

Abstract

Climate change is among the most critical challenges that are facing the human race in the 21st century. One of the major factors that leads to climate change is the increasing consumption of fossil fuels, driven by industrialization and economic growth at an unprecedented pace. For a secure and sustainable future of energy and the environment, new clean and efficient energy technologies are in urgent need. Thermoelectric materials are a group of materials that can directly convert heat into electricity. Being solid state, clean, reliable and without moving parts, thermoelectric energy conversion holds great promise as a candidate technology to harvest energy from thermal sources, such as the sun and terrestrial heat sources, as well as improve the efficiency of existing energy systems by recycling the inevitable waste heat. The bottleneck that prevents large-scale deployment of thermoelectric modules so far, however, is the relatively low efficiency and high cost.

A good thermoelectric material needs to conduct electricity well and conduct heat poorly to attain high efficiency. Remarkable progress has been made in the past decade to decouple the charge and heat transport and thus improve the material performance. Most of the progress has been based on a more detailed understanding of the transport and interaction of fundamental energy carriers, such as electrons and phonons in most semiconductors, and magnons in magnetic materials. These understandings have been achieved through the development of both first-principles simulations and experimental spectroscopic tools, in particular for phonon transport and phonon-phonon interaction, which have enabled calculations and measurements at the single-phonon-mode level. Information gained from these studies formed the foundation

of the successful engineering efforts of designing nanostructured thermoelectric materials. Although the nanostructuring approach has been able to reduce the thermal conductivity of thermoelectric materials down to proximity of the amorphous limit, it has been realized by the community that further improvement of thermoelectric materials requires breakthroughs in boosting the electrical transport properties, including the electrical conductivity and the Seebeck coefficient. Despite several existing strategies, a prerequisite for systematic improvement is, again, insight into the transport and interaction of fundamental carriers, particularly involving electrons, at the single-mode level. This insight has largely remained lacking in terms of electrons, both on the simulation side and on the experimental side.

This thesis aims to develop both simulation and experimental tools to study nanoscale electron, phonon and magnon transport and their interactions, with a particular emphasis on understanding the electron-phonon interaction at the single-mode level. This is among the most important forms of carrier interactions and determines the intrinsic electron transport properties of most conductors. Regarding phonon transport, we applied first-principles lattice dynamics to study phonon-phonon interaction and lattice thermal conductivity in a strongly-correlated thermoelectric compound $FeSb_2$. On electron-phonon interactions, we studied from first-principles the intrinsic electrical transport properties of phosphorene, which are limited by electron-phonon interactions, analyzed its anisotropy and evaluated its potential as a thermoelectric material; we studied how free carriers can in turn scatter phonons through the electron-phonon interaction and reduce the lattice thermal conductivity; to verify this finding, we designed an ultrafast photoacoustic spectroscopic technique to directly detect the damping of a single phonon mode due to electron-phonon interaction. On phonon-magnon interactions, we applied the coupled Boltzmann equation to analyze coupled phonon-magnon diffusion and proposed a novel magnon cooling effect. These fundamental discoveries can potentially lead to new design principles for more efficient thermoelectric materials in the future.

Thesis Supervisor: Gang Chen

Title: Carl Richard Soderberg Professor of Power Engineering

Acknowledgement

This 6-year journey towards a PhD at MIT is long, and would have been excruciating, if not impossible, without the help, support and guidance of my mentors, teachers, friends and family. I want to thank my thesis advisor, Prof. Gang Chen, for his unconditional support and limitless patience. He is so passionate about research, but also empathetic and patient when I hit obstacles. He has great vision and deep understanding of our research field, but also has the flexibility and an open mind to grant me the freedom to explore my own interests and provide guidance when I get lost in uncharted land. He has taken incredible amount of responsibilities on his shoulders, but students are always his top priorities no matter how busy he gets. As an outstanding scholar, and more importantly, a great mentor, Gang is the role model for me and has set up very high standards that I will try hard in my lifetime to reach. I want to thank Prof. Mildred Dresselhaus, Prof. Caroline Ross and Prof. Nicholas Fang for serving on my thesis committee, and providing invaluable advice and support all along the way. I want to thank my former and current colleagues in the NanoEngineering group, especially Mona Zebarjadi, Keivan Esfarjani, Shuo Chen, Wei-Chun Hsu, George Ni, Maria Luckyanova, Kimberlee Collins, Zhiting Tian, Sangyeop Lee, Jonathan Tong, Kenneth McEnaney, Daniel Kraemer, James Loomis, Bo Qiu, Yuan Yang, Jiawei Zhou and Mingda Li, for their friendship and helping hands that I can always turn to. On the ultrafast photoacoustic spectroscopy experiment, I want to thank Prof. Keith Nelson in the MIT Chemistry Department for kindly allowing me to use the setup in his lab, and Alexei Maznev and Doug Shin to help me get familiar with the setup. I am also indebted to Prof. Zhifeng Ren and his group at University of Houston for numerous collaborations. I want to thank Kurt Broderick in the MIT MTL for helping me with microfabrications, and Mark Belanger in Edgerton Student Machine Shop for helping me with machining. I want to thank my friend Ling Qin and Jonathan Chang at Harvard University for their long-time friendship and support. I appreciate funding support from S^3TEC, a DOE EFRC center, and AFOSR MURI through Ohio State University.

I am the single child in my family, and have only been home at most three weeks a year since I left home for college 10 years ago. I want to thank my parents for their unconditional love and understanding, without which any of my achievements today is simply impossible. Last but not the least, I want to thank my wonderful soul mate, Yangying Zhu, who has generously shared her life with me, has dragged me out of the lab at times and shown me the greater colorful world, has stood by my side whether happiness or frustration comes by, has brought me joy and enlightenment of classical music, and has transformed me into a better man with her empathy and love.

Table of Contents

List of Figures

List of Tables

Chapter 1

Introduction

1.1 Basics of Thermoelectrics

The possibility of converting thermal energy directly to electricity holds promise of improving the efficiencies of current power systems as well as future sustainable energy systems[1]. Solid-state thermoelectric (TE) materials[2] can be used for direct heat to electricity conversion via the celebrated Seebeck effect, where a temperature gradient drives the thermal diffusion of charge carriers, giving rise to a counterbalancing electrical voltage. The reverse (Peltier) effect, where a drift electrical current carries heat along, can deliver cooling power without any moving parts or (potentially hazardous) working fluids[3]. Attractive as it is, the application of thermoelectrics (TEs) has long been limited by their low efficiency.

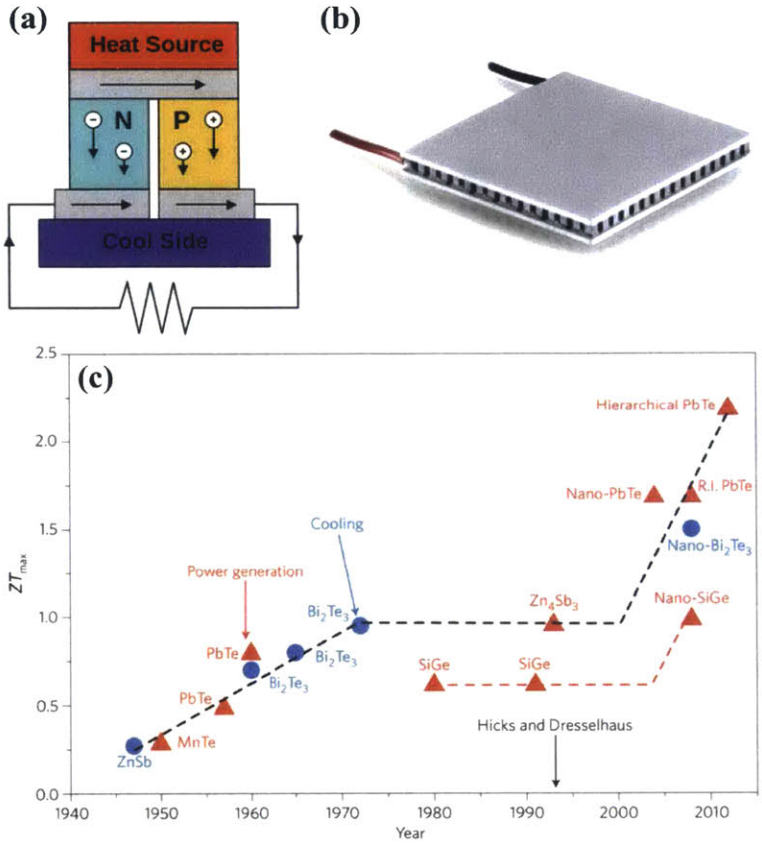

Figure 1-1 (a) Schematic of a typical configuration of a thermoelectric device, where two semiconductor materials (n-type and p-type) are connected thermally in parallel and electrically in series. (b) Photo showing a real thermoelectric module, where thermoelectric legs are sandwiched between two ceramic plates. Image from the website of FerroTec, Inc. (c) A zT roadmap showing the long-term increase of thermoelectric figure of merit zT over the past 60 years. There has been a boom in zT progress since 1990s, when nanotechnology was introduced into thermoelectrics. Figure adapted from Ref. 4.

The efficiency of a TE device is proportional to the nondimensional figure of merit $zT \equiv S^2\sigma T/\left(\kappa_e+\kappa_p\right)$, where S is the Seebeck coefficient defined as the ratio of the open circuit voltage to the applied temperature difference ($S\equiv-\Delta V/\Delta T$), σ is the electrical conductivity (the combination $S^2\sigma$ is usually called the power factor), T is the absolute temperature, and κ_e and κ_p are the electron and phonon contributions to the thermal conductivity, respectively. Figure 1-1 shows the typical configuration of a

thermoelectric device and the progress made in enhancing zT in the past decades. The low zT, and thus the low efficiency, stems from the fact that the relevant material properties are intertwined and usually show opposite trends in a single material. For example, the Seebeck coefficient measures the average entropy transported by charge carriers, and prefers nonsymmetric transport properties of charge carriers above and below the Fermi level (carriers above the Fermi level transport positive entropy, while carriers below the Fermi level transport negative entropy). For this reason the Seebeck coefficient S is usually high when the Fermi level is inside a band gap (nondegenerate semiconductors), degrades when the Fermi level moves into a band (degenerate semiconductors), and becomes negligibly small in a metal. On the other hand, the electrical conductivity σ is proportional to the carrier concentration and thus follows the opposite trend. This general correlation between the Seebeck coefficient and the electrical conductivity is commonly known as the Pisarenko relation[5], which implies that increasing the carrier mobility is crucial for boosting the power factor. Moreover, the electronic thermal conductivity usually grows with an increasing electrical conductivity, as indicated by the Wiedemann-Franz law ($\kappa_e = LT\sigma$, where L is a proportionality constant called the "Lorenz number"[6]), due to the fact that heat and electricity are transported by the same group of carriers in this case. Furthermore, although the phonon thermal conductivity does not directly connect to the electronic properties, the conventional methods of reducing the phonon thermal conductivity, such as by introducing defects and alloying, also increase the scattering of electrons, and deteriorate the electrical conductivity. From the above discussion, it is clear that an ideal TE material should possess a combination of properties of nondegenerate semiconductors (a high

Seebeck coefficient), metals (a high electrical conductivity), insulators (a low electronic thermal conductivity) and amorphous materials (a low phonon thermal conductivity).

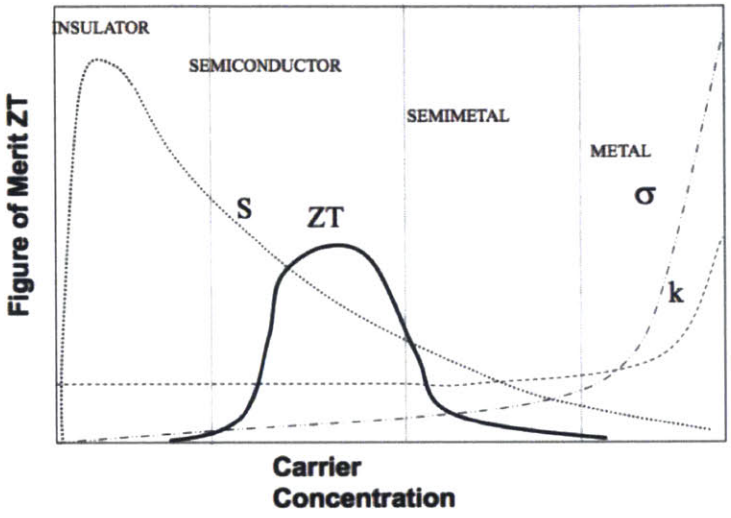

Figure 1-2 Schematic showing how the thermoelectric properties in simple model solids depends on the carrier concentration. The opposite trends of the Seebeck coefficient and the electrical conductivity poses a fundamental challenge to improving the thermoelectric performance.

These observations have placed fundamental difficulties in improving zT. As a more specific sample, Figure 1-2 displays the typical dependence of the thermoelectric properties on the carrier concentration. Since the control of the carrier concentration through doping is the most readily accessible knob that is used to tune the thermoelectric properties of a material, the opposite trends of the Seebeck coefficient and the electrical conductivity with increasing carrier concentration result in an optimum doping level, which seems to limit the best thermoelectric performance one can expect. One thing to note here, however, is that in realistic materials, the properties of the energy carriers are more complex than the simple model used in Fig. 1-2, and indeed a detailed understanding of the transport and interaction properties of energy carriers, combined with advanced nanotechnology and material synthesis capabilities[7], has led to a range of

successful strategies for better thermoelectric materials in the past decade[8]. In the next section, I summarize the existing successful strategies and the working principles behind them. As will be clear, the driving force for all these strategies has roots in the understanding of fundamental microscopic carrier transport and interactions, which is the motivation and focus of this thesis.

1.2 Strategies to Improve zT

From the definition of the figure of merit zT, it is clear that there are two main routes for improvement: by increasing the thermoelectric power factor ($S^2\sigma$), or by reducing the thermal conductivity κ. Both routes have led to successful examples, and there have been recent efforts of combining these two (by the so called "panoscopic" approach[9]). In this section I briefly review the existing strategies along both paths.

1.2.1 Improving Electronic Properties

The dilemma presented in Fig. 1-2 stems from the assumptions of simple electronic structures and transport characteristics, for example, a parabolic band and a constant electron relaxation time[10]. In reality, special electronic structures and/or electron scattering profiles, either natural or by design, often lead to exceptional thermoelectric performance much beyond what simple models predict. One seminal example was proposed by Hicks and Dresselhaus[11,12] in the early 1990s, when they discovered that low-dimensional materials, such as thin films, nanowires and quantum dots, can lead to better thermoelectric performance than their 3-dimensional counterparts. In those structures with certain lengths smaller than the electron coherence length, electrons are confined to a physical space with smaller size, and the resulting density of states exhibits

sharper transitions with respect to energy and is desirable for increasing Seebeck coefficient. This effect can be explained using the Mott formula for the Seebeck coefficient[6]

$$S = \frac{\pi^2}{3}\frac{k_B}{q}k_B T\left[\frac{1}{D}\frac{dD(E)}{dE} + \frac{1}{v^2\tau}\frac{d(v^2\tau)(E)}{dE}\right]_{E=E_F}, \qquad (1.1)$$

where k_B is the Boltzmann constant, q is the electronic charge, D is the electronic density of states, E is the electron energy, E_F is the Fermi energy, v is group velocity and τ is the electronic relaxation time (or reciprocal of the scattering rate). From the Mott formula, it is seen that the Seebeck coefficient is enhanced if there are sharp changes of either the density of states or the relaxation time around the Fermi level. This observation is consistent with the "asymmetric transport" picture described in the previous section. This idea is further quantified and mathematically formulated by Mahan and Sofo[13], where they showed via a variational calculation that the best electronic structure for a thermoelectric material is a δ -function-shaped density of states, and low-dimensionality provides a natural way to introduce sharp features in the density of states through the "**quantum confinement effect**". Although this quantum confinement effect was later observed in various low-dimensional systems, such as quantum dots[14], quantum wells[15], superlattices[16,17], nanowires[18] and a 2-dimensional electron gas confined in a single-layer oxide[19] , these structures are not easily scalable and hence not suitable for practical applications requiring larger-scale operation.

In addition to the size and dimensionality modification, the quantum confinement effect has also been applied to adjusting the relative positions of the electronic bands for better thermoelectric performance, first proposed in a GaAs/AlAs superlattice structure[20].

Since the Seebeck coefficient benefits from sharp changes of the density of states with respect to the carrier energy near the Fermi level, aligning the edges of multiple bands can lead to a largely enhanced density of states and an enhanced Seebeck coefficient without sacrificing the carrier mobility. This "**band convergence**" idea has later been generalized and realized experimentally by the rational alloying of bulk materials with different band gaps[21–26], as shown in Fig. 1-3. The concept of band convergence has also been recently identified to be the reason behind some of the presently known good conventional thermoelectric materials, such as the skutterudites[27].

Another way to introduce sharp features in the density of states is by doping. It is found that certain dopants when added to a specific matrix material can form impurity states that are resonant with the band continuum and can lead to a locally enhanced density of states[28]. Prominent examples include thallium-doped PbTe[29] and indium-doped SnTe[30], as shown in Fig. 1-4. A typical signature of the formation of resonant levels is the deviation of the Seebeck coefficient versus carrier concentration from the conventional Pisarenko plot: instead of a monotonically decreasing trend, in certain doping range the Seebeck coefficient is anomalously enhanced, as demonstrated for indium-doped SnTe as shown in Fig. 1-4(c).

As is clear from the previous discussion of the Mott formula, another way to improve Seebeck coefficient is to introduce sharp features in the electronic relaxation time. Beyond atomic defects, nanoscale domains (or nanoparticles, nanoprecipitates etc.) provide more degrees of freedom into control through scattering engineering, such as the particle size, shape, composition and spatial distribution. Unlike normal non-resonant atomic defects, whose characteristic size is much smaller than the electron wavelength

and thus invoke Rayleigh-type scattering with a monotonic dependence of the scattering strength on the electron energy[31], nanoscale domains have comparable sizes to the electron wavelength. Their scattering characteristics are thus analogous to Mie scattering of electromagnetic waves[32], where the interference effect is important and results in much richer features in the scattering strength. In this regime, the partial wave method[33] can be used for exact calculations of the scattering cross section of single nanodomains with regular shapes, and this approach has been applied to designing nanoparticles with desired scattering features[34–36], including electron filtering[37], where a cutoff energy is established below which carriers are much more strongly scattered[38–40] than those above.

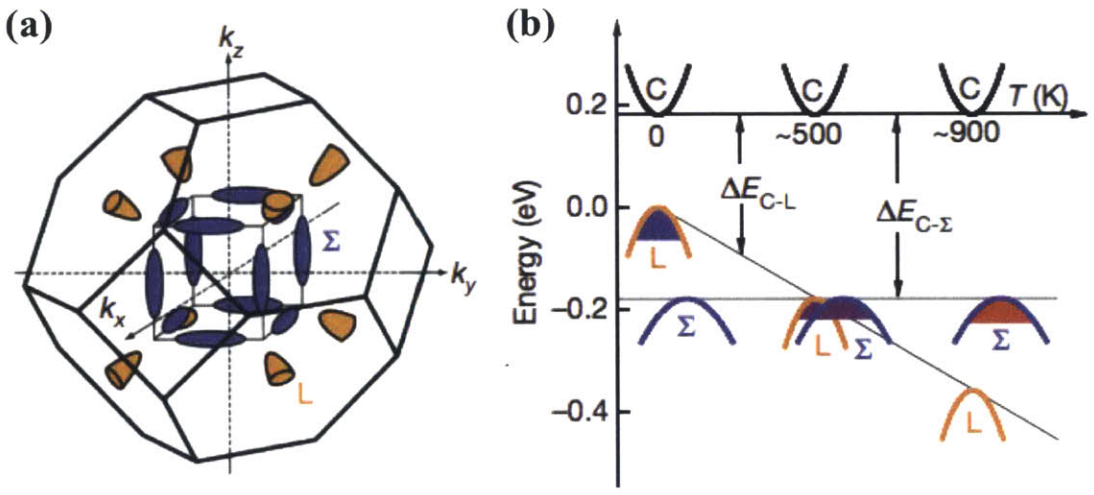

Figure 1-3 Schematic showing the concept of band convergence in a PbTe/PbSe alloy. (a) the position of hole pockets at the *L* (orange) and Σ (blue) points in the Brillouin zone of PbTe; (b) the change of energies of the *L* and Σ bands of PbTe with temperature. At a certain temperature (~500K), the two bands converge and give rise to an enhanced power factor. Alloying with PbSe can raise the band convergence temperature and leads to higher zT at higher temperatures. Adapted from Ref. 21.

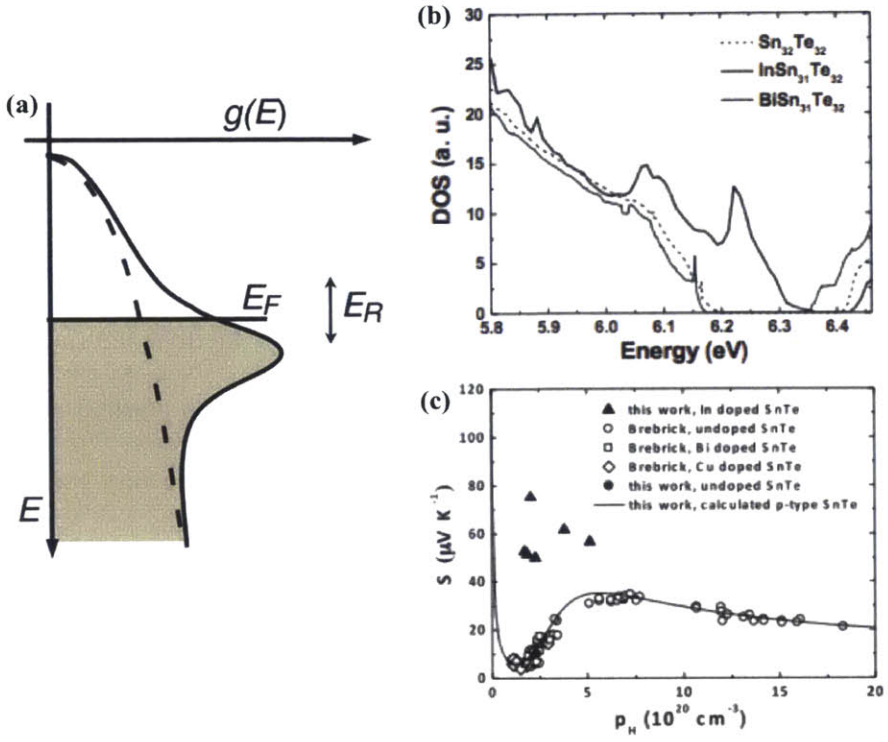

Figure 1-4 (a) Schematic showing how the resonant impurity level distorts the density of states and creates a local maximum. Adapted from Ref. 29. (b) Calculated density of states of indium-doped SnTe compared with bare SnTe and bismuth-doped SnTe from first-principles. A peak near the valence band edge is clearly seen in the case of indium-doped SnTe. (c) The Pisarenko plot of indium-doped SnTe, compared with other dopants and a two-band model. In indium-doped SnTe, the Seebeck coefficient is anomalously enhanced above the normal Pisarenko relation. (b) and (c) are adapted from Ref. 30.

In addition to the abovementioned strategies for enhancing the Seebeck coefficient, there are alternative approaches to boosting the thermoelectric power factor by increasing the carrier mobility, such as the modulation doping[41,42] and invisible doping[43,44], to which I contributed in my Master of Science thesis prior to starting my PhD program.

1.2.2 Reducing Thermal Conductivity by Nanostructures

One of the most successful strategies for improving the thermoelectric performance is by reducing the thermal conductivity with nanostrucutures, such as nanograin boundaries, nanoscale precipitates and particles. Nanoscale interfaces impose strong boundary scatterings on phonons and suppress the thermal conductivity (the classical size effect, or the "Casimir effect"). Reducing the phonon thermal conductivity of thermoelectrics by engineering phonon scattering dates back to the very early stages of thermoelectrics, when researchers used alloying to interrupt the observed phonon propagation effects. The prominent example is the Si/Ge alloy, the best thermoelectric material for high-temperature (> 900 K) applications for a long time, deployed by NASA for radioisotope thermoelectric generators for space missions in the 1970s[45]. A related concept is to introduce "filler" impurity atoms into complex compounds with cage-like structures, such as skutterudites[46–50], where the filler atoms "rattle" inside the cage structure and disrupt the phonon propagation due to the mismatch of natural frequencies. Both alloying and "filler-rattler" approaches introduce atomic scale disorders that are effective in scattering shorter-wavelength phonons, but less effective in scattering phonons with longer wavelengths that are the major heat carriers in most thermoelectric materials. Starting from the 1990s, the ultralow thermal conductivity in semiconductor superlattices (lower than corresponding bulk alloys) with nanoscale periods was observed experimentally[51–54]. It was later recognized[55,56] that the non-Fourier behavior in superlattices is largely due to the ballistic phonon transport in each layer and phonon scatterings at the interfaces, recently quantified by first-principles simulations[57]. This insight led to the later development of bulk nanocomposites[58] consisting of compact

nanograins with a high density of grain boundaries acting as effective filters for phonons with long wavelengths and mean free paths. The manufacturing process usually includes ball milling and hot pressing (or spark plasma sintering, SPS), and is cost-effective. This strategy has been successfully applied to reduce the thermal conductivity of a wide range of thermoelectric materials.

To understand the effectiveness of nanostructures in scattering phonons, first-principles techniques based on density functional theory (DFT) and density functional perturbation theory (DFPT) have been developed in recent years to study phonon dispersion and phonon-phonon anharmonic scatterings in detail[59,60]. These simulations reveal that phonons in real materials have mean free paths that span a range of length scales[61], as shown in Fig. 1-5, and thus hierarchical structures of different length scales are needed to maximally block the phonon flow[62].

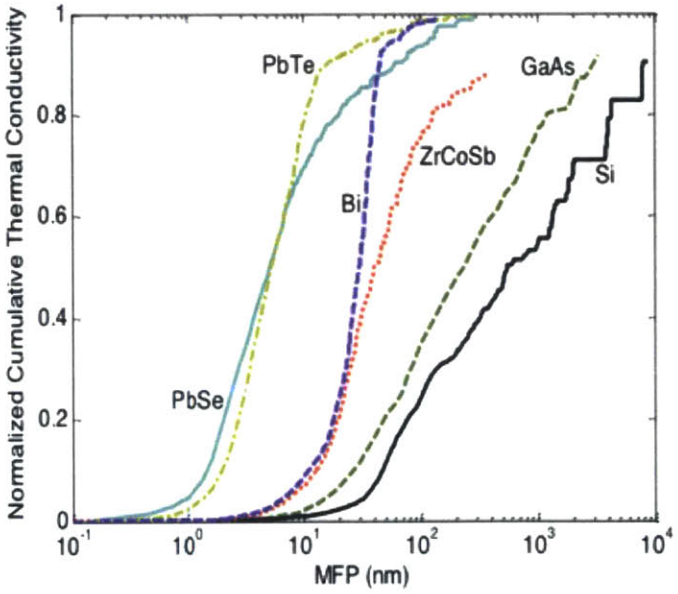

Figure 1-5 Calculated phonon mean free path distribution and the corresponding contribution to the total thermal conductivity, from first-principles techniques. Adapted from Ref. 61.

To verify the calculated phonon mean free path distribution, ultrafast optical spectroscopic techniques were developed to probe the length-scale-dependence of quasiballistic phonon transport[63–65]. When the length scale of the heat source (laser beam size[63] or the period of a thermal grating[64]) becomes comparable to the phonon mean free path, the phonon heat transport become partially ballistic and the measured effective thermal conductivity becomes lower than the bulk value. The combination of simulation and experimental tools has led to mode-by-mode understanding of phonon transport in real materials, and has directly contributed to the success of nanostructured thermoelectrics.

In comparison, the understanding of electron transport has largely lagged behind. On the simulation side, the ability to calculate intrinsic electrical transport properties limited by electron-phonon interaction has just been developed recently[66], and has not been utilized to study a wide range of materials and transport problems. On the experimental side, there have not been tools that can directly probe electron-phonon interaction at the single-mode level. These are the issues that this thesis aims to address, and the end goal of the investigations along this line is to eventually guide material search and design based on the understandings gained from fundamental research.

1.3 Spin Caloritronics

Spin caloritronics[67,68] is a nascent field of study that looks into the interaction between heat and spin. In addition to providing ways of thermally manipulating magnetization and magnetic domain walls[69–71] as supplements to conventional spintronics, it also holds promise of novel energy harvesting and cooling applications owing to the recent discovery of the spin Seebeck effect (SSE)[72–76] and its reciprocal spin

Peltier effect (SPE)[77,78]. Despite existing debates on details, it has been widely recognized that the aforementioned spin caloritronic effects are consequences of the interactions between phonons, electrons and spins[79–82]. From this perspective, spin caloritronics is a natural extension of both thermoelectrics and spintronics. Phonons are responsible for heat conduction in most solids; in metallic and semiconducting materials, electrons are carriers of charge, heat and spin; in magnetic materials, magnons[83] – the collective excitations of spins – also participate in transporting spin[84] and heat[85]. In the spin Seebeck effect, a thermal gradient drives a net spin flow across the boundary between a magnetic material and a metal with strong spin-orbit interaction, such as platinum, where the pure spin current is converted to an electrical voltage through the inverse spin Hall effect, as illustrated in Fig. 1-6.

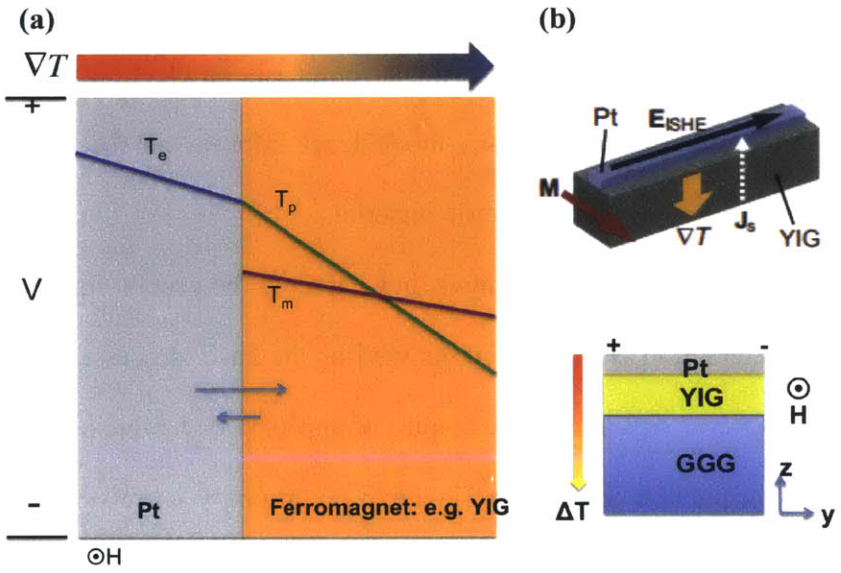

Figure 1-6 (a) Schematic showing the mechanism of spin Seebeck effect. Here T_e, T_p and T_m are the temperature distributions of electrons, phonons and magnons, respectively. (b) A real device configuration of longitudinal spin Seebeck effect. Adapted from Ref. 86.

Despite existing controversy on the nature of the effect, it has been proposed that the spin Seebeck effect can be a candidate for efficient thermal energy harvesting due to the decoupled electrical and thermal transport. In addition to participating in the spin Seebeck effect, magnons can also transport heat[87,88], just as phonons and electrons. As an exploratory part of this thesis, I study how phonon-magnon coupling can lead to a novel magnetic cooling effect. Now with more players on the field (electrons, phonons and magnons), the fundamental studies of spin caloritronics, especially the interplay among different carriers, can potentially benefit thermoelectric research.

1.4 Scope and Organization of Thesis

The focus of this thesis is to develop and apply first-principles simulation and experimental tools to study transport and interaction of electrons, phonons and magnons in real solid state materials, with a particular emphasis on electron-phonon interaction, which can hopefully lead to mode-by-mode level information that can benefit future design and engineering of thermoelectric materials.

The thesis is organized as follows. In Chapter 2, the general formulation of carrier transport and interaction is introduced, as well as the basic processes of first-principles simulation. Chapter 3 presents two examples of applying first-principles simulation tools to study phonon-phonon interaction (in $FeSb_2$, a strongly correlated low temperature thermoelectric material), and electron-phonon interaction (in phosphorene, a newly discovered two-dimensional material). Chapter 4 elaborates on a combined simulation/experimental effort to understand how electrons scatter phonons through electron-phonon interaction and reduce the lattice thermal conductivity in semiconductors, which has been largely ignored in previous studies. Chapter 5 covers an

exploratory project, where the Boltzmann transport equation is applied to coupled phonon-magnon diffusion and leads to the discovery of a novel magnon cooling effect. Chapter 6 summarizes the thesis and points to potential future directions.

Chapter 2

Carrier Transport and Interaction:

General Formulation

2.1 Elements of First-Principles Simulation

In this section we review the ingredients and basic process for first-principles simulations of electron and phonon transport properties. Ever since the foundations of the density functional theory (DFT) were established by Hohenberg, Kohn and Sham[89,90], this computational technique for materials' electronic structure and related equilibrium properties has evolved at a remarkable pace. DFT-based first-principles calculations of the electron and phonon band structures have now become routine even for materials

with complicated unit cells. To calculate thermoelectric properties, however, one has to go beyond the standard DFT band structure calculations, and take into account various scattering processes. There developments are highly nontrivial in terms of both programming complexity and computational cost. To make the calculations tractable, usually only the lowest order scattering process that is captured by the Fermi's golden rule, is calculated. When dealing with electron-phonon interactions in particular, a necessary simplification, namely the Born-Oppenheimer approximation, is used to decouple the electronic and ionic coordinates. Combining the information from band structure calculations with the scattering information, the Boltzmann transport equation can be solved at various levels for the thermoelectric transport properties. In principle this whole process is parameter free, and the only input is the crystal structure and atomic composition of the material. The complete process is illustrated in Fig. 2-1.

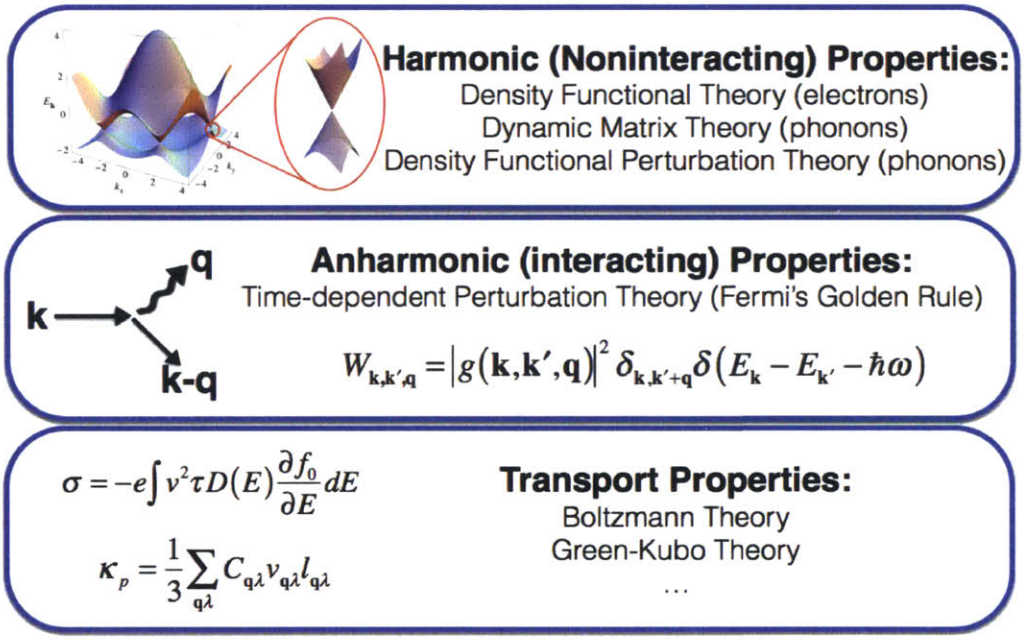

Figure 2-1 Flow chart illustrating the basic process of DFT-based first-principles simulations of thermoelectric transport properties.

2.1.1 Boltzmann Transport Theory

We start with the transport theory as a roadmap of ingredients that are needed from first-principles simulations. There are mainly two categories of transport theories. The first one adopts more of a wave-like point of view, starts directly from the governing dynamic equations of carriers (Schrödinger equation for electrons, and lattice dynamical equations for phonons), and the time evolution of the carriers' states, usually in the form of wavefunctions, is then investigated using Green's-functions-based techniques[91,92]. Because the exact time evolution of wavefunctions is solved, this method has the ability to capture interference effect of wavefunctions, or in other words, the effect of coherence. On the other hand, the interactions among carriers are added to the calculation usually as perturbations. This method has been applied to study quantum transport of electrons in nanoscale conductors[93], phonon transport across interfaces[94] and coherent phonon transport in superlattices[95,96]. In realistic thermoelectric materials, however, interactions of carriers among themselves and with impurities are often strong and the coherence effect is suppressed. In this case, it is more convenient to start from the fully incoherent limit, namely the particle picture, where energy carriers are treated as quasiparticles and their wave nature is only invoked in particular situations, such as the reflection and transmission at an interface. This perspective of transport is conveniently formulated in the framework of the Boltzmann transport equation

$$\frac{\partial f(\mathbf{r},\mathbf{p},t)}{\partial t}+\mathbf{v}\cdot\frac{\partial f(\mathbf{r},\mathbf{p},t)}{\partial \mathbf{r}}+\mathbf{F}\cdot\frac{\partial f(\mathbf{r},\mathbf{p},t)}{\partial \mathbf{p}}=\left(\frac{\partial f}{\partial t}\right)\Bigg|_{col}, \tag{2.1}$$

where $f(\mathbf{r},\mathbf{p},t)$ is the distribution function in phase space that represents the number (or the probability, depending on normalization) of particles occupying a certain state with

real-space position **r** and momentum **p** at time t, while **v** is the group velocity of the carrier and **F** is the external force exerted on the particle. The left hand side of Eq. (2.1) depicts the motion of carriers in phase space under the influence of an external force field, while the right hand side, the so-called "collision term", deals with the change of the distribution function due to scattering processes, either among carriers or with impurities. The Boltzmann transport equation is a reduced form of the Liouville equation that is commonly studied in many-particle statistical physics, where the unknown is a many-particle distribution function $f(r_1, p_1, r_2, p_2 ...)$. In the weak interaction regime, meaning the scattering length (square root of the scattering cross section) of the carrier interactions is much smaller than the average spacing between the carriers, the Liouville equation can be reduced through a formal procedure named Bogoliubov-Born-Green-Kirkwood-Yvon (BBGKY) hierarchy[97] to an equation of single-particle distribution function and a collision term involving a two-particle distribution function. Further invoking the so-called "molecular chaos approximation", which breaks down the two-particle distribution function into a product of two single-particle distribution functions, the Boltzmann equation can be derived[98]. With the molecular chaos approximation, the coherence between particles is abandoned and this approximation directly leads to entropy generation and the Boltzmann's H-theorem[97]. In other words, the collision term on the right hand side of the Boltzmann equation includes all information about the carrier interaction, whose exact form is unknown in most practical situations. Different levels of approximations are developed to devise a physically reasonable form of the collision term.

The simplest approximation of the collision term is the relaxation time approximation (RTA)

$$\left(\frac{\partial f}{\partial t}\right)\Big|_{col} = -\frac{f - f_0}{\tau}, \tag{2.2}$$

where $f_0(\mathbf{r},\mathbf{p})$ is the equilibrium distribution function (namely the Fermi-Dirac distribution for fermions, the Bose-Einstein distribution for bosons and the Boltzmann distribution for classical particles) and τ is the relaxation time of a specific state due to scattering processes. The physical meaning of this form of the collision term is clear: the scattering processes tend to bring the system back to equilibrium, with a time scale set by the relaxation time. In certain scenarios this physical picture is not accurate, for example the phonon normal scattering processes conserve phonon momentum and cannot damp the system towards equilibrium[6]. Nevertheless, RTA often leads to reasonably accurate quantitative predictions for engineering applications, and more importantly, RTA gives an intuitive physical picture of transport that can guide material analysis and design. In some special cases where the phonon normal scattering processes actually dominate the Umklapp scattering processes, such as in certain two-dimensional materials[99], an iterative self-consistent solution of the Boltzmann equation is needed.

With RTA, the Boltzmann transport equation can be readily solved[10], and the particle number and energy flux can be calculated with the solved distribution function. In the case of electrons, the two fluxes depend linearly on both the applied electric field and temperature gradient when the applied field and temperature gradient are weak, and the linear coefficients are directly related to the thermoelectric transport properties. A detailed discussion of the formulation of coupled-transport is postponed till Chapter 5 on

the coupled diffusion of phonons and magnons, which is fully analogous to the coupled electron transport.

The thermoelectric transport properties have the following forms from the Boltzmann transport equation with the RTA:

$$\sigma = -e\int v_e^{\,2}\tau_e D_e(E)\frac{\partial f_0}{\partial E}dE, \tag{2.3}$$

$$S = \frac{1}{\sigma T}\int \left(E - E_f\right) v_e^{\,2}\tau_e D_e(E)\frac{\partial f_0}{\partial E}dE, \tag{2.4}$$

$$\kappa_e = -\frac{1}{T}\int \left(E - E_f\right)^2 v_e^{\,2}\tau_e \frac{\partial f_0}{\partial E}dE - TS^2\sigma, \tag{2.5}$$

$$\kappa_p = \frac{1}{3}\int v_p^2\tau_p \hbar\omega D_p(\omega)\frac{\partial n_0}{\partial T}d\omega, \tag{2.6}$$

where subscripts e and p refer to electron and phonon properties, respectively, and f_0 and n_0 represent the Fermi-Dirac and the Bose-Einstein distributions. It is noted here that the use of the density of states in the above equations is not necessary for first-principles calculations, where the integration with respect to electron energy or phonon frequency is replaced by a summation over all electron and phonon states. Nevertheless we keep the equations written in terms of the density of states here, because it is one of the most important material properties when thermoelectric materials are analyzed.

Now it is clear from Eqs. (2.3) to (2.6) that the information needed from first-principles calculations includes: the energy (frequency), group velocities and the relaxation times of electrons and phonons. The first two properties can be readily calculated with standard DFT, and the real challenge here is to accurately and efficiently

calculate the relaxation times of electrons and phonons from first-principles. In section 2.1.2, we will briefly introduce DFT and the band structure calculations, and we dedicate section 2.2 to introducing the formalism of relaxation time calculations.

2.1.2Electron and Phonon Band Structures and Density Functional Theory

The first step in studying carrier transport is to look for the carrier states that exist in a given material. In the case of electrons, a Schrödinger equation with a periodic ionic potential needs to be solved[6]. Due to the periodicity of a crystal lattice (or discrete translational symmetry), this Schrödinger equation can be projected into different crystal momenta **k** in the reciprocal space, and at each **k** point a smaller scale equation needs to be solved. While this calculation at the single-electron level is trivial, it is important to properly include electron-electron interactions to accurately model real materials. Different levels of approximations of electron-electron interactions were developed for realistic calculations[100,101]. The first level is the Hartree method, where for a given electron, the effect of all other electrons is smeared out as a Coulomb interaction with a continuous charge distribution. There are two major effects missing from this calculation: electron exchange and correlation. The exchange interaction stems from the Pauli exclusion principle, which determines that electrons with the same spin tend to expel each other in real space and the Coulomb energy between them is lowered by this expulsion. The correlation effect refers to the error introduced when smearing out discrete and moving electrons into a static continuous charge distribution, and in practice just includes all other deviations from single-electron results aside from the exchange interaction. The second-level of approximation is the Hartree-Fock method, where the

exchange interaction is treated exactly by using an antisymmetrized Slater determinant as the trial function in a variational solution of the many-particle Schrödinger equation. In 1964, Hohenberg and Kohn proved in their seminal paper[89] that all ground-state properties of a many-electron systems are solely determined by the ground-state charge density distribution. In other words, it is sufficient to solve for the ground-state charge density distribution, which is a single scalar in space, instead of the full wavefunction with the coordinates of every electron. Based on this observation, Kohn and Sham[90] derived a group of single-particle equations that can be solved in an iterative self-consistent way. This group of equations was later named "density functional theory" (DFT), and the key component of DFT is the introduction of an exchange-correlation functional $E_{xc}[\rho]$ of the charge density distribution ρ. Although the exact form of this exchange-correlation functional is unknown, many effective approximations have been devised, among which the most widely used is the local density approximation (LDA):

$$E_{xc}[\rho] = \int \rho(\mathbf{r}) \varepsilon_{xc}(\rho) d\mathbf{r}, \tag{2.7}$$

where $\varepsilon_{xc}(\rho)$ is the exchange-correlation energy of a uniform interacting electron gas that can be numerically calculated to a high precision. And thus, LDA consists of the physical approximation of dividing an arbitrary charge density distribution into a combination of uniform electron gases within small volumes. A systematic extension of LDA is the generalized gradient approximation (GGA), where the exchange-correlation energy also depends on the spatial gradient of the charge density distribution.

Another crucial piece of practical DFT simulation is the use of pseudopotentials. Pseudopotentials are artificially designed ionic potentials of the valence electrons that

include the effects of both the atomic nuclei and the inner-shell core electrons. With pseudopotentials, the number of electrons one needs to simulate in a real material is largely reduced, and thus so is the computational cost also reduced. To generate a pseudopotential, typically a full DFT simulation of a single atom is first carried out, and the wavefunctions of the inner-shell electrons are processed to generate an effective potential that keeps the scattering cross section of the valence electrons unchanged[102]. This is usually done by calculating the logarithmic derivative of the wavefunctions of the valence electrons at a certain cut-off radius to ensure that the logarithmic derivatives are the same when the real core electrons are included or when the effective potential is used instead. This type of pseudopotential is called "norm-conserving" pseudopotentials, and is the main type used in this thesis.

DFT has become a standard technique in chemistry and material science nowadays, and there are commercial as well as open-source computer programs available for electron and phonon band structure calculations. The DFT engine used in this thesis is Quantum Espresso[103], an open-source package written in Fortran; and post-processing of the DFT data was mostly carried out by home-made computer codes, except for the Wannier interpolation program EPW[104] that will be introduced later.

As examples, Figure 2-2 displays the electronic band structures of phosphorene and $FeSb_2$, the two materials studied in detail in later chapters. The electronic band structures provide several crucial parameters that determine the electron transport: the energy band gap, the effective masses and the group velocities. It is well known that DFT calculation underestimates the band gaps, and in practice the bands are often rigidly shifted to match the experimental band gap. The effective masses are defined through the

second derivative of the energy dispersion relation $m^* = \hbar^2 \left(\frac{\partial^2 E}{\partial k^2} \right)^{-1}$, which is an important parameter in evaluating the thermoelectric performance: a large effective mass leads to large density of states, and often benefits the Seebeck coefficient, while a smaller effective mass is good for a high mobility and thus benefits the electrical conductivity. The group velocities are defined as the derivative of the energy dispersion relation $\mathbf{v} = \frac{1}{\hbar} \nabla_{\mathbf{k}} E$ and directly enters Eqs. (2.3) to (2.6) for calculating transport properties.

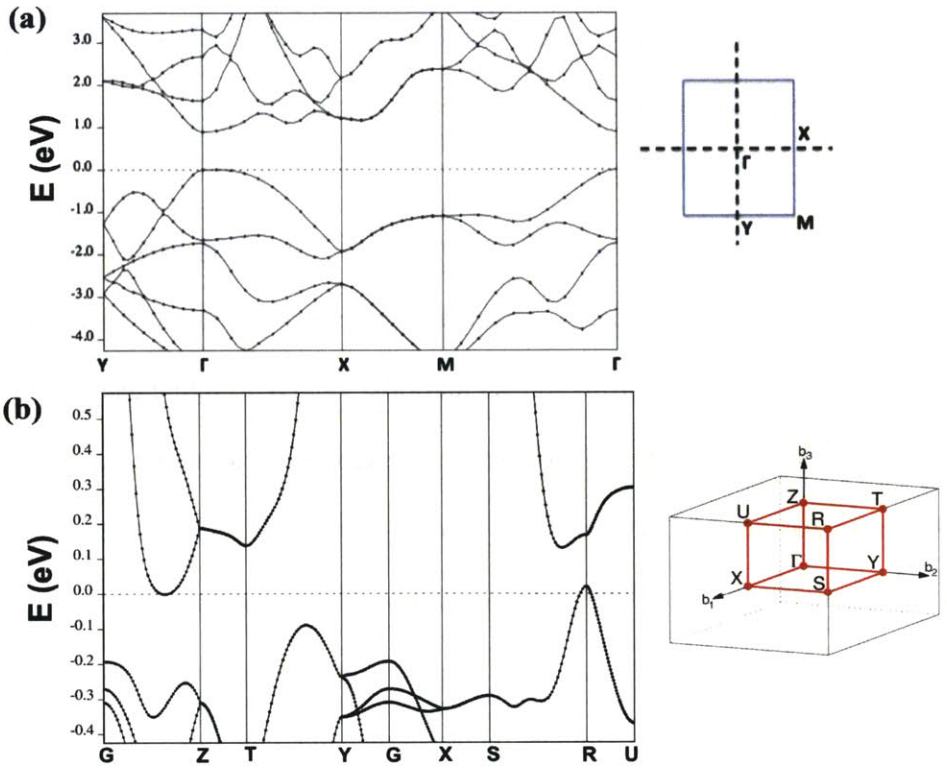

Figure 2-2 Examples of DFT calculation of electronic band structures. (a) The electronic band structure of phosphorene, a two-dimensional semiconductor. Large anisotropies of both the conduction and valence bands are observed near the band edges at the Γ point. (b) The electronic band structure of $FeSb_2$. Experimentally a semiconductor, $FeSb_2$ is found to be a metal from DFT calculation, a well-known problem of DFT for underestimating the bandgaps.

To calculate the band dispersion of phonons, the interatomic forces need to be calculated. Since the atoms in a solid are "glued" together by the electron cloud, the interactomic forces are the cost of the total electron energy with respect to displacements of atoms. In general, these forces can be calculated by two means: by manually displacing atoms from their equilibrium positions and using DFT to calculate the forces exerted on all the atoms, the so-called "frozen-phonon" approach[105]; or by solving the linear response of the charge density with respect to atomic positions $\frac{\partial \rho}{\partial \mathbf{R}}$ directly in an extended DFT framework, the so-called "density functional perturbation theory" (DFPT)[106]. The two approaches are mathematically equivalent, and the only difference is that one works in real space, while the other works in the reciprocal space. With the interatomic forces calculated through either of the two methods, the lattice dynamical equations of the atoms can be solved for the phonon dispersion relations[107]. Figure 2-3 shows the phonon dispersion relation of $FeSb_2$ calculated using DFT and the "frozen phonon" approach.

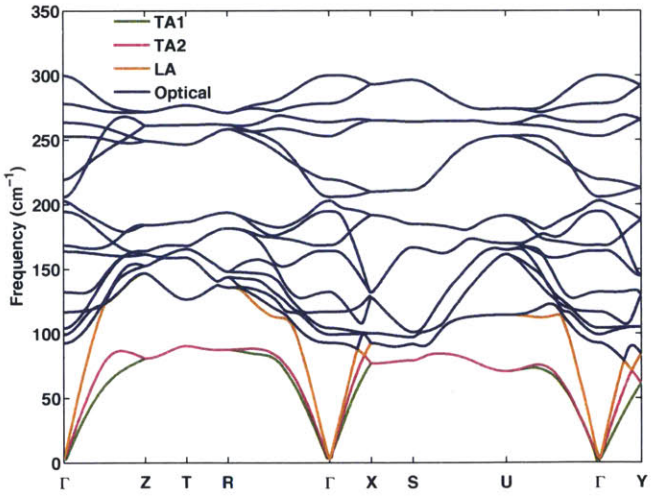

Figure 2-3 Calculated phonon dispersion relation of $FeSb_2$ using DFT and the frozen phonon approach.

2.2 Scattering and Fermi's Golden Rule

It is clear from discussions in the previous sections that the real challenge of calculating the electron and phonon transport properties from first-principles is to deal with the scattering processes, or in other words, to calculate the relaxation time τ accurately in a computationally tractable way. In this section we describe the general formalism of calculating scattering rates of various processes and the strategies to reduce the computational cost in practice. A more comprehensive introduction is given in a review article[108] coauthored by the author of this thesis.

In the transport regime that we are usually concerned with, the carrier interaction (scattering) can be safely treated using perturbation theories. Starting with the electron and phonon band structures as the unperturbed states, the interaction among the carriers or between carriers and impurities are introduced as a perturbation Hamiltonian ΔH. Depending on the nature of the interactions, ΔH can be either time-independent (the impurity scattering) or time-dependent (electron-phonon, and phonon-phonon interactions). In the framework of time-dependent perturbation theory[109], the eigenstates of the unperturbed system will not evolve independently any more, and instead transitions happen among the eigenstates. The rate of the transtions from the initial state $|i\rangle$ to the final state $|f\rangle$, in the lowest perturbation order, is give by the Fermi's golden rule:

$$W = \frac{2\pi}{\hbar}\left|\langle i|\Delta H|f\rangle\right|^2 \delta\left(E_i - E_f\right), \tag{2.8}$$

where W is the transition rate, E_i and E_f are the energies of the initial and final states. The δ function imposes the energy conservation in the case of a time-independent perturbation. If the perturbation has a time-harmonic form instead, the energy of the final states no longer has to be the same as the initial state, and instead $\delta(E_f - E_i - \hbar\omega)$ should be used in Eq. (2.8). In the following subsections, we introduce the forms of ΔH in cases of the different scattering processes studied in this thesis.

2.2.1 Phonon-Phonon Anharmonic Scattering

If the interatomic potential U in a real solid is expanded in a Taylor series of the atomic displacements from the equilibrium positions $\{u_i\}$

$$U = \frac{1}{2}\sum_{ij}\phi_{ij}u_i u_j + \frac{1}{3!}\sum_{ijk}\psi_{ijk}u_i u_j u_k + \ldots, \tag{2.9}$$

the first order terms vanish because the displacements are measured from the equilibrium position, the second order (harmonic) force constants $\phi_{ij} = \frac{\partial^2 U}{\partial u_i \partial u_j}$ defines the phonon dispersion, and the higher order (anharmonic) force constants, most importantly the third order force constants $\psi_{ijk} = \frac{\partial^3 U}{\partial u_i \partial u_j \partial u_k}$ cause phonons to scatter among themselves and thus create the thermal resistance in a real solid. Both harmonic and anharmonic force constants can be calculated by the "frozen phonon" method and DFPT. With the third order force constants being the perturbation, the Fermi's golden rule for phonon-phonon anharmonic processes is given as[110]

$$\frac{1}{\tau_{\mathbf{q}\lambda}^{ph-ph}}=\frac{\pi}{\hbar^2}\sum_{\mathbf{q}_1\lambda_1,\mathbf{q}_2\lambda_2}\left|V_{\mathbf{q}\lambda,\mathbf{q}_1\lambda_1,\mathbf{q}_2\lambda_2}\right|^2\begin{Bmatrix}\left(1+n^0_{\mathbf{q}_1\lambda_1}+n^0_{\mathbf{q}_2\lambda_2}\right)\delta\left(\omega_{\mathbf{q}\lambda}-\omega_{\mathbf{q}_1\lambda_1}-\omega_{\mathbf{q}_2\lambda_2}\right)\delta_{\mathbf{q}-\mathbf{q}_1-\mathbf{q}_2-\mathbf{G}}\\+\left(n^0_{\mathbf{q}_2\lambda_2}-n^0_{\mathbf{q}_1\lambda_1}\right)\begin{bmatrix}\delta\left(\omega_{\mathbf{q}\lambda}+\omega_{\mathbf{q}_2\lambda_2}-\omega_{\mathbf{q}_1\lambda_1}\right)\delta_{\mathbf{q}-\mathbf{q}_1+\mathbf{q}_2-\mathbf{G}}\\-\delta\left(\omega_{\mathbf{q}\lambda}+\omega_{\mathbf{q}_1\lambda_1}-\omega_{\mathbf{q}_2\lambda_2}\right)\delta_{\mathbf{q}+\mathbf{q}_1-\mathbf{q}_2-\mathbf{G}}\end{bmatrix}\end{Bmatrix}, \quad (2.10)$$

where $\tau_{\mathbf{q}\lambda}^{ph-ph}$ is the relaxation time of a phonon mode with wave vector $\mathbf{q}$ and branch index λ, $n^0_{\mathbf{q}\lambda}$ is Bose-Einstein distribution, $\omega_{\mathbf{q}\lambda}$ is the phonon frequency, $\mathbf{G}$ is a reciprocal lattice vector and $V_{\mathbf{q}\lambda,\mathbf{q}_1\lambda_1,\mathbf{q}_2\lambda_2}$ is the three-phonon interaction matrix elements given by

$$V_{\mathbf{q}\lambda,\mathbf{q}_1\lambda_1,\mathbf{q}_2\lambda_2}=\left(\frac{\hbar}{2}\right)^{3/2}\sum_{\mathbf{R}_i\tau_i\alpha_i}\psi^{\alpha\beta\gamma}_{0\tau,\mathbf{R}_1\tau_1,\mathbf{R}_2\tau_2}\frac{e^{i(\mathbf{q}_1\cdot\mathbf{R}_1+\mathbf{q}_2\cdot\mathbf{R}_2)}e^{\tau\alpha}_{\mathbf{q}\lambda}e^{\tau_1\beta}_{\mathbf{q}_1\lambda_1}e^{\tau_2\gamma}_{\mathbf{q}_2\lambda_2}}{\left[M_\tau M_{\tau_1}M_{\tau_2}\omega_{\mathbf{q}\lambda}\omega_{\mathbf{q}_1\lambda_1}\omega_{\mathbf{q}_2\lambda_2}\right]^{1/2}}, \quad (2.11)$$

where $\mathbf{R}$ denotes the coordinate of a unit cell and τ is the coordinate of an atom inside the unit cell, $\{\alpha,\beta,\gamma\}$ labels the coordinate directions, M_τ is atomic mass and $e^{\tau\alpha}_{\mathbf{q}\lambda}$ is one component of the porization vector of the phonon mode $\{\mathbf{q},\lambda\}$. The two δ-functions in Eq. (2.10) impose the energy conservation as well as the crystal momentum conservation due to the crystal periodicity. With Eqs. (2.10) and (2.11), the phonon relaxation time due to phonon-phonon anharmonic interaction can be calculated, and together with Eq. (2.6), the lattice thermal conductivity can be calculated.

2.2.2 Electron-Phonon Interaction

Electron-phonon interaction has been well known to create major resistance to electron transport in metals and semiconductors. The coordinates of electrons and atomic nuclei represent the most common degrees of freedom in a solid. The full quantum mechanical treatment of the excitations in a solid thus require the solution of the

Schrödinger equation involving the coordinates of all electrons and atomic nuclei, which appears intractable in most cases. A widely applied simplification, the Born-Oppenheimer approximation[111], makes use of the fact that the electrons' mass is much smaller than that of the nuclei, and the electrons respond to the motions of the nuclei so quickly that the nuclei can be treated as static at each instant. Under the Born-Oppenheimer approximation, the coordinates of the nuclei enter the electronic Schrödinger equation as external parameters, and in turn the electronic ground-state energy acts as part of the interaction energy between the nuclei given a specific configuration, with which the quantized excitations of the atomic nuclei, namely the phonons, can be investigated separately from the electrons[6]. It is important to note, however, that the Born-Oppenheimer approximation does not separate the electronic and atomic degrees of freedom completely, and a remaining coupling term can cause transitions between the eigenstates of the electron and phonon systems[110]. This electron-phonon interaction problem was first studied by Bloch[112], and later understood as the main source of resistance to electrical conduction in metals and semiconductors at higher temperatures[10,31,110], and played the key role in the microscopic theory of superconductivity[113].

In the case of electron-phonon interaction, the perturbation Hamiltonian is the change of the total electron energy with respect to atomic displacements, and the Fermi's golden rule can be derived accordingly as

$$\frac{1}{\tau_e^{ep}(\mathbf{k})}=\frac{2\pi}{\hbar}\sum_{\mathbf{k}',\lambda}\left|\langle\mathbf{k}'|\partial_{\mathbf{q}\lambda}V|\mathbf{k}\rangle\right|^2\begin{bmatrix}\left(f_{\mathbf{k}'}+n_{\mathbf{q}}\right)\delta\left(E_{\mathbf{k}}-E_{\mathbf{k}'}+\hbar\omega_{\mathbf{q}\lambda}\right)\delta_{\mathbf{k}+\mathbf{q},\mathbf{k}'+\mathbf{G}}\\+\left(1+n_{\mathbf{q}}-f_{\mathbf{k}'}\right)\delta\left(E_{\mathbf{k}}-E_{\mathbf{k}'}-\hbar\omega_{\mathbf{q}\lambda}\right)\delta_{\mathbf{k}-\mathbf{q},\mathbf{k}'+\mathbf{G}}\end{bmatrix}\left(1-\frac{\mathbf{v}_{\mathbf{k}'}\cdot\mathbf{v}_{\mathbf{k}}}{|\mathbf{v}_{\mathbf{k}'}||\mathbf{v}_{\mathbf{k}}|}\right),\quad(2.12)$$

where τ_e^{ep} is the relaxation time of electrons due to electron-phonon interaction, $\mathbf{k}$ and $\mathbf{k}'$ are the wave vectors of initial and final electron states, $\partial_{\mathbf{q}\lambda} V$ is the change of electron total energy with respect to a phonon perturbation with wave vector $\mathbf{q}$ and band index λ that can be obtained from DFPT calculations, and the term $\left(1-\frac{\mathbf{v}_{\mathbf{k}'}\cdot\mathbf{v}_{\mathbf{k}}}{|\mathbf{v}_{\mathbf{k}'}||\mathbf{v}_{\mathbf{k}}|}\right)$ considers the fact that large-angle scatterings are more effective in creating resistance to electron transport than small-angle scatterings. Thus the defined relaxation time is also called the "momentum relaxation time", in contrast to the "energy relaxation time" without the $\left(1-\frac{\mathbf{v}_{\mathbf{k}'}\cdot\mathbf{v}_{\mathbf{k}}}{|\mathbf{v}_{\mathbf{k}'}||\mathbf{v}_{\mathbf{k}}|}\right)$ factor[93]. Equation (2.12) implies that the strength of electron phonon scattering depends on: 1) the strength of the coupling, represented by the magnitude of the matrix elements; 2) the available phase space for the scattering events to happen, determined by the energy and momentum conservation requirements; 3) the available final electron states, since Eq. (2.12) sums over all possible final states. We will discuss the impact of the three factors on the electron-phonon scattering in phosphorene in detail in Chapter 3.

Electron-phonon interaction can affect phonon transport as well. We will discuss this effect in semiconductors in detail in Chapter 4, and here we only provide the Fermi's golden rule for the phonon relaxation time due to electron-phonon scattering[110]

$$\frac{1}{\tau_{\mathbf{q}\lambda}^{ep}}=-\frac{2\pi}{\hbar}\sum_{mn,\mathbf{k}}\left|g_{mn}^{\lambda}(\mathbf{k},\mathbf{q})\right|^2\left(f_{n\mathbf{k}}-f_{m,\mathbf{k}+\mathbf{q}}\right)\delta\left(E_{n\mathbf{k}}-E_{m,\mathbf{k}+\mathbf{q}}-\hbar\omega_{\mathbf{q}\lambda}\right), \tag{2.13}$$

where m and n are the indices of electron energy bands, $g_{mn}^{\lambda}(\mathbf{k},\mathbf{q})=\left(\hbar/2m_0\omega_{\mathbf{q}\lambda}\right)^{1/2}\langle m,\mathbf{k}+\mathbf{q}|\partial_{\mathbf{q}\lambda}V|n,\mathbf{k}\rangle$ is the electron-phonon coupling matrix

element (m_0 is a convenient reference mass in practical calculations, and real atomic masses are absorbed into the matrix elements).

2.2.3 Interpolation with Maximally Localized Wannier Functions

In the preceding subsections, we have presented the ingredients needed for calculating the relaxation times of electrons and phonons due to electron-phonon and phonon-phonon interactions. These ingredients can all be obtained from standard DFT and DFPT calculations. The calculations of phonon-phonon interactions can be readily carried out with these ingredients. For electron-phonon interactions, however, there is another technical obstacle: because the phonon energy scale (tens of meV) is much smaller than the electron energy scale (~eV), usually a very dense sampling mesh of the Brillouin zone is required for a converged calculation, which can be computationally costly. One way to get around this obstacle is to use interpolation: first carry out the calculations on a coarse mesh, and then interpolate to a sufficiently dense mesh required for convergence. Although the idea is straightforward, it is nontrivial to find an accurate and systematic interpolation method in this case. Intuitively, interpolation in the reciprocal space is equivalent to the extension of the distance of interaction in real space that is included in the calculation. In this vein, a clear path is that the calculations first on the coarse mesh should cover interactions in real space up to a cut-off distance, beyond which the interactions are weak and can be safely ignored. Then with the interaction matrix elements on a real space basis, interpolation to an arbitrarily dense mesh in the reciprocal mesh should be accurate because the artificially excluded long-range interactions are small. This method has actually been widely used in phonon-phonon scattering calculations already, where the real space interatomic force constants are

usually cut-off at a certain distance (or "neighbor shell"), beyond which the interatomic force constants are set to zero. In the case of electron-phonon interaction, however, this method is not as straightforward because there is no apparent real space basis to use to describe the interactions in real space.

In fact, there is a real space correspondence to the Bloch wavefunctions in reciprocal space, called the Wannier functions[6]. Wannier's observation was that the Bloch wavefunctions $\psi_{n\mathbf{k}}(\mathbf{r}) = u_{n\mathbf{k}}(\mathbf{r})e^{i\mathbf{k}\cdot\mathbf{r}}$, where $u_{n\mathbf{k}}(\mathbf{r})$ is a periodic function in $\mathbf{r}$, are also periodic in $\mathbf{k}$ with a period of $\frac{2\pi}{a}$ with a being the lattice constant, and thus a set of real space wavefunctions can be defined as a spatial Fourier transform of the Bloch wavefunctions with respect to $\mathbf{k}$

$$\varphi_{n\mathbf{R}}(\mathbf{r}) = \frac{V}{(2\pi)^3}\int_{BZ} d\mathbf{k} e^{-i\mathbf{k}\cdot\mathbf{R}} \sum_{m=1}^{J} U_{mn}^{(\mathbf{k})} \psi_{m\mathbf{k}}(\mathbf{r}), \tag{2.14}$$

where V is the unit cell volume, J is the number of electron bands, and $U_{mn}^{(\mathbf{k})}$ is an arbitrary unitary matrix. The Wannier functions $\varphi_{n\mathbf{R}}(\mathbf{r})$ are reminiscent of atomic orbitals, and indeed are the atomic orbitals in the simple case of a tight binding model[6]. In a real material, however, the Wannier functions $\varphi_{n\mathbf{R}}(\mathbf{r})$ can take on random shapes and may not even be localized. The degrees of freedom in choosing the unitary matrix $U_{mn}^{(\mathbf{k})}$, however, makes it possible to computationally search the optimum, in this case maximally localized, Wannier functions[114]. Pioneered by N. Marzari and D. Vanderbilt[115], efficient computational methods have been developed to calculate the maximally localized Wannier functions in real materials. Figure 2-4 illustrates both the

concept of Wannier functions and the calculated maximally localized Wannier functions in silicon.

With the maximally localized Wannier functions as the proper real space basis, the electron-phonon interaction matrix elements can be transformed into real space, and the long-range interactions can be cut off in real space beyond a certain distance. This so-called "Wannier interpolation" scheme was first developed by F. Giustino and S. Louie at UC Berkeley[116], and a computer program named EPW[104] has been developed for this interpolation scheme. This program is also used in this thesis with extensive modifications in terms of integration methods (discussed in the next section) and the capability of calculating transport properties.

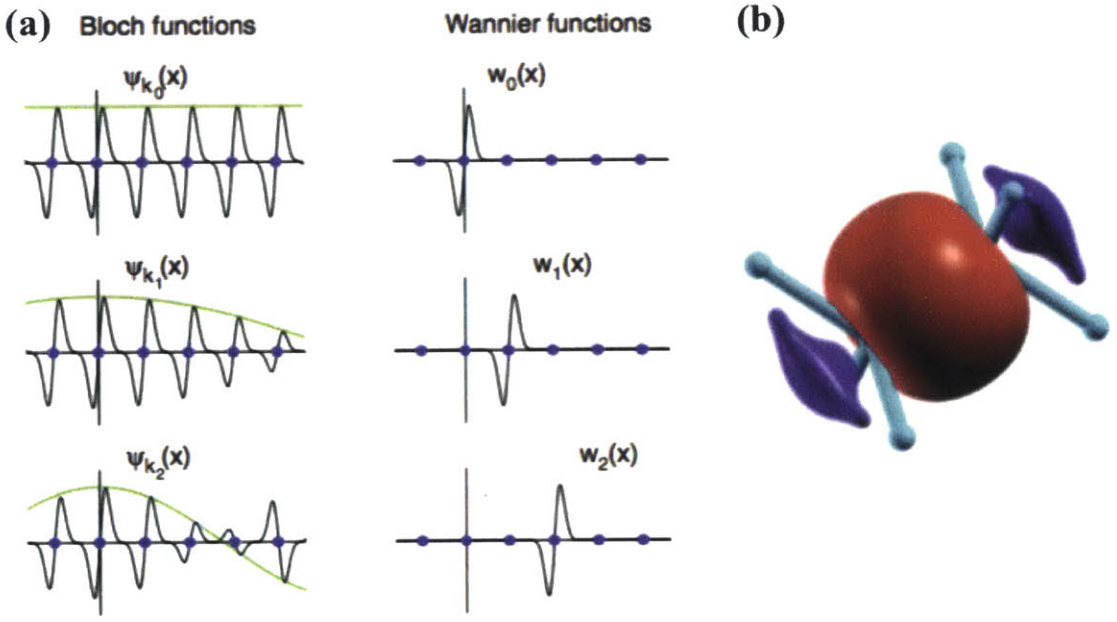

Figure 2-4 Illustrations of Wannier functions. (a) Schematic comparing the extended Bloch functions and localized Wannier functions. (b) Calculated maximally localized Wannier functions for silicon, using the four valence bands. Adapted from Ref. 114.

2.2.4 Integration Methods of the Scattering Rates

To carry out the sums in the Fermi's golden rule equations (2.10), (2.12) and (2.13), special treatments are needed due to the presence of the two δ-functions. One straightforward way to numerically treat the δ-functions is to replace them with Gaussians with a finite width. In this case the widths of the Gaussians (the "degauss" parameter) need to be compatible with the sampling mesh density, and both parameters need to be tested for convergence. Simple to implement, it is cumbersome to test convergence and more importantly, and some fine features in the calculation can be washed out by the Gaussian broadening. An alternative is to use the so-called "tetrahedral method"[117]. The idea is to divide the three-dimensional Brillouin zone into a large number of small tetrahedra, and assume linear energy dispersion within each tetrahedron

$$E = ak_x + bk_y + ck_z + d, \tag{2.15}$$

where the linear coefficients a, b, c and d can be uniquely determined by the calculated energies at the four vertices of the tetrahedron. When the tetrahedra are sufficiently small, the linear interpolation has only higher-order errors. With the interpolated linear energy dispersion relations, the Fermi's golden rules with δ-functions can be analytically integrated. In this case, the convergence of calculation only needs to be tested on the sampling mesh density, and sharp features in either the electronic band structure or the scattering profile can be captured. In two-dimensional calculations, an analogous triangular method[118] can be used. Tetrahedral and triangular methods are used in this thesis, except for the phonon-phonon scattering calculation, where the convergence issue is not as critical as the electron-phonon scattering calculation. Figure

2-5 shows the electronic density of states of phosphorene calculated using the triangular method, where sharp features near the band edges are well resolved.

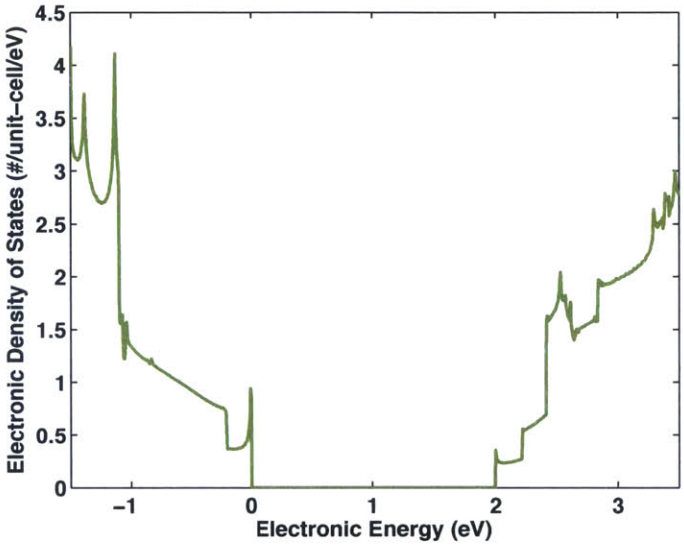

Figure 2-5 Electronic density of states of phosphorene calculated with a triangular integration method.

2.3 Fundamentals of Magnons

Another type of energy carriers studied in this thesis is magnons. Magnons, or quantized spin waves, are quantized excitations of a magnetic system, just as phonons are quantized excitations of a crystal lattice. On the physical origins, both phonons and magnons are Goldstone modes from broken continuous symmetries: the continuous translational symmetry in the case of phonons, and the continuous rotational symmetry in the case of magnons. Figure 2-6(a) illustrates the propagation of a magnon: spins on each lattice site possess a different phase of precession. The dynamics of the magnons is described by the Heisenberg Hamiltonian

$$H = \frac{\Gamma}{\hbar^2}\sum_{ij}\mathbf{J}_i \cdot \mathbf{J}_j, \tag{2.16}$$

where Γ is the exchange energy between two spins $\mathbf{J}_i$ and $\mathbf{J}_j$. In a ferromagnet, through a formal manipulation named "Holstein-Primakoff transformation"[119], the Heisenberg Hamiltonian can be expanded in a series analogous to the Taylor expansion Eq. (2.9). The first term in the series is the ground state energy $H_0 = N\Gamma J^2$, where N is the number of sites, and J is the spin quantum number. The second term in the series is $H_2 = \sum_{\mathbf{k}} \hbar\omega(\mathbf{k})\hat{a}_{\mathbf{k}}^{+}\hat{a}_{\mathbf{k}}$, where $\omega(\mathbf{k})$ gives the magnon dispersion relation, and $\hat{a}_{\mathbf{k}}^{+}$ and $\hat{a}_{\mathbf{k}}$ are creation and annihilation operators of magnons, respectively. In the simplest one-dimensional spin chain, the magnon dispersion relation is $\omega(k) = -\Gamma(1-\cos ka)$, where a is the lattice constant. This dispersion is shown in Fig. 2-6(b). In the small k regime, the dispersion is quadratic, in contrast to the linear dispersion of phonons. The next term in the series represents 4-magnon scattering processes. Unlike phonons, there are no three-magnon processes, due to the conservation of total angular momentum. And thus, although magnons are bosonic quasiparticles, their number is conserved when they only interact among themselves, and for this reason Bose-Einstein condensation of magnons has been observed[120].

One important and interesting feature of magnons is that their energy can be controlled by an external magnetic field through the Zeeman effect. Under an external magnetic field, the magnon dispersion is modified to $\omega(\mathbf{k}) = \omega_0(\mathbf{k}) + g\mu_B B$, where g is the Landé g factor, μ_B is the Bohr magneton, and B is the external magnetic field. Given the temperature, the energy of magnons directly affects their population, and this effect is analogous to electron transport, where the electric field also changes the energy

of electrons. With this observation, in Chapter 5 we develop a Boltzmann theory of magnon transport and describe a novel magnon cooling effect driven by an inhomogeneous magnetic field.

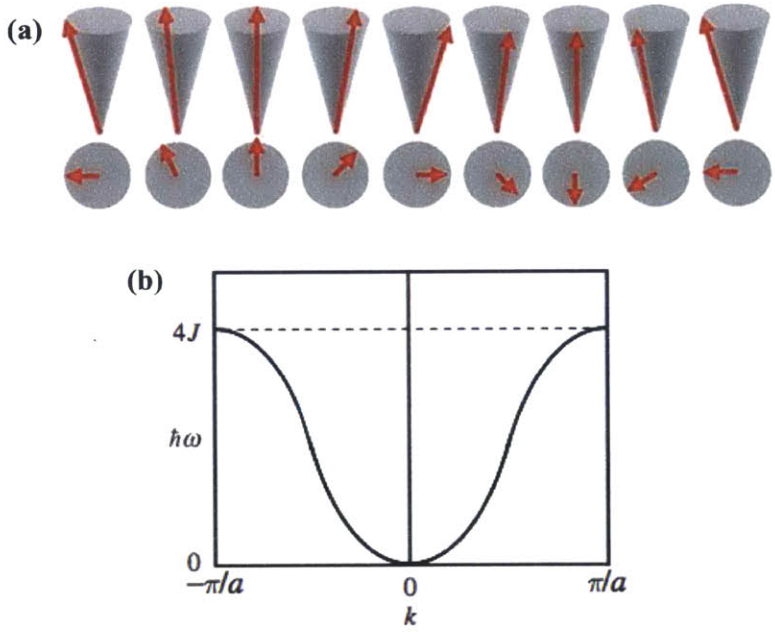

Figure 2-6 (a) Illustration of spin wave (magnon) propagation. Picture from internet:http://www.unimuenster.de/Physik.AP/Demokritov/en/Forschen/Forschungsschwerpunkte/mBECwam.html. (b) Magnon dispersion in a one-dimensional spin chain.

Chapter 3

Understanding Electron and Phonon Transport in Thermoelectrics from First-Principles

In this chapter we apply the first-principles simulation tools described in Chapter 2 to study the phonon-phonon interaction in a low-temperature thermoelectric material $FeSb_2$ and the electron-phonon interaction in a newly discovered two-dimensional semiconductor phosphorene. The most important transport properties we can extract from these calculations are the mean free path distributions of electrons and phonons, which provide practical guidelines in designing nanostructures to engineer the electrical and thermal transport properties of these materials.

3.1 Phonon-Phonon Interaction in $FeSb_2$*

3.1.1 Background

Thermoelectric materials are useful not only for generating electric power from heat, but also for providing cooling power by passing through an electric current[2,3,58,121–126]. Thermoelectric materials are especially attractive as refrigerating materials for being reliable, noiseless, and without any moving parts[3]. Recently, the compound $FeSb_2$ has attracted a significant amount of research interest as a promising thermoelectric material for cooling applications at cryogenic temperatures since it was experimentally found to show an ultra high Seebeck coefficient ($S \approx -42$ mV/K), and thus a large power factor ($PF \approx 2300\ \mu WK^{-2}cm^{-1}$) at $T = 12$ K [127]. Subsequent work was done for a better understanding of this material, and improving its thermoelectric efficiency[128–135]. The origin of the high Seebeck coefficient is still under debate. $FeSb_2$ has been characterized to be a strongly correlated semiconductor[136–138], or more specifically, a Kondo insulator[139,140], where a small hybridization gap (~10 meV) is formed at low temperatures as a result of the interaction between localized f- or d-orbitals (d-orbitals of Fe atoms in this case) with itinerant energy bands. Since f- and d-bands are in general quite flat, the resulting electronic structure is known to give large Seebeck coefficients[141]. This mechanism was recently verified in a model study of Kondo insulator nanowires using the dynamic mean-field theory[142]. Tomczak et al. studied the electronic structure and the corresponding Seebeck coefficient of $FeSb_2$ in detail from first-principles[143]. They obtained the electronic ground state of $FeAs_2$ and $FeSb_2$ including many-body effects

---

* B. Liao et al., Physical Review B, **89**, 035108 (2014)

using DFT with the GW approximation, and managed to reproduce temperature dependence of the Seebeck coefficient that was in good agreement with experiments in the intermediate temperature range but failed to explain the large peak of the Seebeck coefficient at lower temperatures for $FeSb_2$. On the other hand, Pokharel et al.[144,145] studied the correlation between the thermal conductivity and the Seebeck coefficient of $FeSb_2$ samples with different grain sizes, and suggested that the phonon-drag effect should be mainly responsible for the abnormal Seebeck coefficient.

Despite its high power factor, the single crystal $FeSb_2$ shows low zT due to its high lattice thermal conductivity ($k \sim 500$ W/mK at 12K)[127,131]. Thus it is the key for improving its thermoelectric performance to understand the thermal transport in $FeSb_2$ and to reduce its thermal conductivity accordingly. Compared to the abundant investigations of its electronic properties, only a handful of studies thus far looked into the thermal properties of $FeSb_2$. Lazarević et al.[146] calculated the phonon dispersion relation of $FeSb_2$ using density functional perturbation theory (DFPT) and studied some specific phonon modes using Raman spectroscopy experimentally. Diakhate et al.[147] also studied the harmonic properties of phonons and the lattice heat capacity using DFPT. No work so far, however, has been focused on the anharmonic properties of the lattice, and the phonon-phonon interactions, which largely controls the thermal transport properties of $FeSb_2$.

We here apply the first-principles formalism for the thermal conductivity calculation based on DFT and real-space lattice dynamics to $FeSb_2$ in order to understand its intrinsic phonon-phonon interactions and more importantly, to provide information on the phonon mean free path distribution, which is important in guiding the nanostructuring

strategy for effectively reducing its thermal conductivity[58,61,122,128]. The electronic structure is first obtained by DFT given the crystal structure, and then the interatomic forces can be calculated by DFT after directly displacing specific atoms from their equilibrium positions by a small amount according to the crystal symmetry. Provided the atomic displacements and the corresponding interatomic forces, in addition to the linear constraints imposed by symmetry, a least-square fitting procedure is invoked to extract the harmonic and anharmonic force constants[105], within which the phonon harmonic and anharmonic properties are encoded. The phonon dispersion relation, the phonon-phonon scattering rates, the lattice thermal conductivity and the mode-specific phonon mean free paths can then be calculated based on the force constants information[60].

3.1.2 Calculation Details

$FeSb_2$ crystalizes in an orthorhombic marcasite structure (space group Pnnm)[136], with 2 iron atoms and 4 antimony atoms in one unit cell, as shown in Fig. 3-1. Each iron atom is surrounded by 6 antimony atoms that are arranged in a deformed octahedron. The low symmetry of the crystal structure and the complexity of the unit cell render it a computationally challenging task to reliably attain the force constants of $FeSb_2$.

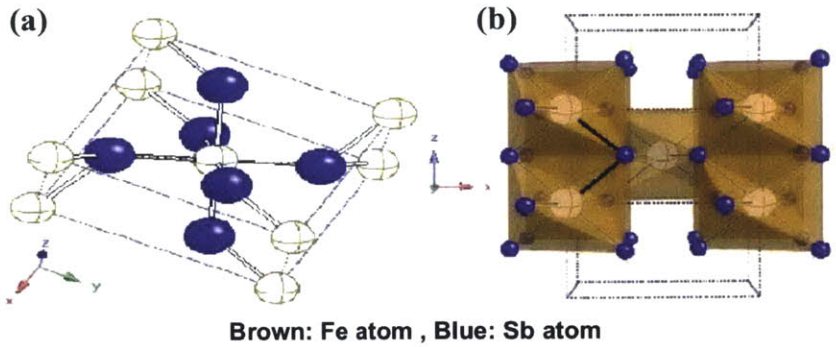

Figure 3-1 Crystal structure of $FeSb_2$. Adapted from Ref. 136.

We used the Quantum ESPRESSO package[103] for the DFT calculation, with norm-conserving Perdew-Zunger local density approximation (LDA) pseudopotentials[148]. We chose the plane-wave cut-off energy as 120 Ryd and a $16\times16\times16$ k-mesh for the self-consistent field (SCF) calculation to guarantee well-converged interatomic forces. The crystal structure was fully relaxed, and the resulting lattice parameters were $a = 5.743$ Å, $b = 6.414$ Å and $c = 3.102$ Å, ~1% smaller than the experimental values at $T = 20$ K [136]. To obtain long-range force constants, supercells with distinct sizes ($2\times2\times2$, $1\times1\times4$, $1\times4\times1$ and $4\times1\times1$) were constructed. Specific atoms in a unit cell were displaced systematically by amounts of 0.01Å, 0.02Å and 0.04Å along different coordinate directions from their equilibrium positions, and the interatomic forces were calculated for each configuration. Several configurations with random atomic displacements were added to improve the quality of the dataset for fitting the force constants. In the least-square fitting procedure, 18 neighbor shells were included for the harmonic (second-order) force constants, and 9 neighbor shells for the anharmonic (third-order) force constants, which amounted to 200 second-order and 1365 third-order independent force constants. It is worth noting that due to the low symmetry of the crystal, the 18th neighbor shell is only ~ 6.4 Å away from the atom at the origin, and the 9th neighbor shell goes to ~ 5.2 Å away. The absence of longer-range interactions due to the limitation of the computing resource might contribute to the errors and uncertainties in the simulation result, as will be discussed later.

3.1.3 Results and Discussion

After the harmonic force constants were extracted, the phonon dispersion relations could be calculated by solving for the eigenvalues of the dynamical matrix

constructed from the harmonic force constants[60], as shown in Fig.2-3. Our calculated phonon dispersion relations were in very good agreement with other calculations[146,147] using DFPT, indicating that the extraction of the harmonic force constants was reliable. It is relatively harder to validate the anharmonic force constants. The mode-specific Grüneisen parameters, $\gamma_{n,q} \equiv -\frac{d\ln\omega_{n,q}}{d\ln V}$, where $\omega_{n,q}$ is the frequency of a specific phonon mode, and V the volume of the crystal, quantify the anharmonicity of the lattice at a microscopic level, and can be computed directly from the anharmonic force constants[60]. Being hard to measure in experiments, the Grüneisen parameters manifest themselves in all other measurable quantities that resulted from the lattice anhamonicity, for example the bulk thermal expansion coefficient[60,149] $\alpha = \frac{\Gamma c_p}{3B}$, where Γ is the averaged Grüneisen parameter weighted by the mode-specific heat capacity, c_p the total heat capacity and B the bulk modulus. We first calculated the bulk thermal expansion coefficient and compared it to the experimental data[136], as shown in Fig.3-2. Good agreement was achieved at very low temperatures, while at higher temperatures, deviations from the experimental data were observed. As discussed by Petrovic et al[136], the peak structure in the thermal expansion coefficient can possibly be attributed to the Shottky peak in the electronic specific heat associated with narrow band gap semiconductors, which can not be captured in our simulation.

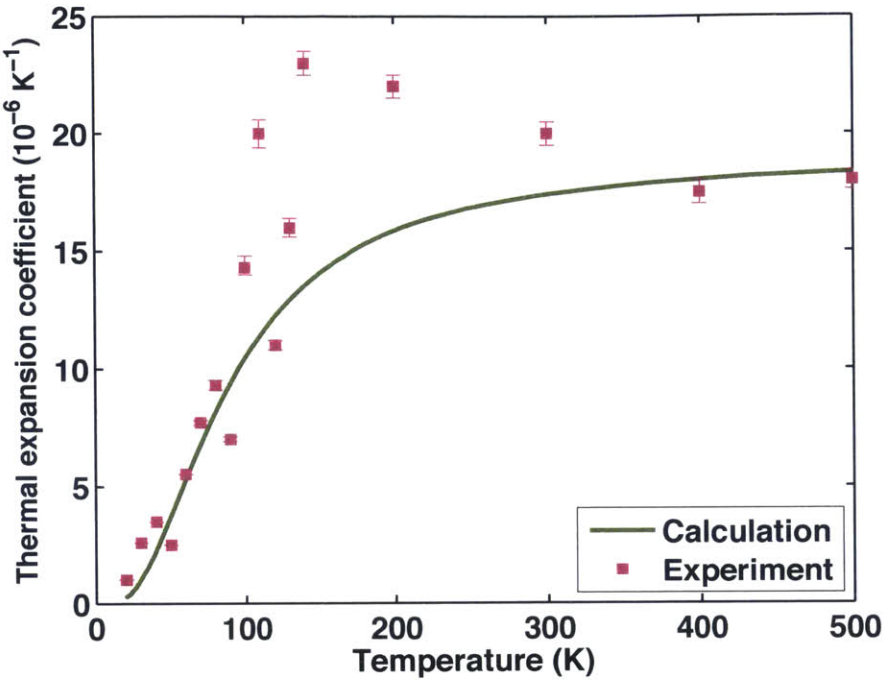

Figure 3-2 The calculated and experimental thermal expansion coefficient of $FeSb_2$. The experimental data is extracted from Ref. 136.

Moreover, we calculated the mode-specific Grüneisen parameters via two different approaches and compared the results in order to check the self-consistency of our simulation. One approach was to manually scale up the size of the crystal by a small amount (0.01% in this case) and to recalculate the phonon dispersion relations so that the mode specific Grüneisen parameters could be computed by the finite difference method from the definition; the other approach was to compute the Grüneisen parameters directly from the anharmonic force constants. The results are plotted in Fig. 3-3. No perfect match was observed due to the absence of contributions from higher order force constants and farther away atomic layers that were not included in the simulation when calculating the Grüneisen parameters directly from the anharmonic force constants. Especially the deviations in the acoustic modes were caused by the fact that the size of the supercells that could be handled was very limited given the complexity of the unit cell. Nevertheless

the general trend and the range of the dispersion of the numerical values were consistent between the two approaches, indicating that a reasonable degree of convergence in terms of the number of neighbor shells and the force constants was reached in our calculation.

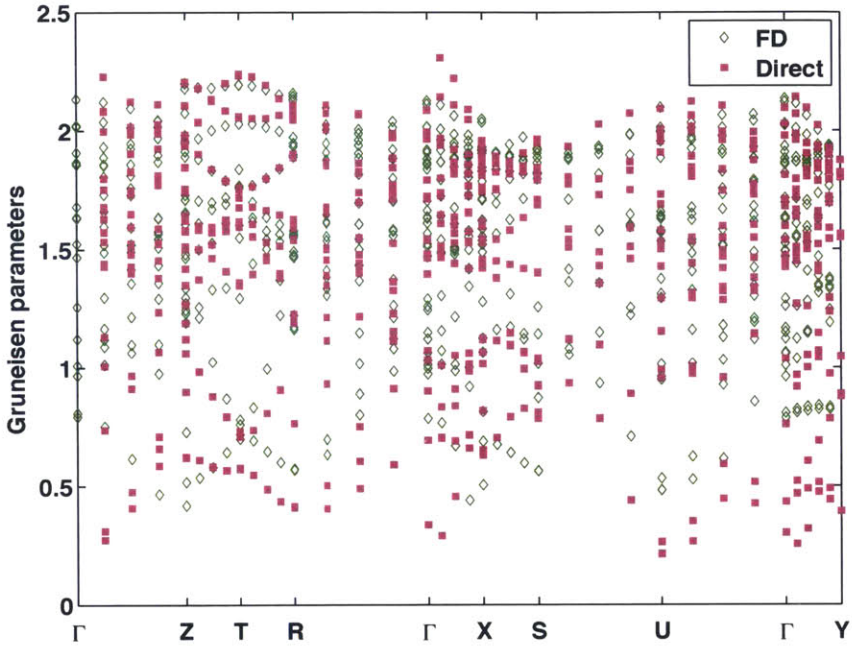

Figure 3-3 The comparison of mode-specific Grüneisen parameters calculated with two different approaches: finite difference (FD) and direct calculation from third order interatomic force constants.

Of great interest are the phonon-phonon scattering rates that can be calculated from the extracted force constants using Fermi's golden rule[60]. The scattering rates for both normal processes and Umklapp processes at $T = 20$ K are plotted in Fig.3-4. The scattering rates of the acoustic modes and optical modes are plotted separately. A quadratic dependence of the normal scattering rates of acoustic phonons on frequency can be seen from the plot, while the scattering rates of the acoustic phonons for Umklapp processes seem to scale as ω^3, a fact that is quite similar to silicon[60]. It is noticed that at $T = 20$ K the phonon scattering rates are in general quite low, and the phonon mean free

paths can be comparable to the sample size, implying that boundary scattering should be included when calculating the thermal conductivity.

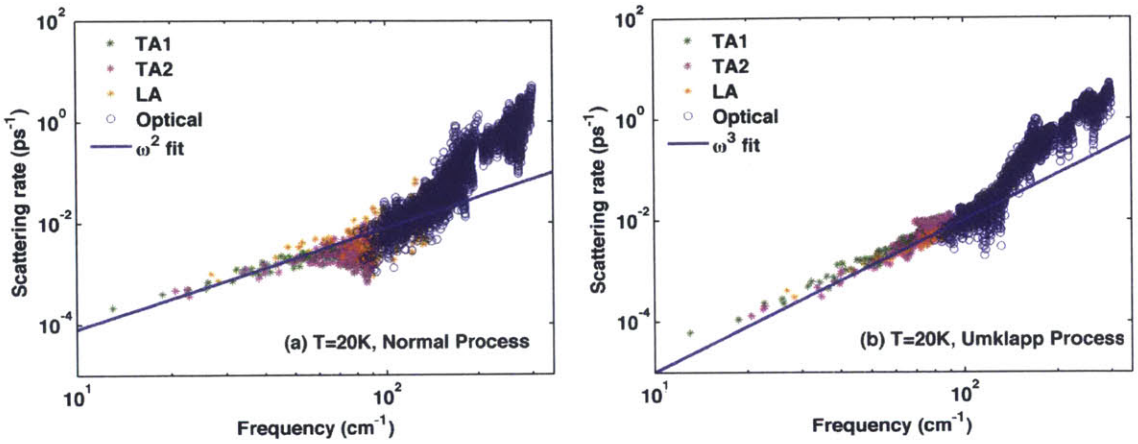

Figure 3-4 The calculated phonon-phonon scattering rates due to (a) normal processes and (b) Umklapp processes in $FeSb_2$ at 20K.

A finite mesh when sampling the Brillouin zone leads to errors in calculating the lattice thermal conductivity, due to the missing contributions of phonon modes with very long wavelengths. This numerical artifact can be compensated by extrapolating the results of calculations with a finite mesh of different sizes according to the following relation[60,150]

$$\frac{\kappa_n(T)}{\kappa_\infty(T)} = 1 - \frac{c(T)}{n_k} + \mathrm{O}\left(\frac{1}{n_k^2}\right), \tag{3.1}$$

where the coefficient $c(T)$ can potentially depend on temperature (at higher temperatures, the phonon-phonon dominant thermal conductivity $\kappa_0(T) \sim T^{-1}$, leading to a temperature-independent c [150]. Otherwise $c(T)$ will depend on the temperature), n_k is the number of sampling points in one dimension, κ_n is the corresponding calculated lattice thermal conductivity, and κ_∞ is the extrapolated lattice thermal conductivity

corresponding to infinite sampling points. Calculations with $6\times6\times6$, $8\times8\times8$ and $10\times10\times10$ sampling meshes were conducted for extrapolation. The extrapolation is illustrated in the inset of Fig. 3-5, where the linear relation Eq. (3.1) is found to hold at different temperatures, and $c(T=20\text{K})$ is distinct from those of higher temperatures as expected, since the scaling $\kappa_0(T)\sim T^{-1}$ starts at higher temperatures. The extrapolated thermal conductivity is plotted in Fig. 3-5, and is compared to the experimental data from Bentien et al.[127] and Sun et al.[131]. Our calculation overestimates the thermal conductivity of $FeSb_2$, and it is understandable and expected because at the temperature range that we are interested in, the sample boundary scattering and impurity scattering play important roles compared to the phonon-phonon scattering under investigation. We can incorporate these two effects using model relaxation times via Matthiessen's rule. We use the Casimir model[151] for the sample boundary scattering, i.e. $\frac{1}{\tau_{BS}}=\frac{v}{l}$, where τ_{BS} is the relaxation time due to sample boundary scattering, v is the mode dependent group velocity and l is the characteristic size of the sample that we chose as a fitting parameter. We also add a Rayleigh-type term accounting for the impurity scattering[152], $\frac{1}{\tau_{IS}}=A\omega^4$, where A is used as another fitting parameter. The consideration of boundary scattering and impurity scattering in this manner is not from a *first-principles* approach and provides less essential information on phonon transport in $FeSb_2$ since these procedures are sample-dependent, but we chose to adopt the two models for data fitting just to show that they were still insufficient to explain the experimental data even with the extra two scattering mechanisms. One such fit is shown in Fig. 3-5. The fitting parameters in this case are $l=0.5$ mm and $A=3.7\times10^{-41}$ s^3. While one could bring down the calculated thermal

conductivity to the experimental level at lower temperatures, the deviations at higher temperatures are still apparent. In fact, our calculations follow the typical T^{-1} trend for a phonon-phonon dominant system quite well, whereas the experimental values fall on a $T^{-1.7}$ fit at higher temperatures. Although the exclusion of the contributions from longer-range atomic interactions and higher-order force constants could result in errors in our calculations, their inclusion would not alter the 1/T temperature-dependence. Thus we suspect that this deviation is caused by the omission of other scattering mechanisms specific to the $FeSb_2$ system, either due to electron-phonon interactions (the phonon drag effect) or to electron correlations. It is also worth noting that the way the lattice thermal conductivity was extracted from the experiments was to subtract the electronic contribution from the measured total thermal conductivity, and the electronic contribution was estimated using the Wiedemann-Franz law with a metallic Lorenz number $L_0 = 2.44 \times 10^{-8}\ \mathrm{W\Omega K^{-2}}$ in both the references[127,131]. And as commented in the references[127,131], the electronic contribution has a significant magnitude compared to that from the phonons at temperatures above 100 K. Given the strong correlation among electrons, it is probable that the Wiedemann-Franz law, or the metallic Lorenz number are no longer valid in this system. Furthermore, the strongly correlated electron dynamics could also lead to different phonon behaviors via the phonon-electron interactions. These complications still require further investigations in the future.

To further examine the thermal conductivity, we decomposed the total thermal conductivity into contributions from different modes, as shown in Fig. 3-6. Below 50K, the acoustic phonons dominate the thermal conduction since the population of the optical modes is very small. At higher temperatures, however, the contributions from the optical

modes gradually become significant, taking up to ~33% at 200K. Optical phonons typically do not contribute much to the total thermal conductivity due to their low group velocities and short mean free paths[153]. In $FeSb_2$, the hybridization of the optical phonon bands with the longitudinal acoustic (LA) mode and among themselves results in significant band dispersion and higher group velocities, as can be observed in the phonon dispersion plot in Fig. 2-3, which is one reason for the significant contribution from optical modes at higher temperatures.

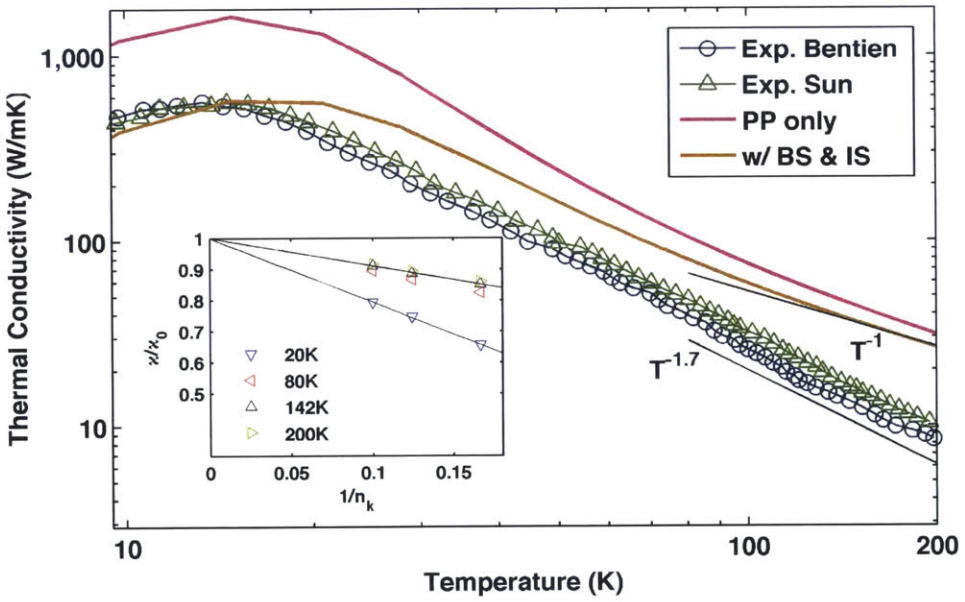

Figure 3-5 The comparison between the calculated and experimental thermal conductivity of $FeSb_2$. The magenta line represents the calculation result with only phonon-phonon interactions, and the brown line represents calculation result including boundary and impurity scatterings. The inset illustrates the linear extrapolation to compensate for the finite sampling mesh problem.

In Fig. 3-7 the thermal conductivities along different crystal axes are plotted. The thermal conductivity along c axis is about half of those along a and b axes at low temperatures, and this anisotropy diminishes at higher temperatures. The low-temperature anisotropy can be possibly attributed to two causes: the group velocity anisotropy and the

phonon-phonon scattering anisotropy. The former can be ruled out by the calculated sound velocities by Diakhate et al.[147], where the average sound velocities do not show significant direction-dependence. To check the latter, we present in Fig. 3-8 the correlation between the total relaxation time and the group velocity components of the acoustic modes that dominate the low temperature thermal conduction. It is observed that those phonon modes with large group velocities along c axis mainly reside in the short-relaxation-time region, whereas the modes with the longest relaxation times also possess large group velocity components along a and/or b axes. This result confirms that the origin of the lower temperature anisotropy lies in the anisotropic phonon-phonon scattering.

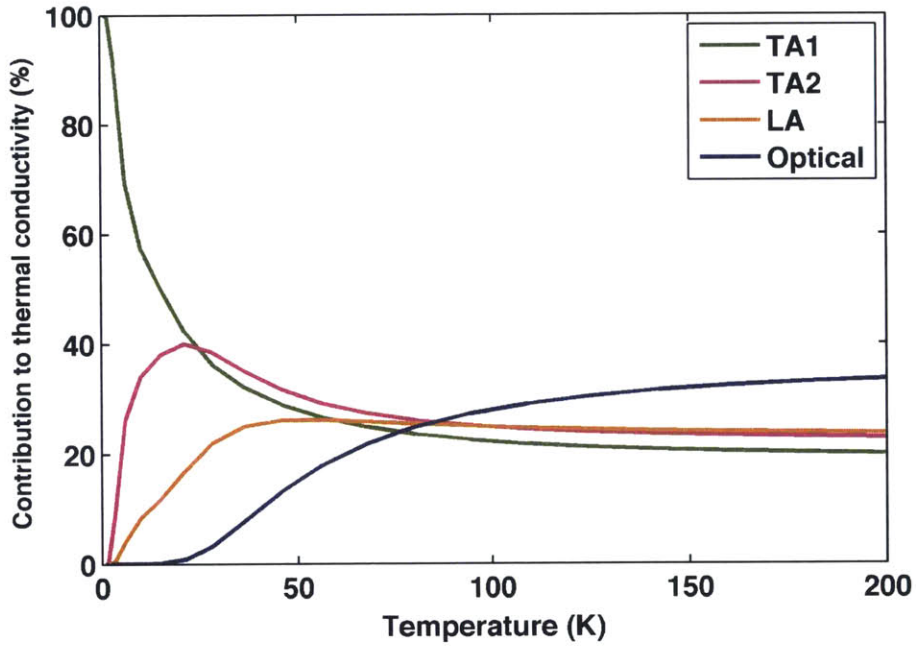

Figure 3-6 The contributions of different phonon modes to the total thermal conductivity of $FeSb_2$ at different temperatures.

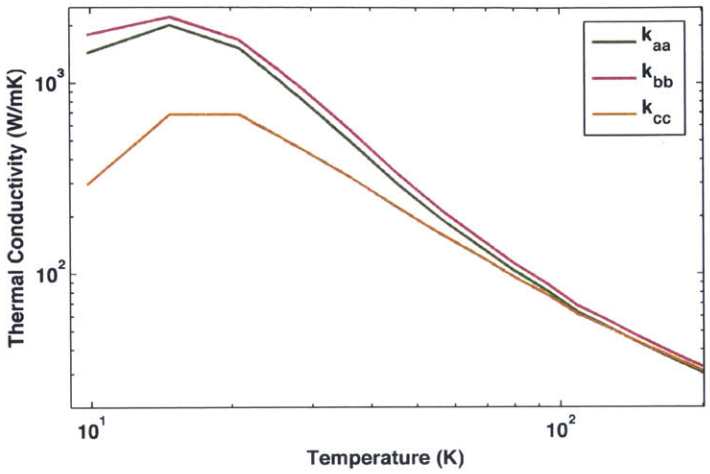

Figure 3-7 The thermal conductivity of $FeSb_2$ along different directions, showing the anisotropic thermal transport.

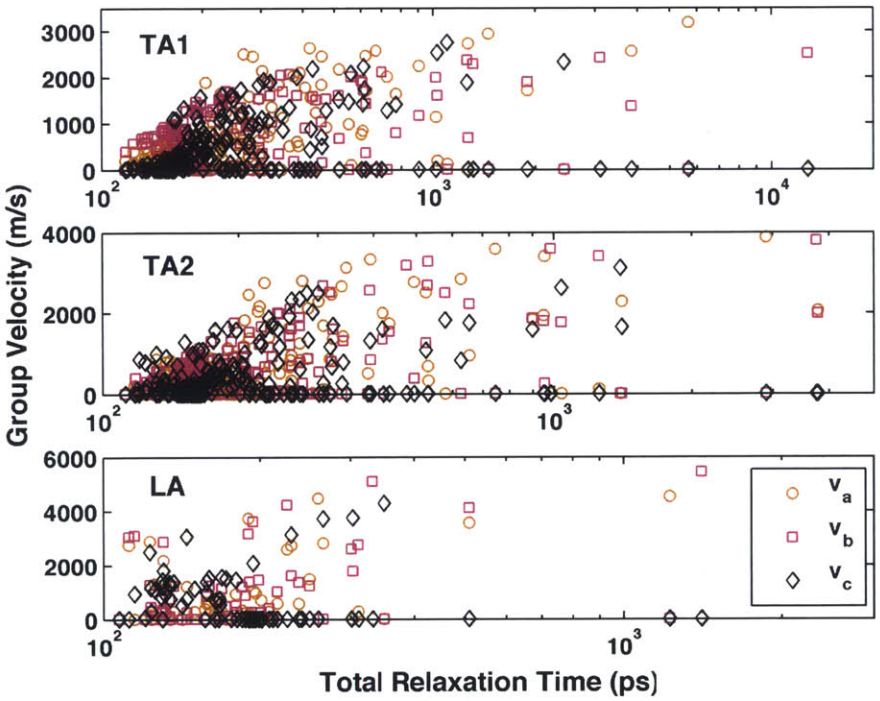

Figure 3-8 The correlation between the group velocity directions and the total relaxation time, illustrating that the anisotropic thermal transport is due to anisotropic scattering.

Although no perfect match was achieved with the experimental data, we believe the simulation still provides valuable information on the lattice dynamics in $FeSb_2$ as a

first attempt to understand the anharmonic processes from first principles of a crystal with a complex structure and possible strong electron correlations, and thus could serve as a basis for future theoretical and experimental investigations. In Fig. 3-9 we present the accumulated thermal conductivity with contributions from phonon modes with different mean free paths due to the phonon-phonon scattering alone. From Fig. 3-9, the phonon mean free paths are quite long at $T = 20$ K , and concentrated in the range 1~200 μm, indicating that it could be an effective way to reduce the lattice thermal conductivity of $FeSb_2$ by introducing nanostructures, such as grain boundaries and nanoinclusions, with characteristic sizes smaller than 1 μm, which has been readily verified in the work of Zhao et al.[128].

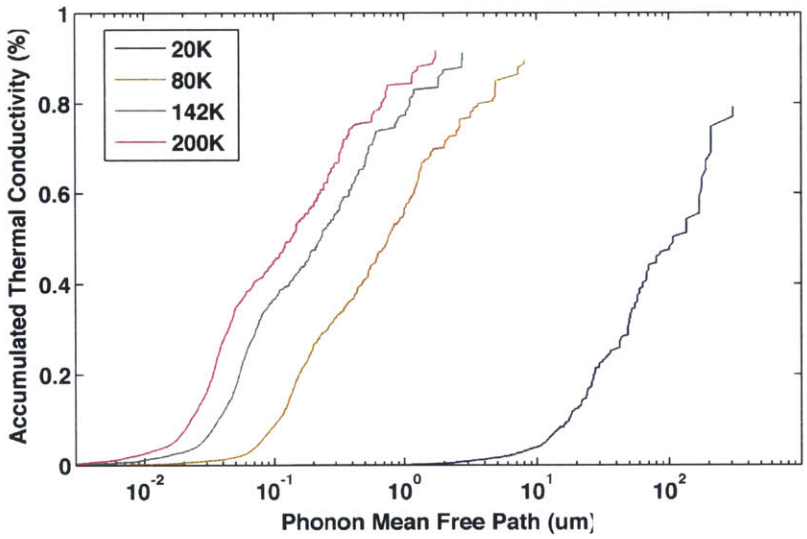

Figure 3-9 Phonon mean free path distribution in $FeSb_2$ and their accumulated contribution to the total thermal conductivity, at different temperatures.

In summary of this section, we studied the thermal transport properties of $FeSb_2$ using a first-principles formalism based on DFT and real-space lattice dynamics. Calculations of the electronic structure, the phonon dispersion relation, the phonon-phonon scattering rates, the lattice thermal conductivity and the phonon mean free path

distribution were presented, which could be of value for future theoretical and experimental studies of $FeSb_2$. The discrepancy with the experimental data suggests that more work needs to be done in the future to better understand the thermal transport in $FeSb_2$. This could include looking into the possible effect of strong electron correlations, electron-phonon interactions and higher order anharmonic processes on the thermal transport which has not before been systematically investigated to the best of our knowledge.

3.2 Electron-Phonon Interaction and Thermoelectric Transport in Phosphorene[†]

3.2.1 Background

20 years ago, Hicks and Dresselhaus predicted that low dimensional conductors could have better thermoelectric performance compared with their 3-dimensional bulk counterparts, mainly owing to the quantum confinement effect[11,12]. In particular, the electronic density of states in low-dimensional systems usually exhibit sharp changes with respect to the carrier energy, which is of significant benefit for improving the Seebeck coefficient[13]. In the past two decades, researchers have widely utilized the much-advanced nanotechnology to boost the thermoelectric performance using various approaches[122,154]. Experimentally, artificial low-dimensional structures, such as quantum dots[14], quantum wells[15], superlattices[16,17], a 2-dimensional electron gas[19] and nanowires[18,155] have all been studied for enhancing thermoelectric properties. These

---

[†] B. Liao et al., Physical Review B, **91**, 235419 (2015)

structures, however, are difficult to scale up due to the complexity of the fabrication process and the high cost.

Immediately after the first successful isolation of graphene[156], a stable monolayer of carbon, the look into natural low-dimensional conductors for good thermoelectrics started, in the hope that these materials are easier to obtain at a lower cost[157–159]. Unfortunately, graphene itself turns out to be a not-so-good thermoelectric material, because of 1) the high electron-hole symmetry and the absence of a bandgap, which results in large detrimental bipolar conduction; 2) the linear dispersion for low-energy excitations, which leads to a smooth quadratic density of states without the preferred sharp features; and 3) an ultra-high lattice thermal conductivity[160,161], in part coming from the large contribution of the less-scattered flexural phonon mode[162] (there have been theoretical works suggesting that the classical size effect in nanostructured graphene can largely reduce its lattice thermal conductivity[163,164]). Along these lines, natural 2-dimensional materials with a sizable bandgap, quadratic low-energy dispersion, and suppressed flexural phonon modes have been sought as better candidates for thermoelectrics, in addition to the generally preferred high carrier mobility. Some subsequently synthesized/isolated 2-dimensional materials usually fit some of the above criteria, but for most cases they also possess serious drawbacks. For example, a monolayer of the transition-metal dichalcogenide MoS_2 comes with a bandgap while being limited by its relatively low carrier mobility[165,166]; silicene and germanene, monolayers of silicon and germanium atoms arranged in honeycomb lattices, possess similar low-energy electronic structures as that of graphene, but with very small band gaps (a few meV), which only arise from spin-orbit coupling[167,168].

Recently, a new member of the 2-dimensional-material family, single layers of black phosphorus dubbed "phosphorene", has emerged and attracted intense research interest[169–176]. In a phosphorene layer, phosphorus atoms are arranged in a puckered honeycomb lattice[177] with low symmetry and high anisotropy, as illustrated in Fig. 3-10.

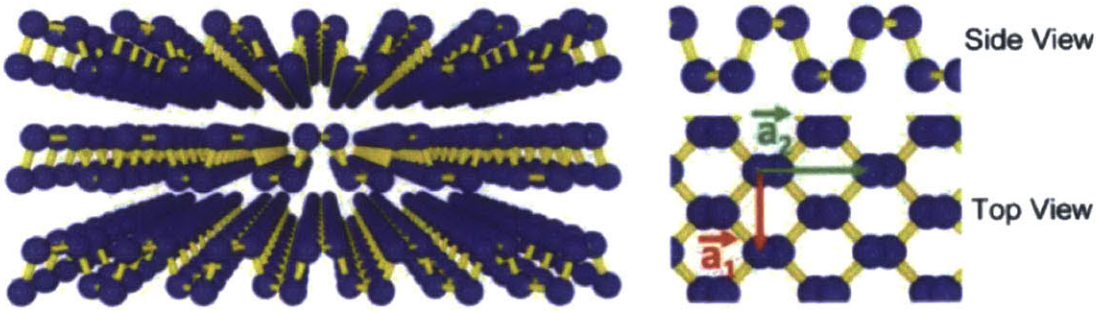

Figure 3-10 The puckered honeycomb structure of a single layer of black phosphorus, or phosphorene. Adapted from Ref. 169.

This hinge-like puckered structure leads to intriguing mechanical properties, such as a negative Poisson ratio[178]. The resulting electronic structure is also highly anisotropic, with a fundamental bandgap of 2 eV[179] that can be potentially tuned either by changing number of layers[169], controlling the edge termination and the width of a ribbon[180] or imposing a strain[181,182]. The low-energy dispersion is quadratic with very different effective masses along armchair and zigzag directions[179] for both electrons and holes. This anisotropic electronic structure is useful for thermoelectric materials, since in the direction with a smaller effective mass, the carrier mobility and thus the electrical conductivity can be high, while the larger effective mass along the other direction contributes to an overall large density of states that improves the Seebeck coefficient. Moreover, few-layer black phosphorous has been experimentally found to exhibit high carrier mobility, especially for holes[169–171,183,184], while the theoretical calculations on single-layer phosphorene have suggested even higher values[179,185], and the possible

tunability via applying a strain[186,187]. These features have stimulated lots of research efforts in evaluating the potential thermoelectric performance of phosphorene. Qin et al. simulated the lattice thermal conductivity of phosphorene from first-principles[188], showed that the thermal transport was also highly anisotropic, and revealed that the much reduced lattice thermal conductivity compared with graphene could be largely attributed to the suppressed flexural mode. Jain et al. refined the lattice thermal conductivity calculation using the full iterative solution of the Boltzmann transport equation[189]. Fei et al. pointed out that the directions with higher electrical and thermal conductivity, respectively, in phosphorene are orthogonal to each other, which leads to a promising thermoelectric figure of merit along the armchair direction, exceeding 2 at 500K[179].

Although aforementioned works have studied the thermoelectric properties of phosphorene in some detail, the treatment of electron-phonon interaction in phosphorene has been limited to the constant relaxation time approximation for calculating the Seebeck coefficient, and limited to the deformation potential approximation for calculating the electrical conductivity. In particular, the existing deformation potential calculations[179,185] obtained separate deformation potentials for different transport directions by deforming the lattice along that direction. The validity of such an approach is questionable because the deformation along one direction will scatter electrons going in all directions. In the present work we study the electron-phonon interaction in phosphorene fully from first-principles. We find that the deformation potential calculations tend to overestimate the carrier mobility, and we fully assess the potential of phosphorene as a thermoelectric material based on our simulation results.

3.2.2 Methods and Details of the Calculation

We first carry out the standard density functional theory calculation of the electronic structure of phosphorene after obtaining a fully relaxed crystal structure using the Quantum Espresso package[103] and a norm-conserving pseudopotential with the Perdew-Wang exchange-correlation functional within the local density approximation[190]. We use a 200×200 k-mesh and the triangular integration method[118] to generate an accurate electronic density of states. The phonon dispersion and the electron-phonon scattering matrix elements are calculated within density functional perturbation theory[106], initially on a coarse 10×10 q-mesh, and then along with the electronic structure on a coarse 10×10 k-mesh, are interpolated using the EPW package[104,116] to a dense 300×300 k-mesh covering half of the Brillouin zone centered around the Γ point and a 300×300 q-mesh in the full Brillouin zone using maximally localized Wannier functions[114] for calculating the electronic relaxation time due to the electron-phonon interaction, which is given by the Fermi's golden rule[110] Eq. (2.12). The summation is performed using the triangular method[118] to improve the convergence, and to eliminate the need of choosing the Gaussian broadening parameter when doing the summation using Gaussian functions to approximate the delta functions. The calculated electronic relaxation times are then plugged into the standard formulae of the transport properties based on the Boltzmann transport equation[10], Eqs. (2.3) to (2.5), except in this case the sums are taken directly over all individual modes, and the density of states is not used. A similar calculation scheme has been applied by other researchers to studying the electron-phonon interactions in graphene[191,192]. The power of this *ab initio* approach lies in the fact that individual carrier states can be analyzed separately in terms of the time and

length scales associated with their transport, given by the electron-phonon relaxation time $\tau_e^{ep}(\mathbf{k})$ and the carrier mean free path $l_e^{ep}(\mathbf{k}) \equiv \tau_e^{ep}(\mathbf{k})|\mathbf{v}_\mathbf{k}|$ that characterizes the average length a carrier can travel before getting scattered by a phonon, respectively. This information provides crucial guidance in designing nanostructured thermoelectric materials, as will be discussed in a later subsection.

3.2.3 Results and Discussion

The electronic band gap is underestimated to be 0.8 eV, and is a well-known problem of density functional theory. The more accurate band gap of 2 eV from the GW calculation[179] is imposed in the following calculations by rigidly shifting the bands. The electronic density of states is shown in Fig. 2-5, where well-defined step-like features specific to 2-dimensional quadratic bands are observed, as well as quasi-1-dimensional peaks near the band edges as a result of the high anisotropy, since both the lowest conduction band and the highest valence band are very flat along the zigzag direction, resembling 1-dimensional bands along the armchair direction, which signals a high Seebeck coefficient. This feature is reminiscent of the quasi-2-dimensional bands in good bulk thermoelectrics, such as PbTe and PbSe[193].

We proceed to calculate the scattering rates and mobility for free carriers in phosphorene as limited by electron-phonon interactions. We exclude contributions from the flexural phonon modes for two reasons: 1) out-of-plane vibrations do not contribute to the first-order electron-phonon interactions in 2D materials due to the inversion symmetry with respect to the material plane, as in the case of graphene[192,194] (although the flexural phonon modes in phosphorene have small in-plane components as well, their contributions are negligibly small); 2) so far in most experiments phosphorene samples

are studied on a substrate, by which the flexural phonons will be largely suppressed. The scattering rates are presented in Fig. 3-11, and compared with the deformation potential calculation using parameters from Qiao et al.[185]. At each electronic energy, electrons with different wavevectors in general have different scattering rates due to the direction-dependence of the electron-phonon scattering, and thus the plotted scattering rate is multi-valued at each electron energy. Although the deformation potential approximation is not rigorously applicable in this case due to previously mentioned reasons, in general it gives reasonable estimates of the average strength of the electron-acoustic-phonon interactions in phosphorene, except for the case of holes in the zigzag direction, where the predicted scattering rate using the deformation potential approximation is 3 orders of magnitude lower than our result, and a hole mobility of 26,000 cm^2/Vs was predicted accordingly[185]. Our results indicate that the contributions from optical phonons are not negligible, especially for carriers slightly away from the band edges. More importantly, we observe peak structures of the scattering rates near the band edges, similar to the density of states. This can be explained by the high anisotropy of the band structure. According to Eq. (2.12), the scattering rate of a specific carrier state depends on the available phase space for the final states. In other words, the large number of carrier states along the zigzag direction provides a large number of available final states to be scattered to for carriers traveling along the armchair directio. In this way the carrier transport along the two directions are coupled through the electron-phonon interaction and the electron-phonon scattering rates follow the trend of the total density of states.

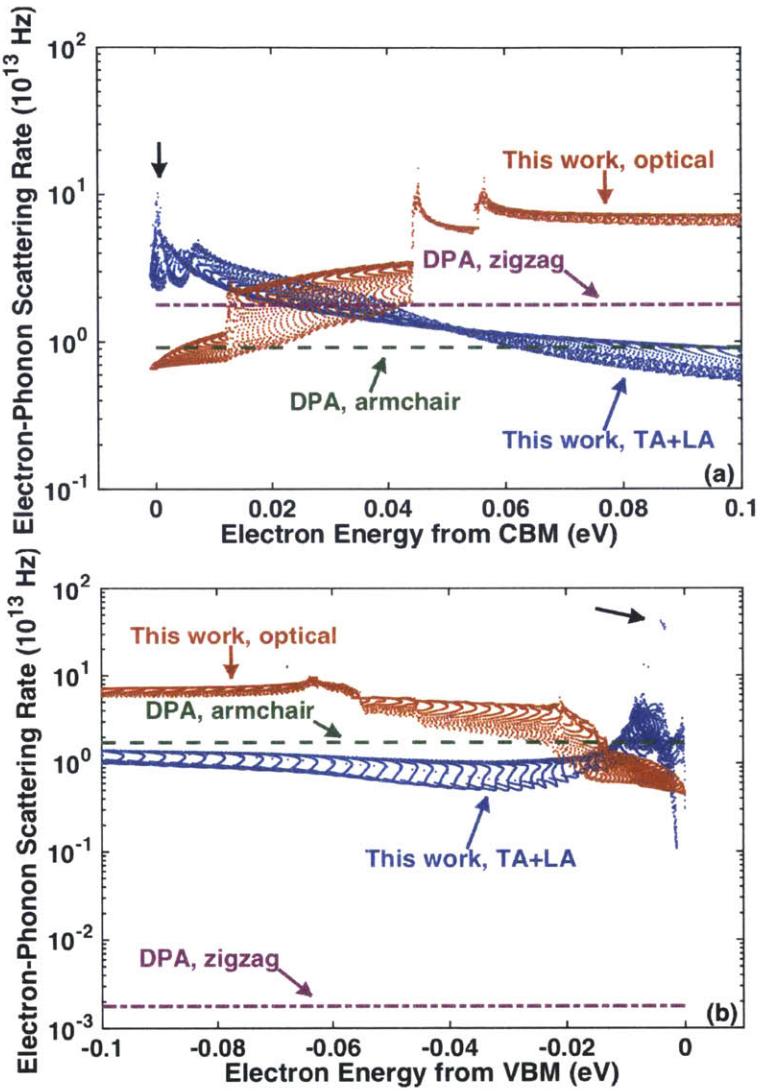

Figure 3-11 The comparison of the calculated electron-phonon scattering rate of (a) electrons and (b) holes to the deformation potential calculation in Ref. 185. The black arrows mark the peak structures of the scattering rates near the band edges.

The peak structures of the scattering rates near the band edges are expected to have a major impact on the carrier mobility since carriers near the band edges contribute the most to the carrier transport. We show here in Fig. 3-12 the carrier mobilities of electrons and holes along armchair and zigzag directions at 300K, with respect to the carrier concentration. We simulate the effect of carrier concentration by rigidly shifting the Fermi level, assuming the electronic band structure is not greatly affected by free

carriers. We predict that the phonon-limited carrier mobility of phosphorene is ~170 cm^2/Vs for both electrons and holes along the armchair direction at 300K and that there is a moderate anisotropy between the two transport directions. Experimentally Xia et al.[171] measured the hole mobility of a 15 nm thick (~30 atomic layers) black phosphorous sample to be ~600 cm^2/Vs and that of an 8 nm thick (~15 atomic layers) sample to be ~400 cm^2/Vs, and more recently Xiang et al.[184] measured the hole mobility of a 4.8 nm thick (~8 atomic layers) sample to be ~200 cm^2/Vs, all measured along the armchair direction. The decreasing trend of the hole mobility with decreasing number of atomic layers was previously attributed to the sample quality degradation[171]. As shown by Qiao et al.[185], the hole effective mass along the zigzag direction increases from 0.89 to 6.35 as the number of atomic layers decreases from 5 to 1, while the hole effective mass along the armchair direction stays unchanged. As we discussed in the previous section, the high anisotropy and large effective mass along the zigzag direction provides a large phase space for the electron-phonon scattering processes and gives rise to the peak structures of the scattering rates near the band edges. Therefore our finding suggests that the drastically increased anisotropy with decreasing number of atomic layers[185] could also contribute to the observed reduction of the carrier mobility, and thus the single-layer phosphorene may not be the best option for high-mobility applications.

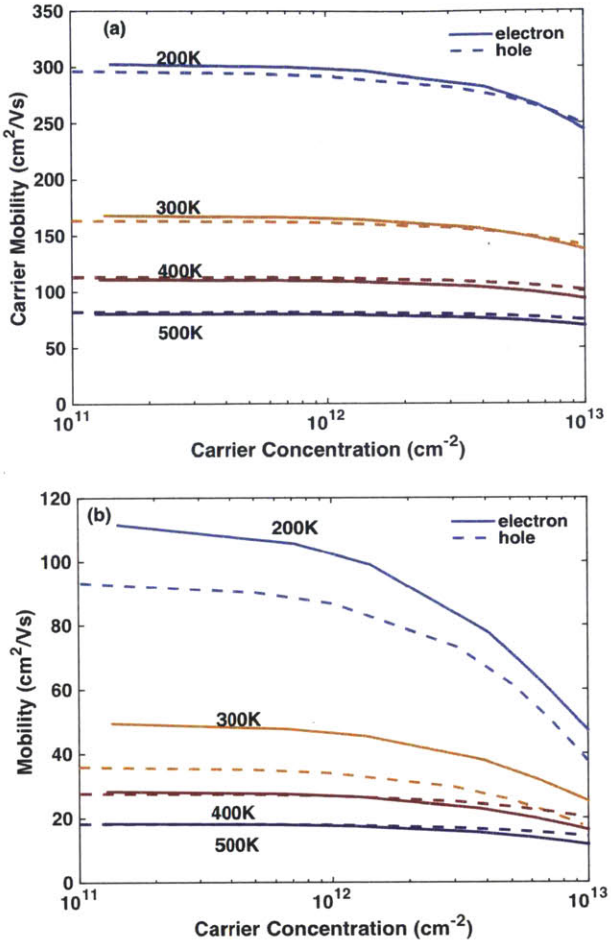

Figure 3-12 The calculated carrier mobility for electrons (solid line) and holes (dashed line) for phosphorene: (a) along the armchair direction and (b) along the zigzag direction at different temperatures; all plotted versus the carrier concentration.

In Fig. 3-13 we show the calculated Seebeck coefficient and thermoelectric power factor along the armchair direction for both p-type and n-type phosphorene, at various carrier concentrations and temperatures. In calculating the electrical conductivity, the thickness of the phosphorene sheet is chosen as the interlayer distance in bulk phosphorous, 0.55 nm[179]. Although this conventional choice seems somewhat arbitrary, it will not affect the thermoelectric figure of merit zT because the same factor appears in the thermal conductivity as well. Owing to the special features of the electronic structure

mentioned above, the Seebeck coefficient is high, and the thermoelectric power factor reaches ~70 μW/cm-K^2 in p-type phosphorene at room temperature. This number is comparable to that in state-of-the-art bulk thermoelectric materials, such as BiTeSb alloy[58] (the arbitrariness of choosing the film thickness may render this comparison unfair, to some extent).

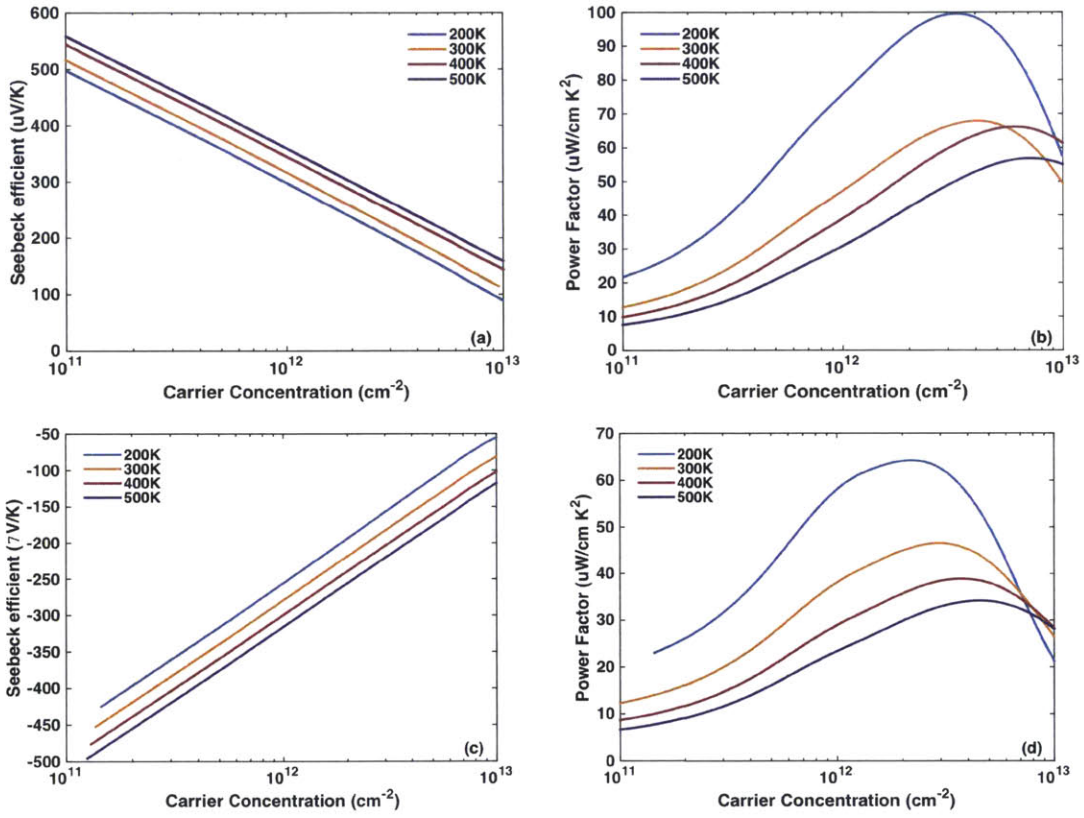

Figure 3-13 The calculated (a) Seebeck coefficient and (b) thermoelectric power factor for p-type and (c) Seebeck coefficient and (d) thermoelectric power factor for n-type monolayer phosphorene versus the carrier concentration along the armchair direction at different temperatures.

With the recently reported phonon thermal conductivity of phosphorene calculated from first-principles[188,189], we have all the ingredients for calculating the thermoelectric figure of merit zT, and the results are shown in Fig. 3-14 for p-type and n-type phosphorene along the armchair direction at temperatures up to 500K. The optimal

zT is ~0.06 at 300K and ~0.14 at 500K for p-type, with the optimal carrier concentration around 5×10^{12} cm^{-2} at 300K and 8×10^{12} cm^{-2} at 500K. These values are for impurity-free phosphorene and should be regarded as an upper limit for the thermoelectric performance of phosphorene.

A common strategy to improve the thermoelectric performance is to introduce nanoscale grain boundaries or precipitates[58,62] to strongly scatter phonons and suppress the thermal conductivity. The success of this nanostructuring approach relies on the separation of the transport length scales of electrons and phonons: in typical thermoelectric materials, the phonon mean free paths[61] are much longer than the electron mean free paths[66], so that nanostructures with characteristic sizes in between can effectively block the phonon flow while leaving the electrons intact. Therefore, whether this nanostructuring approach is effective for a certain material and what should be the proper length scale of the nanostructures depends on the detailed information of the mean free path distributions of electrons and phonons in that material.

To evaluate the potential effectiveness of the nanostructuring approach[58] for further improving zT of phosphorene, we calculate the accumulated contribution to the transport properties along the armchair direction from individual carrier states with respect to their mean free paths, as shown in Fig. 3-15, where we choose the optimal carrier concentration 5×10^{12} cm^{-2} at 300K. The calculated accumulated contribution represents fictitious values of the transport properties if carriers with mean free paths longer than a certain value are strongly suppressed by nanostructures (removed from the calculation), which is then normalized by the corresponding bulk values. In doing so, we first sort the carrier states with respect to their mean free paths, and then calculate the

transport properties using Eqs. (2.3) to (2.5), but only including in the summations carrier states with mean free paths below a certain value. For example, from Fig. 3-15(a), we can tell that holes with mean free paths below 6 nm contribute to about 40% of the total electrical conductivity and the power factor, and about 25% to the electronic thermal conductivity. Figure 3-15 indicates that the major contribution to the transport comes from carriers with mean free paths below 10 nm at 300K, or in other words, nanostructures with characteristic sizes above 10 nm do not have a strong impact on electron transport in phosphorene. Since the phonon thermal conductivity has contributions from phonons with mean free paths up to 1 μm[188,189], nanostructures with a characteristic size of ~10 nm can significantly reduce the phonon thermal conductivity (down to about 1 W/mK according to reference[189]) and preserve the electronic properties. In this ideal case, the figure of merit zT at 300K can be improved to around 1 in p-type phosphorene along the armchair direction(in reality phonons with mean free paths longer than 10nm still conduct some heat, just with shorter mean free paths). We note here that a more realistic evaluation of the effectiveness of the nanostructuring approach is to study the scattering of phonons and electrons with the grain boundaries using, for example, atomic Green's function method[94]. In practice, however, since the atomic details of the grain boundaries can vary in numerous ways, a first-principles treatment has not been practical so far. Nevertheless, the mean free path distributions provide practical guidance for experimentalists in designing nanostructrures with proper length scales to achieve improved thermoelectric performance of phosphorene.

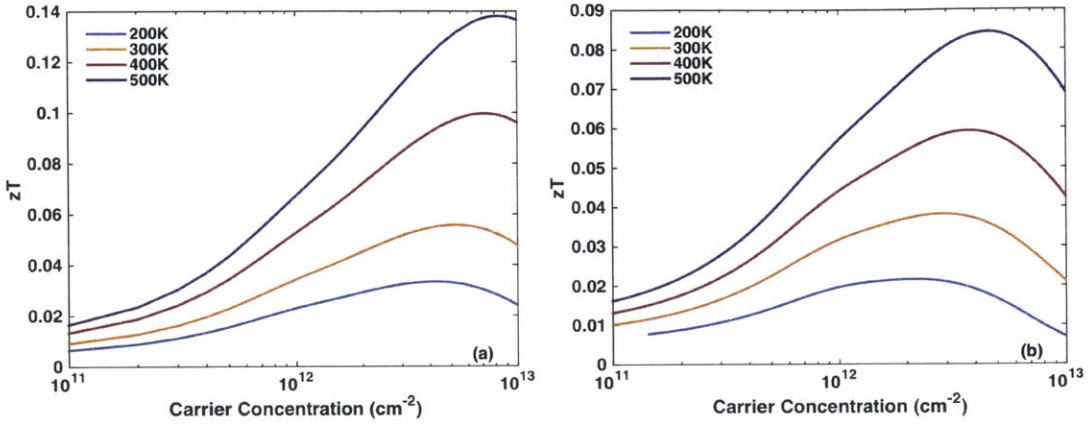

Figure 3-14 Thermoelectric figure of merit zT versus the carrier concentration for (a) p-type and (b) n-type phosphorene along the armchair direction at different temperatures, limited by the electron-phonon scattering.

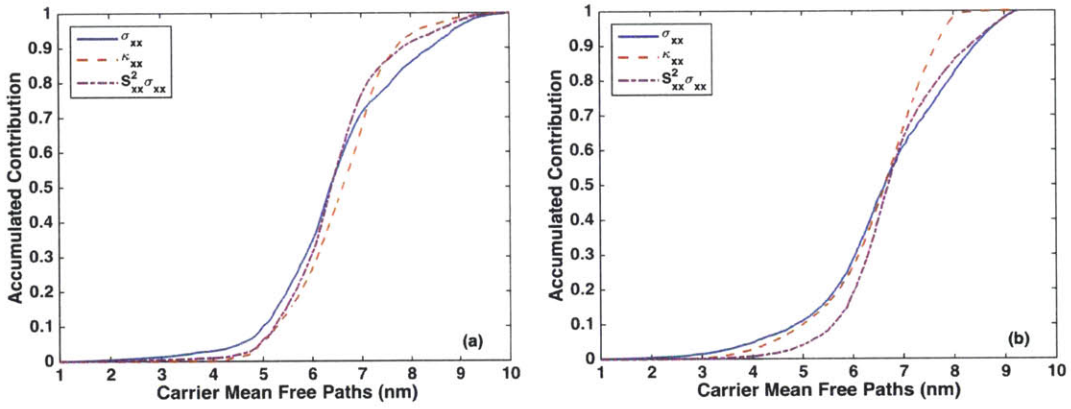

Figure 3-15 Accumulated contribution to transport properties (σ_{xx}: electrical conductivity, S_{xx}: Seebeck coefficient, κ_{xx}: electronic thermal conductivity) along the armchair direction from individual carrier states with respect to their mean free paths in (a) p-type and (b) n-type phosphorene. The carrier concentration is at 5×10^{12} cm^{-2} and the temperature is at 300K for both cases.

In summary of this section, we study the potential thermoelectric performance of phosphorene via first-principles calculation of the electron-phonon interactions. Our calculation finds that previous deformation potential calculations overestimate the carrier mobility due to the high anisotropy and the large contributions from optical phonons. We further calculate the figure of merit zT for phosphorene and the carrier mean free path

distribution, which, in comparison to the phonon mean free path distribution, indicates that nanostructuring can effectively enhance the thermoelectric performance of phosphorene.

Chapter 4

Effect of Electron-Phonon Interaction on Phonon Transport

In this chapter we study an electron-phonon interaction effect that has largely been ignored in semiconductors in previous studies, namely, how electrons act back on phonons through the electron-phonon interaction and affect the lattice thermal conductivity. We first present a study of this effect in silicon from first-principles calculations, where we show that the lattice thermal conductivity can indeed by largely reduced by electron-phonon interaction when the carrier concentration gets above 10^{19} cm^{-3}, in contrast to previous beliefs. Then we present an experimental study to verify that this effect is correct using ultrafast photoacoustic spectroscopy. In this experimental study we find that a 250-GHz acoustic pulse can be significantly suppressed by photoexcited carriers. We further quantify this effect, and find the linear dependence of

the phonon scattering rate due to the electron-phonon interaction on the carrier concentration, in agreement with the theoretical calculation.

4.1 First-principles Simulation of the Phonon Scattering due to Electrons in Silicon*

4.1.1 Background and Introduction

While the effect of the electron-phonon interaction on electron transport has been widely studied in great detail and has become standard content in textbooks[10,31,110], its effect on phonon transport has received much less attention. In our opinion the reason is twofold. First of all, the carrier concentration in semiconductors for conventional microelectronic and optoelectronic applications is typically below 10^{19} cm^{-3} [195], and as we shall show later, the impact of the electron-phonon interaction on phonon transport in this concentration range turns out to be too small to invoke any practical interest. On the other hand, in metals with a typical carrier concentration greater than 10^{22} cm^{-3}, the thermal conduction is dominated by electrons, and in most cases phonons contribute less than 10% to the total thermal conductivity[196]. Most of the existing work that were related to the effect of electron-phonon interaction on the lattice thermal conductivity looked into metals, pioneered by Sommerfeld and Bethe[197], and subsequently by Makinson[198] and Klemens[199]. The main conclusion is that the phonon thermal conductivity in metals is limited by electron-phonon interaction only at low temperatures. The classical treatment of this problem in semiconductors was provided by Ziman[110,200,201], where simplified

---

* B. Liao et al., Physical Review Letters, **114**, 115901 (2015)

models for the phonon dispersion, the electronic structure and the interaction matrix elements were used for a closed-form analytic formula with limited accuracy and applicability (only valid at low temperatures in degenerate semiconductors). Again the common wisdom was that the electron-phonon interaction would only be important on the phonon transport at low temperatures, partly due to the fact that most of the studies analyzed samples with carrier concentrations below 10^{18} cm^{-3}. A detailed discussion of the aforementioned models was given by Asheghi et al.[202].

In the past two decades, the field of thermoelectrics has been revived after the introduction of nanotechnology. Most of the best thermoelectric materials synthesized so far have been heavily-doped semiconductors, or in some cases, semiconductors with intrinsic off-stoichiometry defects, usually with carrier concentrations well above 10^{19} cm^{-3} or even 10^{20} cm^{-3} (e.g.[203] for BiSbTe, [204] for Si/Ge, [21,62] for PbTe, [30] for SnTe etc.). Moreover, a large portion of the efforts for enhancing the thermoelectric efficiency have been focused on reducing the lattice thermal conductivity via nanostructuring[56,58,62]. In this context, how the lattice thermal conductivity is affected by electron-phonon interaction with the carrier concentration in the range of 10^{19} cm^{-3} to 10^{21} cm^{-3} has become an important question yet to be answered in detail. So far only Ziman's formula was used in modeling this effect in heavily-doped thermoelectrics[205–212], and this formula is apparently insufficient for achieving an adequate modern understanding. Here we attempt to answer this question more accurately with calculations done fully from first-principles.

4.1.2 Calculation Details

The phonon scattering rate due to electron-phonon interaction can be calculated using Fermi's golden rule Eq. (2.13). This expression is related to the imaginary part of the phonon self-energy $\Pi''_{\mathbf{q}\nu}$ in treatments of the electron-phonon interaction using field theories: $\frac{1}{\tau^{ep}_{\mathbf{q}\nu}} = \frac{2\Pi''_{\mathbf{q}\nu}}{\hbar}$ [213]. Given that the phonon energy scale is much smaller than the electron energy scale, $f_{n\mathbf{k}} - f_{m\mathbf{k}+\mathbf{q}} \approx \frac{\partial f_{n\mathbf{k}}}{\partial \varepsilon_{n\mathbf{k}}} \hbar\omega_{\mathbf{q}\nu} = -f_{n\mathbf{k}}\left(1 - f_{n\mathbf{k}}\right)\frac{\hbar\omega_{\mathbf{q}\nu}}{k_B T}$, and Eq. (2.13) agrees with that used by Ziman[110]. The electron-phonon interaction matrix elements can be calculated *ab initio* within standard density functional perturbation theory (DFPT)[106]. Although the matrix elements obtained this way have been used to calculate the effect of the electron-phonon interaction on electronic transport[214–216], the phonon mesh density required for a converged electron-phonon interaction calculation can be rather demanding. Thanks to the recent development of an interpolation scheme using maximally-localized Wannier functions[116], electron-phonon interaction calculations with very fine meshes have become possible. After the electron-phonon interaction matrix elements are obtained, Eq. (2.13) can be integrated over the first Brillouin zone to generate the phonon lifetimes.

To fully evaluate the effect of the electron-phonon interaction on the lattice thermal conductivity, the intrinsic lattice thermal conductivity that is limited by the phonon-phonon scattering processes must also be calculated from first-principles and used as the baseline. Here this calculation is done with the first-principles framework based on DFT and real-space lattice dynamics, as presented in previous chapters of this thesis[60,105]. The lifetimes due to both the phonon-phonon interaction and the electron-

phonon interaction are finally combined using Mattiessen's rule[110], and the lattice thermal conductivity can be calculated as the sum of contributions from all the phonon modes $\kappa = \frac{1}{3}\sum_{q\nu} C_{q\nu} v_{q\nu}^2 \tau_{q\nu}$, where $C_{q\nu}$ is the mode-specific heat capacity, $v_{q\nu}$ is the group velocity and $\tau_{q\nu}$ is the total lifetime.

We use the Quantum Espresso package[103] for the DFT and DFPT calculations, with a norm-conserving pseudopotential with Perdew-Burke-Ernzerhof exchange-correlation functional[217]. The electron-phonon interaction matrix elements are first calculated on a $12\times12\times12$ k-mesh and a $6\times6\times6$ q-mesh, and later interpolated to finer meshes using the Electron-Phonon-Wannier (EPW) code[104]. The original code was later modified to carry out the Brillouin zone integration using the tetrahedra method[117] to improve the convergence. The convergence of the phonon lifetimes due to electron-phonon interaction with respect to the k-mesh density has been checked. Results shown later are calculated on a $60\times60\times60$ k-mesh and a $60\times60\times60$ q-mesh. The details of the phonon-phonon calculation follow those in Ref.[60]. All calculations are performed at the room temperature (300K).

4.1.3 Results and Discussion

The scattering rates of all phonon modes due to electron-phonon interaction (by either electrons or holes) at the carrier concentration of 10^{21} cm^{-3} are given in Fig. 4-1. Several general features can be observed here. First of all, phonons near the zone center, both acoustic and optical ones, are strongly scattered by both the electrons and holes in intravalley processes. Since the phonon energy scale is much smaller than that of the electrons, phonons with larger wavevectors are less likely to be scattered by electrons,

and the corresponding scattering phase space restricted by the energy and momentum selection rules is much smaller. This is reflected in the low scattering rates of phonons with intermediate wavevectors. For phonons near the zone boundary, the scattering rates due to electrons or holes are very different. In the case of scattering with electrons, the phonons near the zone boundary can efficiently participate in intervalley processes, moving electrons among the 6 equivalent pockets near the bottom of the conduction band of silicon, and the resulting scattering rates are comparable to those of the phonons near the zone center. In the case of scattering with holes, however, the intervalley processes are absent due to the sole hole-pocket, and thus the scattering rates of the phonons by holes near the zone boundary are very low.

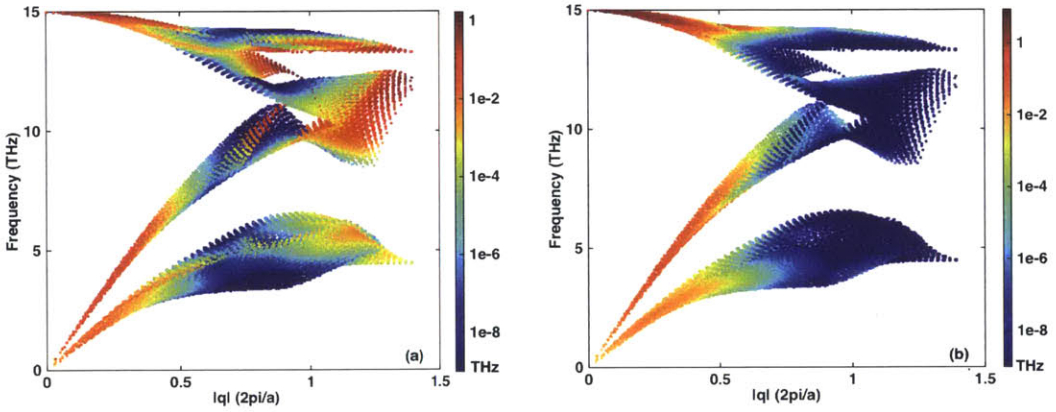

Figure 4-1 The scattering rates of phonons in silicon due to electron-phonon interaction by (a) electrons and (b) holes. The carrier concentration is 10^{21} cm^{-3}. The color denotes the scattering rates, and the white region indicates that either there is no phonon mode, or the scattering rates are below the threshold rate of the calculation.

Since it is very difficult, if not impossible, to isolate the contributions of the electron-phonon interaction to the lattice thermal conductivity experimentally, we are not able to directly verify our calculations via comparing with any previous experimental data (our calculation is indeed verified by an photoacoustic measurement for a single

phonon mode, as will be elaborated in the next section of this thesis). As a benchmark, we study the asymptotic behavior of the scattering rates of phonons near the zone center, and we compare our results with an analytic model. At the long wavelength limit, the effect of phonons on the lattice approaches a uniform strain, and thus the matrix elements $\langle m\mathbf{k}+\mathbf{q}|\partial_{\mathbf{q}\gamma}V|n\mathbf{k}\rangle$ can be replaced by a constant *deformation potential*: $D_A q$ for acoustic phonons and D_O for optical phonons[31]. The presence of q in the acoustic case is due to the fact that the deformation potential is proportional to the spatial derivative of the atomic displacement, while in the optical case, it is proportional to the atomic displacement *per se*[31]. With this deformation potential approximation (DPA), the asymptotic behavior of Eq. (2) can be derived without further approximations in the nondegenerate regime as

$$\frac{1}{\tau_{\mathbf{q}\nu}^{ep}}=\frac{\left(2\pi m^*\right)^{1/2}D_A^2}{\left(k_BT\right)^{3/2}g_d\rho v_s}\exp\left(-\frac{m^*v_s^2}{2k_BT}\right)n(E_f)\omega_{\mathbf{q}\nu} \text{ for acoustic modes and} \tag{4.1}$$

$$\frac{1}{\tau_{\mathbf{q}\nu}^{ep}}=\left(\frac{2\pi m^*}{k_BT}\right)^{1/2}\frac{D_O^2}{g_d\rho\omega_O}\sinh\left(\frac{\hbar\omega_O}{2k_BT}\right)n(E_f)\exp\left(-\frac{m^*\omega_O^2}{2k_BTq^2}\right)(\hbar q)^{-1} \text{ for optical modes,} \tag{4.2}$$

where m^* is the density-of-state effective mass of the carriers, ρ the mass density, g_d the number of equivalent carrier pockets, v_s the sound velocity, $n\left(E_f\right)$ the carrier concentration with E_f being the Fermi level, and ω_O the optical phonon frequency (~15 THz in silicon). Equations (4.1) and (4.2) supplement Ziman's formula in the nondegenerate regime at higher temperatures. In Fig. 4-2 we show the comparison between the calculated scattering rates and the analytic predictions Eqs. (4.1) and (4.2) for longitudinal acoustic (LA) and optical (LO) phonons scattered by electrons or holes

(the shear strain induced by transverse phonons is a second-order effect in the DPA formalism[31] and thus does not fit in the discussion here). A $60\times60\times60$ q-mesh is used for this calculation. As predicted by Eq. (4.1), the scattering rates of LA modes scale linearly with the phonon frequency near the zone center, and the slope in turn depends linearly on the carrier concentration. As the carrier concentration approaches the degenerate regime, the scattering rates saturate. In the case of LO modes, the scattering rates depend on the magnitude of the wavevector in a more complex manner. Due to the anisotropy of the electron pockets, the electron-phonon interaction scattering rates near the zone center are more scattered compared to holes. Good agreements between the calculated scattering rates and the DPA prediction are observed with $D_A \approx 5.2$ eV, $D_O \approx 1\times10^8$ eV/cm for electrons and $D_A \approx 4.8$ eV, $D_O \approx 1\times10^9$ eV/cm for holes, all in a reasonable range compared to literature[31] values except for D_O for electrons, of which we could not find reliable data in the literature.

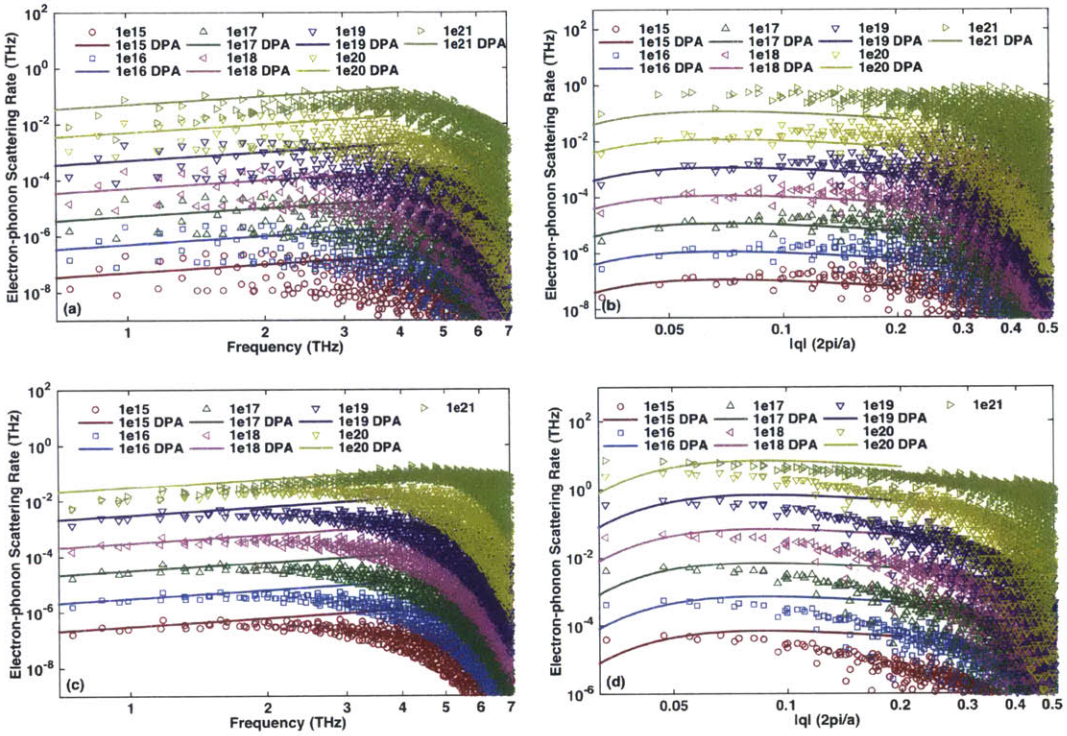

Figure 4-2 The asymptotic behaviors (lines) of the phonon scattering rates due to the electron-phonon interaction, calculated from DPA, are compared with data obtained from first-principles (dots) for (a) LA modes and (b) LO modes scattered by electrons and (c) LA modes and (d) LO modes scattered by holes. A $60\times60\times60$ q-mesh is used in this calculation.

Upon gaining confidence in our calculation, we proceed to compare the scattering rates of phonons due to electron-phonon interaction (at carrier concentrations of 10^{21} cm^{-3}) to the intrinsic phonon-phonon interactions, as shown in Fig. 4-3. The electron-phonon interaction scattering rates are at least two orders of magnitude lower than the intrinsic phonon-phonon scattering rates when the carrier concentration is below 10^{18} cm^{-3}, and above 10^{19} cm^{-3}, the electron-phonon interaction scattering rates start to be comparable to the intrinsic phonon-phonon scattering rates within the low-frequency region, and in fact can surpass the phonon-phonon scattering rates for the low-frequency phonons when the carrier concentration reaches 10^{21} cm^{-3} as shown in Fig. 4-3. This is

expected to have a major impact on the lattice thermal conductivity, since most of the heat is carried by phonons with the lowest frequencies.

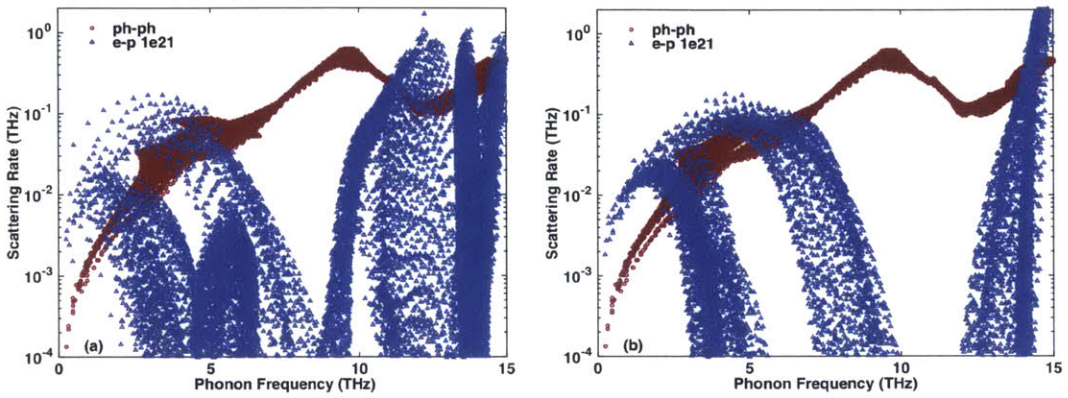

Figure 4-3 The phonon scattering rates due to electron-phonon interaction with (a) electrons and (b) holes at the carrier concentration of 10^{21} cm^{-3} and the intrinsic phonon-phonon interaction. This calculation is carried out on a $60\times60\times60$ q-mesh, mainly limited by the phonon-phonon interaction calculation.

Figure 4-4 shows the calculated lattice thermal conductivity of silicon taking into account both the electron-phonon interaction and the phonon-phonon interaction. As expected, when the carrier concentration is below 10^{18} cm^{-3}, the effect of the electron-phonon interaction on the lattice thermal conductivity is negligible, whereas the electron-phonon interaction significantly reduces the lattice thermal conductivity when the carrier concentration goes above 10^{19} cm^{-3}. In particular, holes are more efficient in scattering phonons than electrons, which is probably due to the isotropic hole pockets in contrast to the anisotropic electron pockets (this finding is consistent with experimental facts where boron-doped p-type silicon has a lower thermal conductivity than phosphorous-doped n-type silicon with similar doping concentrations at the room temperature[202,218]), and the lattice thermal conductivity can be reduced by as much as 45% when the hole concentration reaches 10^{21} cm^{-3}.

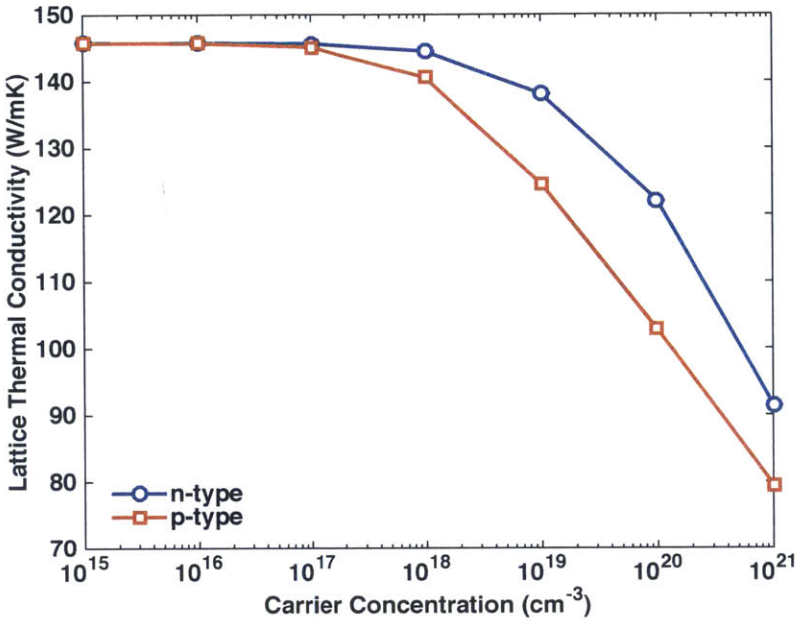

Figure 4-4 The lattice thermal conductivity versus the carrier concentration, taking into account both the electron-phonon interaction and the phonon-phonon interaction. The calculation is done on a $60\times60\times60$ q-mesh for both electron-phonon and phonon-phonon calculations.

To further analyze the effect of the electron-phonon interaction on phonon transport, we also calculate the change of the phonon mean free paths when the electron-phonon interaction is considered and the carrier concentration is at 10^{21} cm^{-3}. In Fig. 4-5 we compare the phonon mean free paths with and without the electron-phonon interaction. Electrons and holes can efficiently scatter phonons with mean free paths longer than 100 nm, which is a group of phonons that carries ~70% of the total heat in silicon at 300K[60].

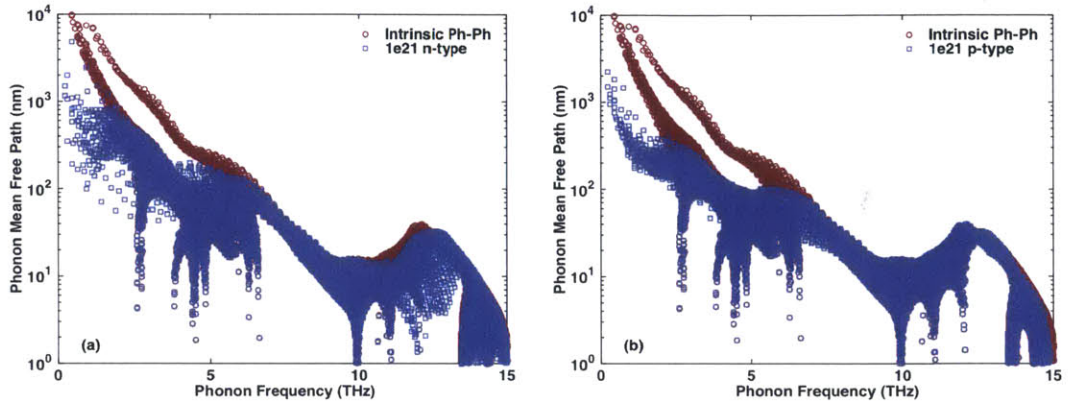

Figure 4-5 Phonon frequency dependence of the phonon mean free paths with and without electron-phonon interaction: (a) phonons scattered by electrons and (b) phonons scattered by holes. The carrier concentration is 10^{21} cm^{-3} in both cases.

In summary of this section, we carry out a first-principles calculation of the lattice thermal conductivity of silicon considering both phonon-phonon and electron-phonon interactions, and we predicted a large reduction (up to 45%) of the lattice thermal conductivity due to the electron-phonon interaction at the room temperature, an effect previously overlooked in most cases. This finding not only fills the gap of understanding of how the electron-phonon interaction affects the lattice thermal conductivity in semiconductors when the carrier concentration is in the range of 10^{19} cm^{-3} to 10^{21} cm^{-3}, but also has a profound technological impact on the field of thermoelectrics. Although higher carrier concentrations also mean higher electronic thermal conductivity, this effect is in general much smaller than the reduction of the lattice thermal conductivity in the considered range of carrier concentrations (a simple estimation using the Wiedemann-Franz law and experimental data for the electrical conductivity of heavily-doped silicon[219] yields values below 1 W/mK for carrier concentrations above 10^{20} cm^{-3} at room temperature).

4.2 Photoacousctic Spectroscopy of Phonon Damping by Photo-excited Carriers

4.2.1 Backgound and Introduction

The electron-phonon interaction is among the most important interactions of (quasi)particles in condensed matter physics. Given its paramount importance, numerous experimental techniques have been developed to probe the electron-phonon interaction in various materials directly or indirectly, with most of them examining the effect of the electron-phonon interaction on electrons. For example, the collective effect of the interactions among all phonons and electrons that participate in transport can be inferred from electrical transport experiments[110,220]. Alternatively, the average electron-phonon coupling strength can be directly measured by investigating the timescale of equilibration of electrons and phonons in ultrafast optical pump-probe experiments[221–224]. In these experiments, electrons are first heated up by absorbing a femtosecond laser pulse to a temperature much higher than the lattice (phonon) temperature, and the subsequent equilibration of the electrons and phonons is recorded through measuring the change of either the reflectance or transmission of the sample by a probe pulse. The cooling rate of the electrons is directly related to the electron-phonon coupling constant λ [225], which indicates the average strength of the interactions between electrons near the Fermi level and all phonons. Furthermore, angle-resolved photoemission spectroscopy (ARPES) can directly map out the electronic band structure near the material surface and the linewidths of the electronic states provide specific information of the interaction strength between a single electron state with all the phonon modes[226].

On the other hand, the effect of the electron-phonon interaction on phonons has been much less studied experimentally. Previous measurements on metals usually apply a high magnetic field to "freeze out" the electrons and then measure the change of the thermal conductivity[227]. Usually the change is small due to the small energy scale of typical magnetic fields, and most measurements were thus far done at cryogenic temperatures with large uncertainties. An alternative way to probe the phonon-specific information of the electron-phonon interaction in metals would be through superconducting tunneling spectroscopy (STS)[228]. From STS the Éliashberg function[225] $\alpha^2F(\omega)$ can be extracted, which reflects the interaction strength of electrons near the Fermi surface with phonons having a specific frequency ω. However it is limited to superconductors and cannot resolve individual phonon modes. Early experiments on semiconductors mostly focused on the effect of carriers introduced by doping on the thermal conductivity[229–241]. One difficulty of these experiments is to separate the contributions to the phonon scattering from the carriers themselves and from the impurities introduced by doping. The same difficulty stands in inelastic neutron scattering (INS) measurements of the phonon linewidths for doped semiconductors[242].

The recent advancement of thermoelectrics has revived the research interest of the effect of the electron-phonon interaction on phonons, since most thermoelectric materials are heavily doped semiconductors with carrier concentrations in the range of 10^{19} to 10^{21} cm^{-3}, and it was shown in the previous section[243] that the lattice thermal conductivity of silicon can be reduced by 45% due to the electron-phonon interaction at a carrier concentration of 10^{21} cm^{-3}, through first-principles simulation. Although this effect is significant in the simulation, it is challenging to verify in experiment due, again, to the

difficulty of separating the contributions from carriers and impurities if the carriers are introduced by doping. Despite the difficulty, experimental evidence of this effect is highly desirable, not only to corroborate the theory and the simulation in the previous section[243], but also to demonstrate the necessity of including this effect in the design, analysis and engineering of thermoelectric materials in the future.

In the next subsection we describe an experimental technique developed to directly measure the phonon scattering by free carriers, in this case excited by ultrafast laser pulses. Since the carriers are introduced optically without atomic impurities, the effect of the electron-phonon interaction should be easily isolated.

4.2.2 Design and Calibration of Experimental Setup

The new experimental technique is built upon ultrafast photoacoustic spectroscopy[244–246]. In conventional ultrafast photoacoustic spectroscopy, an acoustic strain pulse is launched in a thin sample first by an ultrafast optical pump pulse. This optical pump pulse is absorbed by electronic transitions, and the deformation potential of the excited electrons causes strain in the sample, and an acoustic strain pulse is then released by the relaxation of the carriers with the emission of phonons. Then this acoustic strain pulse travels back and forth inside the thin sample and is recorded by an ultrafast optical probe pulse. The optical response in the probe pulse is generated either through the strain of the material[244], or through the Brillouin oscillation[246], which aroses from the interference of light reflected from the sample surface and from the strain pulse. In the former case, usually a broadband signal is detected with peak frequencies corresponding to the thickness resonances of the thin sample, while in the latter case, a narrow band signal can be obtained with a peak frequency (Brillouin frequency f_B) determined by the

longitudinal speed of sound v_L, the refractive index n of the sample and the probe wavelength λ according to

$$f_B = \frac{2nv_L}{\lambda}. \tag{4.3}$$

In silicon with a 400nm probe pulse, the Brillouin frequency is ~250 GHz. Figure 4-6 shows the Brillouin oscillation superposed with the acoustic pulses recorded in a 370nm-thick silicon membrane. By comparing the amplitudes of the frequency components of the pulses, the damping of the phonon pulse due to losses during the propagation inside the membrane, can be quantified. In the conventional pump-probe setup, the phonon damping is caused by phonon-phonon interaction in the bulk of the sample and to surface losses[244,246].

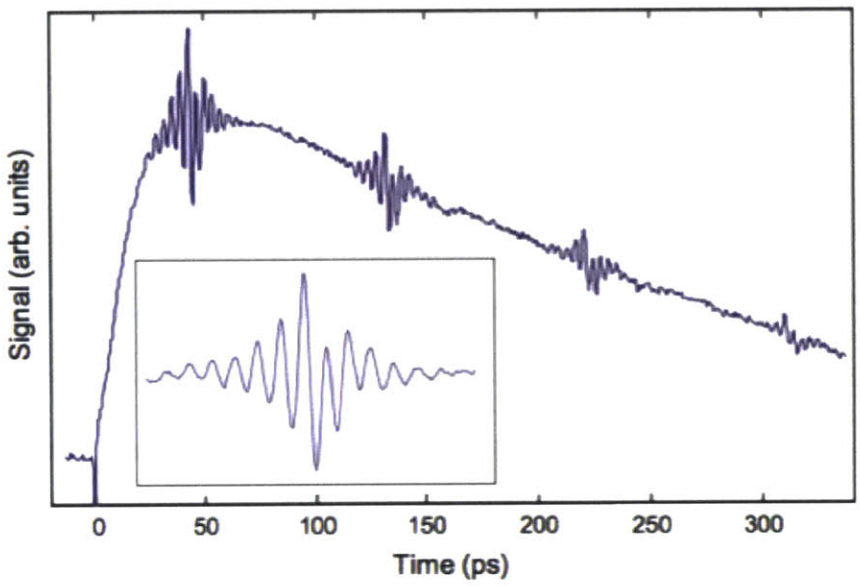

Figure 4-6 Typical acoustic pulses and Brillouin oscillations observed in an ultrafast photoacoustic measurement. In this case the measurement was done in a 370nm-thick silicon membrane. Acoustic pulses convoluted with the Brillouin oscillation were observed. The background signal resulted from the carrier generation and diffusion. Adapted from Ref. 246.

In order to measure the phonon damping caused by free charge carriers, we introduce another optical pulse to generate carriers inside the sample. We choose to use 800nm optical pulses for this purpose and a 1.7 μm -thickness silicon material as the sample. At 800nm, the optical penetration depth of silicon is ~8 μm , so that approximately the carriers are generated uniformly within the membrane. For pump and probe pulses, we choose 400nm wavelength, at which the penetration depth is only ~50nm. The experimental setup is illustrated in Fig. 4-7. This experimental setup is in Prof. Keith Nelson's laboratory in the Department of Chemistry of MIT.

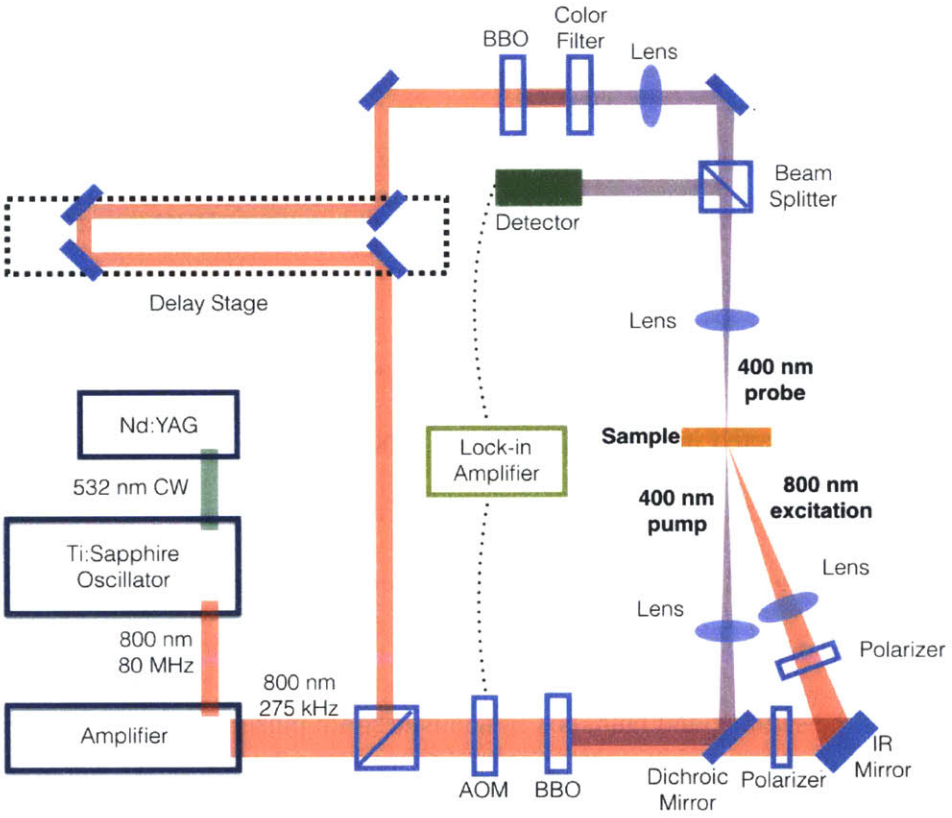

Figure 4-7 Schematic of the experimental setup. Unlabeled components are regular mirrors.

The output laser beam from the amplifier is at 800 nm with a repetition rate of 275 kHz. It is then separated by a polarizing beam splitter into a pump beam and a probe

beam. The pump beam is subsequently modulated by an acousto-optic modulator (AOM) at a modulation frequency of 95 kHz. After going through a frequency-double crystal (bismuth borate, BBO), the generated second harmonic (400 nm) beam is separated from the remaining 800nm beam by a dichroic mirror. The two beams are then focused onto the sample plane with lenses. The extra path the 800 nm beam takes than the 400 nm beam is ~6 cm long, corresponding to a delay of ~260 ps. The choice of this delay time will be explained later. Two thin film polarizers are placed in the path of the 800nm beam to continuously control its power without deflecting the beam. The diameters of both beams at the sample plane (also the focal planes of the corresponding lenses) are measured with a razor blade to be ~60 μm. On the other hand, the probe beam goes through a delay stage, which gives a maximum delay of ~5 ns compared to the 400 nm pump beam. Then the probe beam is frequency-doubled via a BBO crystal, and the residual 800 nm beam is filtered out by a color filter. The 400 nm probe is then focused onto the sample plane with a lens (beam diameter ~20 μm). The reflected probe beam from the sample is directed into a photodiode via a beam splitter, which is then read out by a lock-in amplifier at the modulation frequency of the AOM (95 kHz).

Since we use a pulsed laser to generate carriers, the timing of the three pulses is crucial. We design the pulse sequence as follows: at t=0 ps, the 400 nm pump pulse hits the front side of the sample, and launches an acoustic strain pulse. It takes ~210 ps for the strain pulse to traverse the 1.7 μm -thick membrane and be recorded by the 400 nm probe beam on the back side of the sample. After that, this acoustic strain pulse is reflected from the sample surface and starts the second round trip inside the membrane. In our design, the 800 nm pulse arrives at t=260 ps, right after the first acoustic pulse is

recorded. The 800 nm pulse generates free electron-hole pairs uniformly inside the membrane. Since silicon is an indirect-gap semiconductor, the recombination time is relatively long. And thus, the generated electron-hole pairs remain in the membrane for up to a few ns, and will damp the acoustic strain pulse during its second round trip. At t=620 ps, the second echo is recorded by the probe beam when the strain pulse reaches the back side of the membrane again. The decay of the phonon mode at the Brillouin frequency 250 GHz can now be quantified by comparing the frequency components at 250 GHz of the spectra of the first and second echoes. Furthermore, the contribution to the phonon damping from the photo-excited carriers can be isolated from the phonon-phonon scattering and boundary loss by comparing the total damping rate with and without the 800 nm excitation beam. One important advantage of this design is that only the ratio, not the absolute amplitudes, of the two echoes matters, so that the fluctuations on larger time scales, such as due to laser power, and ambient temperature, will not affect the measurement.

There are several technical considerations. Firstly, the amount of laser power needed for sufficient carrier concentration needs to be estimated. At 275 kHz repetition rate, 10 mW of measured laser power translates to a single pulse energy of 73 nJ (a factor of two takes into account the square-wave modulation of the AOM). The absorptance of the membrane at 800 nm is measured to be 25% to 30% depending on the location. Given the phonon energy of 1.55 eV at 800 nm, and the beam diameter of 60 μm , the generated concentration of electron-hole pairs can be estimated to be 1.8×10^{19} cm^{-3}. At this carrier concentration, we expect from Eq. (4.1) that the 250 GHz phonon lifetime due to electron-phonon interaction is a few hundred of picoseconds, on the same order of the

intrinsic phonon life time ~250 ps, and thus, the extra damping of the phonon mode due to carriers should be able to be observed. Secondly, the heating caused by the 800 nm beam needs to be minimized. Given the single pulse energy of 73 nJ, and the volumetric specific heat of silicon $\sim 1.6\times10^{6}$ J/K-m^3, the instantaneous temperature rise due to absorption of a single 800 nm pulse can be estimated to be ~3 K. This is significantly smaller than the Debye temperature of silicon (645 K) and thus has negligible effect on phonon damping. The limited heat dissipation capability, however, of the silicon membrane also leads to an accumulated steady-state temperature rise. We estimate this temperature rise in a COMSOL simulation to be ~15 K at the maximum power (~15 mW) that we use in the experiment. This temperature rise is still not expected to have an observable effect on phonon damping, also verified by the experimental fact that the amplitude of the first echo is not affected by the presence of the 800 nm excitation. Thirdly, the 400 nm pump pulse also generates carriers. Although their contributions to the phonon damping is subtracted out when we compare the total damping with and without the 800 nm excitation, we do not want the carriers generated by the 400 nm pump to dominate those generated by the 800 nm excitation. The typical power of the 400 nm pump beam we use in the experiment is 13 mW, ~60% of which is measured to be reflected by the membrane. Since the photon energy at 400 nm is twice that at 800 nm, the number of photons in a 400 nm beam is smaller than that of an 800 nm beam given the same power. Due to the shallow absorption length (~50 nm) at 400 nm, an extremely high ($\sim 5\times10^{20}$ cm^{-3}) carrier concentration is initially generated within the thin 50-nm layer. At this carrier concentration, Auger recombination takes over and the recombination time is below 100 ps[195]. Therefore, the carrier concentration will drop

significantly before the acoustic pulse reaches the back-side of the membrane for the first time, and further reduced by the diffusion of the carriers. With an average carrier diffusivity of 24 cm^2/s in silicon, the carriers will diffuse out to a layer of ~700 nm in 200 ps, and combined with a recombination time of 100 ps, the carrier concentration is estimated to drop below 1×10^{18} cm^{-3}, much lower than that generated by the 800 nm excitation. To test this conclusion, we measured the intrinsic 250 GHz phonon lifetime with different 400 nm pump power from 6 mW to 15 mW at a same location on the membrane, and we did not see any systematic reduction of the intrinsic phonon lifetime with increasing pump power at 400 nm, as shown in Table 4-1. The large uncertainty at the lower pump power is due to the reduced signal amplitude and thus to the associated signal-noise ratio.

Table 4-1 The measured intrinsic phonon lifetime with different power of the 400 nm pump pulses, at the same location on the membrane.

400 nm Pump Power (mW)	6	9	12	15
Intrinsic Lifetime (ps)	238.3±57.9	224.9±26.1	234.3±23.5	248.2±3.5

To calibrate the alignment of the three beams, we first measured the response of a 40-nm gold film, and fine-tuned the alignment of the three beams to maximize the signal. The result is shown in Fig. 4-8. Two peaks are observed at 0 ps and 260 ps, respectively, corresponding to arrival of the 400 nm and 800 nm pump pulses. The 800 nm signal is of much lower intensity, because gold is 97% reflective at 800 nm and 40% reflective at 400 nm.

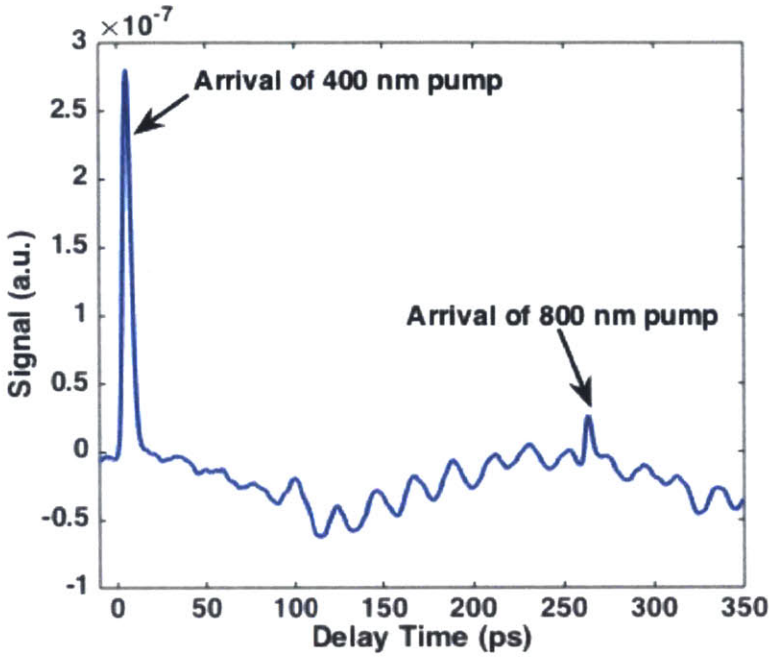

Figure 4-8 Response of a 40-nm gold film. The two peaks at 0 ps and at 260 ps signal arrivals of the 400 nm and 800 nm pump pulses, respectively.

The next calibration step is to measure the response of the silicon membrane with only the 800 nm excitation beam and the 400 nm probe beam. This is to verify the carrier generation as we expected, as well as make sure that the response of the 800 nm excitation does not spectrally interfere with the 250 GHz Brillouin oscillations. The results are shown in Fig. 4-9. The responses are caused by the instantaneous carrier generation. As shown in Fig. 4-9, higher power corresponds to a larger change in the reflectance signal at 260 ps, indicating higher carrier concentration. The decay of the signal with time indicates the carrier recombination process. The recombination process is faster for higher carrier concentration, as expected, but the lifetime is still sufficiently long to ensure that the carrier concentration does not drop significantly within the measurement window (indicated by the dashed lines, 260 ps to 620 ps). The wiggles on the decay curves are the lowest-order thickness resonances of the membrane at 2.5 GHz,

corresponding to the ~400 ps acoustic round-trip time, which is far separated from the 250 GHz Brillouin oscillation. The decay curves drop below the baseline for higher excitation power due to the reflectance change of silicon caused by the slight temperature rise.

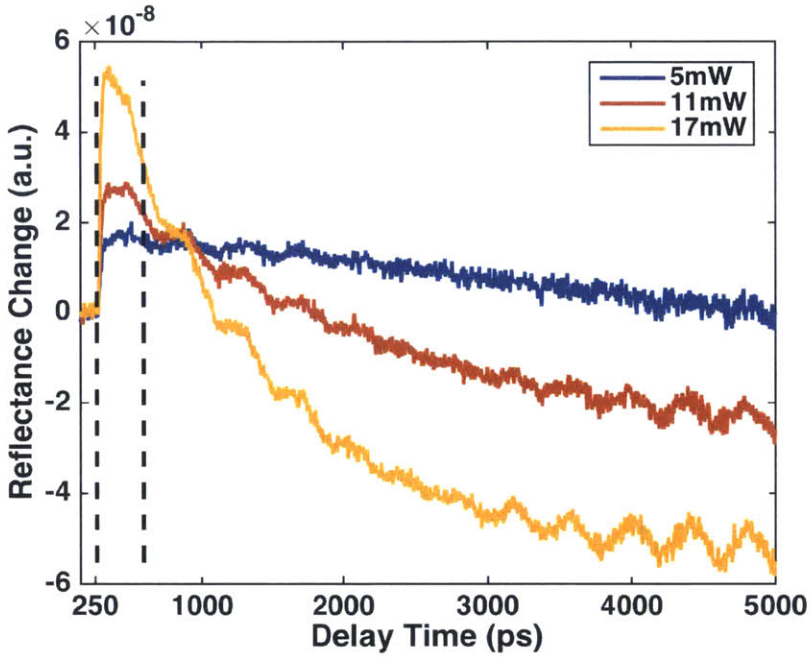

Figure 4-9 The response of a 1.7-μm silicon membrane with only the 800 nm excitation beam and the 400 nm probe beam. The 800 nm excitation power is varied from 5 mW to 17 mW. The responses are caused by carrier generation, with different carrier concentrations and lifetimes at different excitation powers.

4.2.3 Results and Discussion

In Fig. 4-10 we show the profiles of the second acoustic echo, given different powers of the 800 nm excitation beam. It is clearly seen that the fast Brillouin oscillation is incrementally suppressed by the 800 nm excitation pulse, giving a clear evidence of phonon damping by the photo-excited electron-hole pairs.

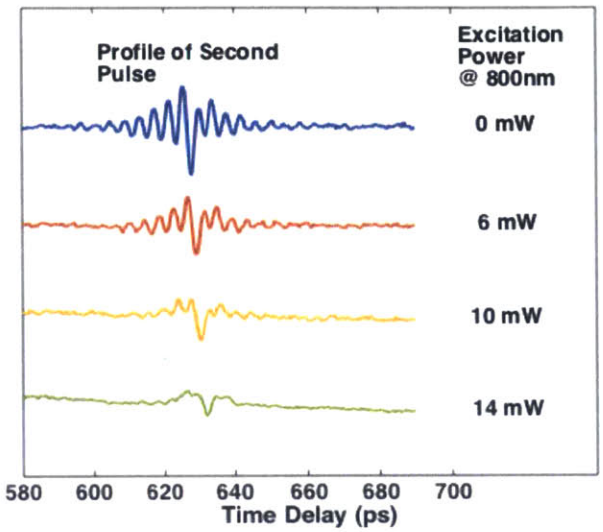

Figure 4-10 The recorded profiles of the second acoustic echo, given different powers of the 800 nm excitation beam.

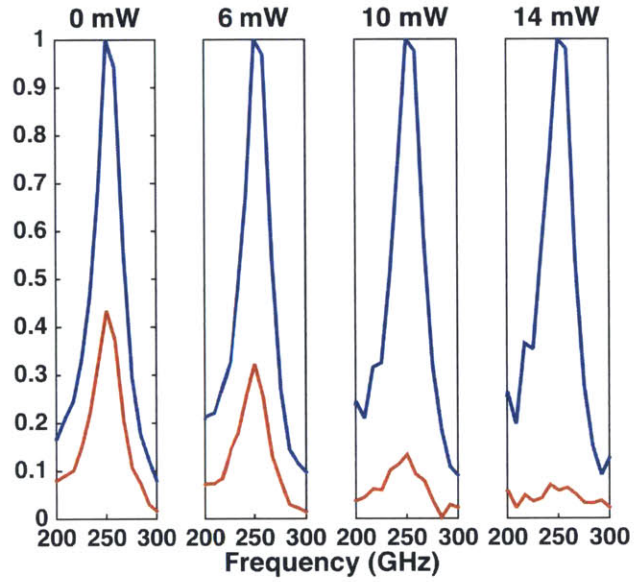

Figure 4-11 Comparing the Fourier spectra of the first and second echoes with different powers of the 800 nm excitation beam. The blue lines are the spectra of the first echoes, and the orange lines are the spectra of the second echoes.

To quantify the phonon lifetime due to electron-phonon interaction, Fourier transforms of the first and second echoes are carried out and are compared quantitatively, as shown in Fig. 4-11. As expected, the amplitude of the frequency component at 250

GHz of the second echo is clearly suppressed by the 800 nm excitation beam, even down to the noise level when the 14 mW of 800 nm excitation beam is used. Measurements beyond this power is thus not possible.

To calculate the 250 GHz phonon scattering rate (reciprocal of the lifetime) due to the electron-phonon interaction, we use Matthiessen's rule to separate the contributions from electron-phonon interaction, phonon-phonon interaction and boundary loss. The scattering rate due to the electron-phonon interaction γ_{ep} can be calculated as

$$\gamma_{ep} = \left[2\ln\left(\frac{A_1}{A_2}\right) - \frac{\Delta t_1}{\tau_i} \right] \Big/ \Delta t_2 - \frac{1}{\tau_i}, \tag{4.4}$$

where A_1 and A_2 are the amplitudes of the first and second echoes, $\Delta t_1 = 50$ ps is the delay time after the first echo but before the 800 nm pulse arrives, $\Delta t_2 = 360$ ps is the rest of the round-trip time, $\tau_i \approx 250$ ps is the intrinsic phonon lifetime measured when the 800-nm excitation beam is turned off, including contributions from the phonon-phonon interaction and boundary loss. To eliminate the error caused by laser fluctuations, we did reference measurements without the 800 nm excitation before and after each measurement with the 800 nm excitation, and we made sure the intrinsic lifetime does not change appreciably in the two reference measurements.

The 250 GHz phonon scattering rate due to the electron-phonon interaction calculated from Eq. (4.4) is plotted in Fig. 4-12, along with the theoretical prediction of Eq. (4.1) without any fitting parameters. The reported data were measured on three different locations of the membrane, and each data point represented an average of 10 to 30 measurements, depending on the signal-noise ratio required. The error bars are the standard deviations of the measurement results that are averaged. Given the

approximations made in data processing, and the possible errors in estimating the carrier concentrations, the agreement between experiment and theory is reasonable. Not only is the linear trend observed as predicted, but also the numerical values are in reasonable agreement.

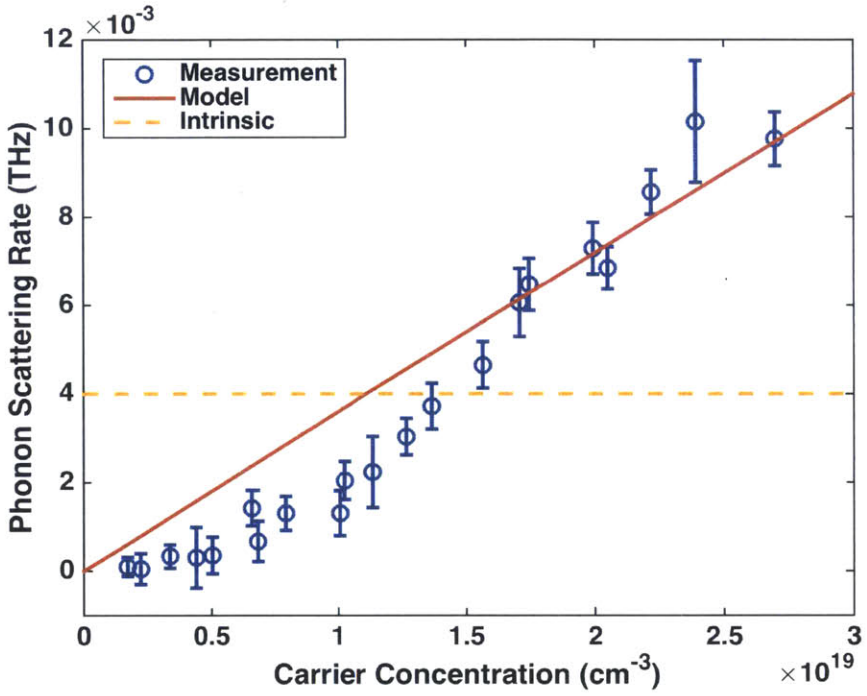

Figure 4-12 The measured 250 GHz phonon scattering rate due to the electron-phonon interaction, compared to the theoretical prediction of Eq. (4.1). The yellow dashed line labels the intrinsic phonon scattering rate due to phonon-phonon interaction and boundary loss.

We emphasize here that the estimation of the carrier concentration given the power of 800 nm excitation is rough, due to uncertainties in measuring the beam sizes, absorptance, and the slight change of carrier concentration during the measurement window, as shown in Fig. 4-9. In particular, the measured scattering rate is lower than the theoretical prediction for lower carrier concentrations.

In summary of this section, we developed an experimental technique based on ultrafast photoacoustic spectroscopy to directly measure the damping of a single phonon

mode by free charge carriers for the first time. The measured results agree well with theoretical prediction quantitatively. We envision this method can be used to characterize electron-phonon interaction for a wide range of relevant materials, such as thermoelectrics and superconductors.

Chapter 5

Magnon Thermal Transport and Magnon Cooling Effect*

In this chapter we explore a Boltzmann transport theory of magnons in ferromagnetic insulators. Since magnons can be driven either by temperature gradient or by magnetic field gradient, a coupled transport theory analogous to that of electrons can be established. Considering the interaction between phonons and magnons, we also propose a novel magnon cooling effect that can potentially realize wireless cooling applications.

5.1 Background

Electron, phonons and magnons are the major energy carriers studied in this thesis. Coupled to these carriers are thermodynamic forces that drive their flows[247]: the gradients of temperature, electrochemical potential and non-equilibrium magnetization[248].

---

* B. Liao et al., Physical Review Letters, **113**, 025902 (2014)

For conditions close to equilibrium, it is particularly convenient to treat the coupled transport phenomena within the phenomenological framework of irreversible thermodynamics[247], where the Onsager reciprocity relation serves as the link between concurrent flows. Routinely used in studying the coupled transport of electrons and phonons[10,247,248], the method of irreversible thermodynamics has also been utilized in analyzing the coupled transport of heat and charge with spins[248–252] .

In this thesis we limit our discussion to ferromagnetic insulators without free conducting electrons. Further steps to understanding the spin caloritronic effects require microscopic models that provide quantitative information of the transport processes, for example the kinetic coefficients[247] that connect the driving forces to the corresponding fluxes. For studying thermoelectrics, the coupled transport processes are typically treated within the framework of Boltzmann transport equation (BTE)[10], which in the diffusion regime gives quantitative kinetic coefficients, and is capable of delineating ballistic transport[56] when solved with proper boundary conditions. It is particularly a natural way to describe thermally induced transport processes where coherent contributions are not important. On the other hand, the spintronics community often uses the Landau-Lifshitz-Gilbert (LLG)[253] equation for the dynamics of magnetization. Compared with BTE, LLG adopts more a "wave-like" point of view, where the coherent dynamics is important and the thermal relaxation acts as a damping factor. Indeed the long wavelength magnons have been shown to exhibit macroscopic coherence lengths at room temperature[254], and LLG is necessary to account for their behaviors. For the thermal transport, however, magnons with a wide range of wavelengths and coherent lengths will be excited, and LLG seems no longer a particularly convenient description. A recent work by Hoffman *et*

al.[255] applied a "semi-phenomenological" stochastic LLG equation to modeling the longitudinal SSE, where the temperature effect was incorporated via a thermally fluctuating Langevin field. Since a linear phonon temperature distribution was presumed in their work, it did not fully solve the coupled phonon-magnon transport problem. An alternative approach to this problem adopts a more "particle-like" picture. The pioneering work by Sanders and Walton[256] treated the coupled phonon-magnon thermal diffusion process with a two-temperature model, where phonons and magnons were modeled as two gases of bosons, each locally in thermal equilibrium with different temperatures, and the local energy exchange rate between them is proportional to the temperature difference. This model was later used to explain the spin Seebeck effect[79], and was recently extended to take into account the boundary heat and spin transfer[257]. It also served as a modeling tool for interpreting dynamic measurements of the thermal conductivity of spin ladder compounds[87,258] and the static direct measurement of the magnon temperature[259], and has been applied to other carrier systems such as electron-phonon[260] and acoustic-phonon-optical-phonon[261].

In their original formulation, Sanders and Walton did not consider the associated magnetization flow with the magnon heat flow. On the other hand, Meier and Loss[262] showed that the magnon flow could also be generated by a non-uniform external magnetic field, but they did not look into the thermal aspect of this transport process. More studies also discussed the similarity between field-driven magnon transport and electron transport[263–267]. In a recent work by Kosevich and Gann[268], both quantum and semiclassical dynamics of a field-driven magnon flow was thoroughly studied. We then attempt to combine the two paths, one from the thermal perspective and the other from

the magnetic perspective, and to then give a unified description of the coupled phonon-magnon diffusive transport of both heat and magnetization, which is also applicable when the external magnetic field is non-uniform, with a special focus on the thermal effect associated with the field-driven magnon flow.

5.2 Formulation of Coupled Phonon-Magnon Diffusion

Magnons are (in most cases[87]) bosonic excitations, and in equilibrium they obey the Bose-Einstein distribution:

$$f_0(\mathbf{r},\mathbf{k}) = \frac{1}{\exp\left[\dfrac{\hbar\omega(\mathbf{k}) + g\mu_B B(\mathbf{r})}{k_B T_m(\mathbf{r})}\right] - 1}, \tag{5.1}$$

where $\hbar\omega(\mathbf{k})$ is the magnon energy[83,253] without external magnetic field, g is the Landé g-factor, μ_B is the Bohr magneton ($-g\mu_B$ combined represents the amount of magnetic moment carried by a single magnon[262]), T_m is the magnon temperature and B is the external magnetic field. Here we neglect the magnetic dipolar interaction and magnetic anisotropy for simplicity. Although magnons can reach a quasi-equilibrium state with a finite chemical potential under parametric pumping[120], here we treat magnons with vanishing chemical potential for local equilibrium is here assumed. Next we write down the steady-state Boltzmann transport equation within the relaxation time approximation (RTA):

$$-\frac{f - f_0}{\tau_m} = \mathbf{v} \cdot \nabla_{\mathbf{r}} f_0, \tag{5.2}$$

where $f(\mathbf{r},\mathbf{k})$ is the non-equilibrium distribution function of magnons, $\mathbf{v}(\mathbf{k})$ is the group velocity of magnons, $\tau_m = \left(\frac{1}{\tau_{m-m}} + \frac{1}{\tau_{m-p,ela}} + \frac{1}{\tau_{m-imp}} \right)^{-1}$ is a lumped relaxation time of magnons including effects of magnon-magnon scattering[269], elastic magnon-phonon scattering[270] and elastic magnon-impurity scattering[271]. The inelastic magnon-phonon scattering is responsible for the local energy exchange between magnons and phonons[270], and in general cannot be written in a relaxation-time form[10]. Thus we follow Sanders and Walton[256] here and consider the energy exchange process separately in the conservation laws later. We emphasize that the validity of this separation requires that the phonon-magnon interactions be much weaker than the magnon-magnon interactions.

After obtaining the non-equilibrium distribution function $f(\mathbf{r},\mathbf{k})$, we can calculate the local magnetization and heat flows carried by magnons. The magnetization flow is $\mathbf{J}_m = -g\mu_B \int \frac{d^3\mathbf{k}}{(2\pi)^3} f\mathbf{v}$, where the minus sign accounts for the fact that the excitation of magnons reduces the total magnetization[119]: $\mathbf{M}(\mathbf{r}) = \mathbf{M}_s - g\mu_B n_m$, where $\mathbf{M}_s$ is the saturation magnetization, and n_m is the number density of magnons. To calculate the magnon heat flow, we start with the thermodynamic relation of a magnet[247]: $dE = dQ + BdM = dQ - Bg\mu_B dn_m$, where E is the total energy of the magnet *and* the interaction energy (BM) between the magnet and the magnetic field, and thus is field-independent[272], corresponding to $\hbar\omega(\mathbf{k})$ microscopically (in contrast $\hbar\omega(\mathbf{k}) + g\mu_B B$ corresponds to the field-dependent "spectroscopic energy"[272]). Differentiating the above relation with respect to time, we get the magnon heat flux

$\mathbf{J}_{qm} = \mathbf{J}_e - B\mathbf{J}_m = \int \frac{d^3\mathbf{k}}{(2\pi)^3}(\hbar\omega + g\mu_B B) f\mathbf{v}$, where $\mathbf{J}_{qm}$ is the magnon heat flux, $\mathbf{J}_e$ is the magnon energy flux. The term $B\mathbf{J}_m$ describes the transport of the magnetic interaction energy associated with the magnetization flow, analogous to $\varphi\mathbf{J}_c$ in the case of electrons, where φ is the electro-static potential and $\mathbf{J}_c$ is the electrical charge flux. Combining the above expression with Eqs. (5.1) and (5.2), we arrive at the constitutive equations for the magnon transport:

$$-\mathbf{J}_m = L_{11}\nabla B + L_{12}(-\nabla T_m), \tag{5.3}$$

$$\mathbf{J}_{qm} = L_{12}T_m\nabla B + L_{22}(-\nabla T_m), \tag{5.4}$$

with the kinetic coefficients given by (assuming an isotropic magnon dispersion):

$$L_{11} = -\frac{(g\mu_B)^2}{3}\int_\omega \tau_m v^2 \frac{\partial f_0}{\partial(\hbar\omega)} D(\omega)d\omega, \tag{5.5}$$

$$L_{12} = -\frac{g\mu_B}{3T_m}\int_\omega (\hbar\omega + g\mu_B B)\tau_m v^2 \frac{\partial f_0}{\partial(\hbar\omega)} D(\omega)d\omega, \tag{5.6}$$

$$L_{22} = -\frac{1}{3T_m}\int_\omega (\hbar\omega + g\mu_B B)^2 \tau_m v^2 \frac{\partial f_0}{\partial(\hbar\omega)} D(\omega)d\omega, \tag{5.7}$$

where $D(\omega)$ is the magnon density of states. We can interpret L_{11} as the isothermal magneto-conductivity σ_m and L_{22} as the uniform-field magnon thermal conductivity κ_m, and define L_{12} as a magneto-thermal coupling coefficient ς_m. Note that the Onsager reciprocity relation manifests itself explicitly in Eqs. (5.3) and (5.4). It can be shown using the Cauchy-Schwartz inequality that $L_{11}L_{22} \geq T_m L_{12}^2$ (in the case of electron

transport, this inequality implies a positive zero-current thermal conductivity[10]), which guarantees the net entropy generation in this system is non-negative. Eqs. (5.3)-(5.7) are reminiscent of electron transport, and the external field B seems to play a similar role as the electrochemical potential of electrons. We need to point out here, however, that a critical difference between electrons and magnons. The number of electrons is conserved, thus the electrochemical potential includes the contribution of a finite chemical potential that can be "self-adjusted" during the transport process, whereas the number of magnons is not conserved, and the B field does not contain a similar contribution as the chemical potential of electrons (given that the magnetic dipolar interaction is negligible).

With the constitutive equations (5.3) and (5.4), we still need conservation laws to complete the formulation. We first look at the phonon system. At a steady state, the phonon energy can either be transported by the phonon heat flux or transferred to the magnon system. Thus in the spirit of Sanders and Walton's original work, the phonon energy conservation states:

$$\nabla \cdot \mathrm{J}_{qp} = \frac{C_m C_p}{C_m + C_p} \frac{T_m - T_p}{\tau_{mp}} \equiv g_{mp}\left(T_m - T_p\right), \tag{5.8}$$

where $\mathbf{J}_{qp}$ is the phonon heat flux, T_p is the phonon temperature, C_m and C_p are the volumetric specific heat of magnons and phonons, τ_{mp} is a phenomenological time scale characterizing the inelastic interaction between phonons and magnons, and we define g_{mp} as a lumped coefficient of phonon-magnon energy exchange. It is worth mentioning that Eq. (5.8) is the result of inelastic phonon-magnon scattering and in principle can be derived from a full version of BTE, similar as in the case of electron-phonon coupling[10]. Another conservation law has to do with the energy input from an external power source.

When the magnetization of the magnet changes, an electromotive force (EMF) is induced in the electromagnet (e.g., a solenoid). To maintain the magnetic field, the current running through the electromagnet has to overcome this EMF and thus to do work. It can be shown[272] that the work done by the current in this process is precisely equal to BdM. Hence the local creation and annihilation of magnons enables the energy exchange between the system (including the ferromagnet itself and its interaction with the magnetic field) and the external power supply. A local version of the above statement can be translated to $\nabla\cdot\left(\mathbf{J}_{qm}+B\mathbf{J}_m+\mathbf{J}_{qp}\right)=B\nabla\cdot\mathbf{J}_m$, or more explicitly:

$$\nabla\cdot\mathbf{J}_{qm}+\nabla B\cdot\mathbf{J}_m=g_{mp}\left(T_p-T_m\right). \tag{5.9}$$

Now combining Eqs. (5.8), (5.9) with (5.3) and (5.4), and the normal Fourier law for phonon heat conduction: $\mathbf{J}_{qp}=-\kappa_p\nabla T_p$ (κ_p is the phonon thermal conductivity), the governing equations for the temperature distributions of magnons and phonons read (considering 1-dimentional situations):

$$-\kappa_p\frac{\partial^2 T_p}{\partial x^2}=g_{mp}\left(T_m-T_p\right), \tag{5.10}$$

$$-\kappa_m\frac{\partial^2 T_m}{\partial x^2}+\left(2\varsigma_m\frac{\partial B}{\partial x}\right)\frac{\partial T_m}{\partial x}+\varsigma_m\frac{\partial^2 B}{\partial x^2}T_m-\sigma_m\left(\frac{\partial B}{\partial x}\right)^2=g_{mp}\left(T_p-T_m\right). \tag{5.11}$$

Here we assume the applied temperature and magnetic field gradients are small and thus the transport coefficients are averaged values that do not explicitly depend on T_m or B. Eqs. (5.10) and (5.11) reduce to the original Sanders-Walton model when the external magnetic field is uniform, even though in this case the magnetization flow is present ($\mathbf{J}_m=-\varsigma_m\nabla T_m$).

5.3 Magnon Cooling Effect

More interesting phenomena emerge when a non-uniform external magnetic field is applied. We expect a non-uniform external field will drive magnon flow, which is associated with a magnon heat flow, and cause temperature redistribution of both magnons and phonons due to the phonon-magnon coupling. Without a concise analytic solution with the coupling terms, we turn to numerical solutions for clarity, before which we first estimate the kinetic coefficients based on information in the literature on yttrium iron garnet (YIG). Since the magnetic energy scale is pretty small ($g\mu_B \approx 1.3$ K/T, for $g = 2$ in YIG), we expect the predicted effect to be more pronounced at low temperatures. Thus we use the low temperature expansion of the magnon dispersion $\hbar\omega(\mathbf{k}) = Dk^2a^2$, where $D \approx 1.8$ meV [273], and the lattice constant $a = 12.3$ Å for YIG [274]. For a similar reason, we neglect the field dependence of the kinetic coefficients in the following discussion. Further assuming a constant relaxation time τ_m, we obtain the ratio $\frac{\sigma_m}{\varsigma_m} = \frac{g\mu_B}{k_B}\frac{\xi(1.5)}{\xi(2.5)} = 1.304$ K/T with $\xi(t) = \int_0^{+\infty} \frac{x^t e^x}{(e^x - 1)^2} dx$, which is analogous to the inverse of the Seebeck coefficient in the electron case. The value of τ_m is highly controversial[79], and here we adopt a value of $\tau_m \sim 1$ ns, which leads to the calculated uniform-field magnon thermal conductivity $\kappa_m \approx 8$ W/mK at 20K with zero field that is at least of the reasonable order of magnitude compared with the experiment[275]. With the same relaxation time, we obtain $\sigma_m \approx 0.25$ W/mT^2, and $\varsigma_m \approx 0.19$ W/mTK. For phonons, we choose $\kappa_p \approx 50$ W/mK [275]. At 20K, the specific heat of magnons and phonons are on the same order of magnitude (~10^4 J/m^{3}K)[276]. Different claims on the

value of τ_{mp} exists, ranging from below a few nanoseconds[257,277] to longer than a few hundred nanoseconds[79,278–280] at 300K. At lower temperature, this relaxation time will be longer, and we tentatively choose $\tau_{mp} \approx 100$ ns due to the large uncertainty of available data.

Given the above parameters, we study numerically an experimentally realizable case: a strip of YIG (100 um long) connected to a thermal reservoir at 20K with one end, and the other end isolated. If part of the YIG strip is covered by a magnetic shielding material with high magnetic permeability, a step-like magnetic field can be realized within YIG just by applying a uniform field. We model this step-like magnetic field as a smeared-out Fermi-Dirac function as shown in Fig. 5-1(a) (the length scale of the smearing is chosen to be much larger than the mean free paths of magnons to avoid the complication of ballistic transport, which in principle can still be fully captured by the BTE), and we calculate the phonon temperature at the isolated end. In this case we apply adiabatic boundary conditions for magnons at both ends ($\mathbf{J}_e = \mathbf{J}_{qm} + B\mathbf{J}_m = 0$). A phonon-temperature-drop of ~56 mK is predicted under a step field varying from 0.5T to 1.5T, with the temperature distribution of both phonons and magnons shown in Fig. 5-1(b). This temperature drop can be further amplified by increasing the field gradient as illustrated in Fig. 5-1(c). We would like to emphasize that the estimation here is very rough due to the lack of information, and is only intended to demonstrate a probable order of magnitude of this effect. The calculation above indicates that this magnon cooling effect may be detected under currently available experimental resolution. In passing we note that the predicted effect differs from the conventional magnetocaloric effect[281], such as adiabatic demagnetization, in that the magnetocaloric effect utilizes

thermodynamic properties of the magnet (i.e. the field-dependent specific heat) in equilibrium, and a uniform field is often applied.

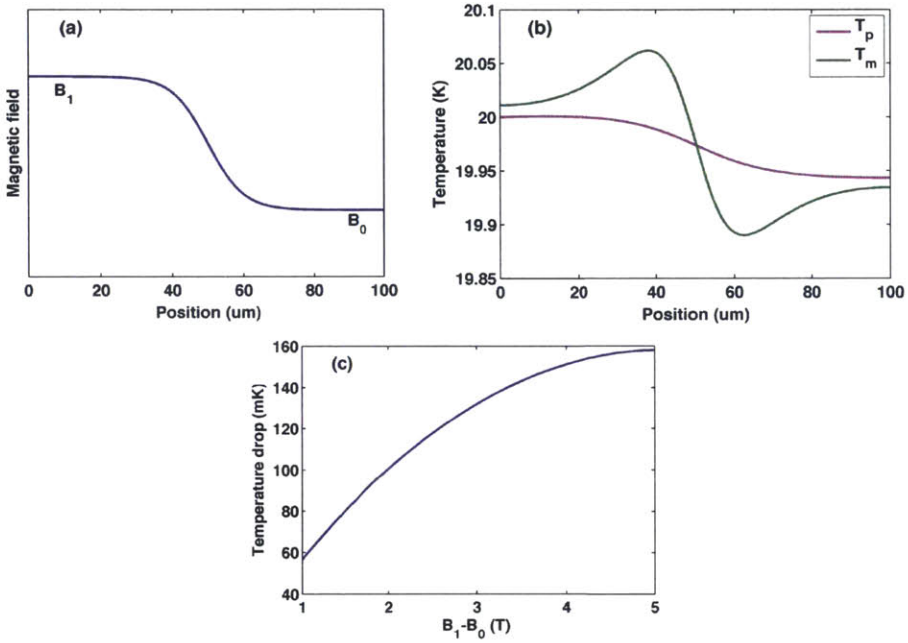

Figure 5-1 (a) The step-like magnetic field, smeared out as a Fermi-Dirac function. B_0 is fixed to be 0.5T in the following calculation. (b) The temperature distribution of phonons and magnons when $B_1 = 1.5$ T. One end of the sample ($x = 0$) is thermally connected to a reservoir at 20K, and the other end is isolated. (c) The dependence of the phonon temperature difference between the two ends on the difference of the magnetic field when B_0 is set to 0.5T.

We provide another example where the magnon cooling effect is set up in close analogy to a thermoelectric Peltier cooling unit and we calculate the coefficient of performance (COP) and effective zT. In this example the YIG strip is sandwiched between two thermal reservoirs with temperatures $T_h > T_c$, when a step field (as in Fig. 5-1(a)) is applied. The temperature profiles when $T_h = 20$ K , $T_h - T_c = 30$ mK and $(B_0, B_1) = (0.5\text{ T}, 1.5\text{ T})$ are plotted in Fig. 5-2(a), and it is clearly shown that heat is moved from the cold source to the hot source. The COP can be calculated via

$\mathrm{COP} \equiv \frac{Q_c}{W} = \frac{\mathbf{J}_{qp,cold}}{-\int_0^L B\nabla \cdot \mathbf{J}_m \, dx}$, and is plotted in Figs. 5-2(b) and 5-2(c) against varying temperature and field difference. At the fixed temperature difference of 30 mK (Fig. 5-2(b)), the optimal COP is around 2, corresponding to an equivalent thermoelectric module with ZT=0.01. From Fig. 5-2(c), the maximal attainable temperature difference is ~60 mK when $(B_0, B_1) = (0.5\ \mathrm{T}, 1.5\ \mathrm{T})$, where the COP drops to zero.

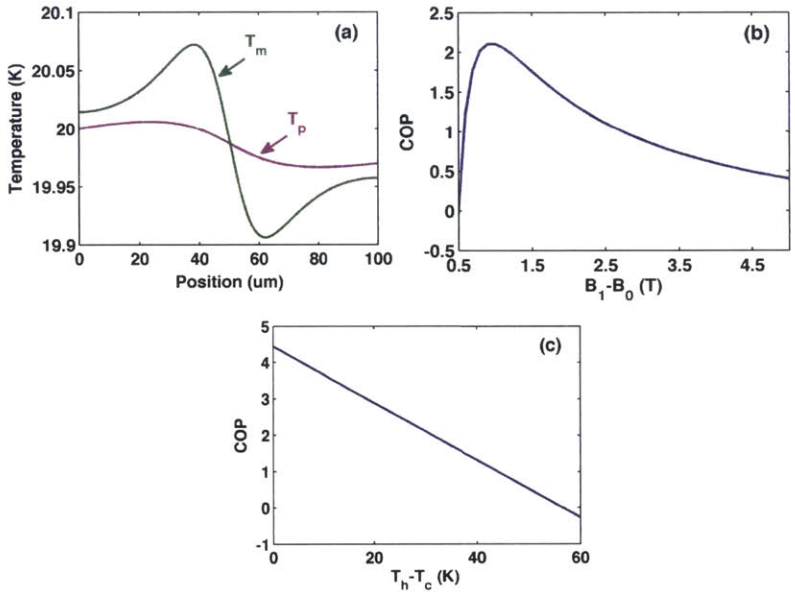

Figure 5-2 (a) The temperature profiles of phonons and magnons when $T_h = 20$ K, $T_h - T_c = 30$ mK and $(B_0, B_1) = (0.5\ \mathrm{T}, 1.5\ \mathrm{T})$. (b) COP versus the change of magnetic field when the temperature difference is fixed at 30mK. The hot-side temperature is fixed at 20K. (c) COP versus the temperature difference when the hot-side temperature is fixed at 20K and the magnetic field is fixed at $(B_0, B_1) = (0.5\ \mathrm{T}, 1.5\ \mathrm{T})$.

In summary of this chapter, we have developed a semi-classical transport theory for coupled phonon-magnon diffusion. The merit of this work lies in the fact that we apply the techniques widely used in the field of thermoelectrics to the study of magnetization transport, utilize the analogy between field-driven electron and magnon transport, and combine the thermal effect with the field-driven magnon transport in a

natural way. Our theory takes into account that magnon flow can be driven by a non-uniform magnetic field, and predicts that the heat carried by magnons associated with their flow can result in a cooling effect. In real materials, non-ideal effects such as magnetic dipolar interactions and the magnetic anisotropy need to be considered as a refinement to this work. We have estimated the magnitude of the magnon cooling effect in YIG, to show it is large enough so that it can be verified by experiments. For practical uses, however, it is necessary to search for more suitable materials (preferably with lower thermal conductivities, and strong phonon-magnon interaction), and thereby to optimize the material properties via engineering efforts. We envision this new effect could supplement the conventional magnetocaloric effect in cryogenic applications in the future.

Chapter 6

Summary and Future Work

6.1 Summary of Thesis

Transport and interaction of microscopic energy carriers in solid-state materials is an old subject, in the sense that it has been one of the cornerstones of modern condensed matter physics, and grandmasters such as L. Landau, N. Mott, P. Anderson, J. Ziman etc., all contributed to laying its foundations. The recent advancement of nanofabrication technology, modern spectroscopic techniques and first-principles simulation tools, however, has revived this old subject and brought in new possibilities and opportunities. With these new tools, transport and scattering processes are no longer abstract concepts, but rather can be intuitively understood in simulations, and directly observed in experiments, even at the single-mode level. These unprecedented understandings then in turn serve as guiding principles in materials innovation. This process is now gradually becoming a standard cycle in many branches of material science research.

This thesis contributes, specifically, to understanding the microscopic processes of transport and interactions occuring in thermoelectric materials. In light of the recent remarkable progress of phonon simulation and spectroscopic tools, and relatively lagged-behind understanding of electron transport, the central goal of this thesis has been to develop simulation and experimental tools to study electron transport, in particular electron-phonon interaction, at the single-mode level. There are two main products of this thesis. Firstly, a computer program has been co-developed by the author, which takes the output of a DFT engine and the Wannier interpolation program EPW[104], calculates the mode-by-mode scattering rates of both electrons and phonons due to electron-phonon interactions, in three-dimensional or two-dimensional materials, and outputs the thermoelectric transport properties. In Chapter 3, this program is applied to investigate intrinsic electrical transport properties limited by electron-phonon interactions in a newly discovered two-dimensional semiconductor phosphorene, and to evaluate its potential as a thermoelectric material. The power of this tool is not only that it predicts all thermoelectric properties from scratch, but also that it provided mode-by-mode information that enables nanoscale engineering efforts. In Chapter 4, this program is applied to study the effect of the electron-phonon interaction on phonon transport in silicon. This is a previously overlooked problem, and our study now reveals that it is an important effect in studying thermoelectric materials. Secondly, an experimental technique has been developed and tested, which extends the conventional ultrafast photoacoustic spectroscopy to be able to measure the damping of a single phonon mode due to free charge carriers. In Chapter 4, this technique is described in detail, and applied to study a silicon membrane. This experimental technique fills the gap of directly

detecting phonon damping by free carriers without introducing dopant impurities, and opens up an avenue towards single-mode level spectroscopy of the electron-phonon interaction.

As an exploratory project, this thesis also looks into magnon thermal transport. Spin caloritronics is a field still in its infancy. One of the main challenges in such a new interdisciplinary subject is the different languages and perspectives that people with different background knowledge use and understand. The main contribution of our work, elaborated in Chapter 5, is to combine the fields of thermoelectrics and spintronics, and to introduce the Boltzmann transport theory as a unifying language in dealing with the transport of magnons. The theoretical framework we developed puts magnons on the same stage with electrons and phonons, and thus contributes to understanding magnon transport from analogies.

We would like to emphasize that the contributions of this thesis are not limited to applications in thermoelectric materials. Many energy conversion technologies face the same challenge and opportunity of understanding the microscopic carrier transport and interaction. One example is photovoltaics, where another group of players, namely photons, also join the field, while control of the electron-phonon interaction is also a major challenge. We believe the fundamental understandings obtained in this thesis will benefit a wide range of energy conversion technologies and material researches.

6.2 Future Directions

Whereas the aim of this thesis is to investigate the microscopic interaction processes with as high a spatial and temporal resolution as possible, I have also realized that most of the existing modeling and experimental tools fall short of capturing, in

realistic energy materials, the microscopic transport and interaction processes, mostly with lengthscale of nanometers (e.g., electron and phonon mean free paths) and with timescale of femtoseconds (e.g., the electron-phonon scattering time): First-principles simulation tools are currently only suitable for simple single crystalline materials; ultrafast optical spectroscopy is limited in its spatial resolution by the diffraction limit, while standard electron microscopes cannot resolve dynamics with sub-nanosecond duration. How to really reach down to the nanometer and femtosecond spatial-temporal resolution to study the fundamental building blocks of energy transport and conversion processes in realistic energy materials? This is the question I intend to answer through research in the future.

I will continue along this path as a postdoctoral scholar in Prof. Ahmed Zewail's laboratory in California Institute of Technology, where ultrafast electron microscopic techniques are being developed. With optical pulses as pumps and electron pulses as probes, these new tools can break the optical diffraction limit while maintaining the femtosecond temporal resolution. Combining ultrafast electron microscopy with the recent development of time-dependent DFT (TDDFT) simulation tools, I believe my future research will lead me down to the extreme spatial and temporal scales, where transport and interaction of individual electrons and phonons can be visualized and understood, and hopefully these understandings will eventually contribute to innovative material design and engineering in the future.

References

1. Chu, S. & Majumdar, A. Opportunities and challenges for a sustainable energy future. *Nature* **488,** 294–303 (2012).
2. Goldsmid, H. J. *Introduction to thermoelectricity.* (Springer, 2010).
3. Bell, L. E. Cooling, Heating, Generating Power, and Recovering Waste Heat with Thermoelectric Systems. *Science* **321,** 1457–1461 (2008).
4. Heremans, J. P., Dresselhaus, M. S., Bell, L. E. & Morelli, D. T. When thermoelectrics reached the nanoscale. *Nat. Nanotechnol.* **8,** 471–473 (2013).
5. Ioffe, A. F. *Physics of Semiconductors.* (Academic Press, 1960).
6. Ashcroft, N. W. & Mermin, N. D. *Solid State Physics.* (Harcourt, 1976).
7. Heremans, J. P., Dresselhaus, M. S., Bell, L. E. & Morelli, D. T. When thermoelectrics reached the nanoscale. *Nat. Nanotechnol.* **8,** 471–473 (2013).
8. Liao, B. & Chen, G. Nanocomposites for thermoelectrics and thermal engineering. *MRS Bull.* **40,** 746–752 (2015).
9. Zhao, L.-D., Dravid, V. P. & Kanatzidis, M. G. The panoscopic approach to high performance thermoelectrics. *Energy Environ. Sci.* **7,** 251–268 (2013).
10. Chen, G. *Nanoscale Energy Transport and Conversion: a Parallel Treatment of Electrons, Molecules, Phonons, and Photons.* (Oxford University Press, 2005).
11. Hicks, L. D. & Dresselhaus, M. S. Effect of quantum-well structures on the thermoelectric figure of merit. *Phys. Rev. B* **47,** 12727–12731 (1993).
12. Hicks, L. D. & Dresselhaus, M. S. Thermoelectric figure of merit of a one-dimensional conductor. *Phys. Rev. B* **47,** 16631–16634 (1993).
13. Mahan, G. D. & Sofo, J. O. The best thermoelectric. *Proc. Natl. Acad. Sci.* **93,** 7436–7439 (1996).
14. Harman, T. C., Taylor, P. J., Walsh, M. P. & LaForge, B. E. Quantum Dot Superlattice Thermoelectric Materials and Devices. *Science* **297,** 2229–2232 (2002).
15. Hicks, L. D., Harman, T. C., Sun, X. & Dresselhaus, M. S. Experimental study of the effect of quantum-well structures on the thermoelectric figure of merit. *Phys. Rev. B* **53,** R10493–R10496 (1996).
16. Venkatasubramanian, R., Siivola, E., Colpitts, T. & O'Quinn, B. Thin-film thermoelectric devices with high room-temperature figures of merit. *Nature* **413,** 597–602 (2001).
17. Chowdhury, I. *et al.* On-chip cooling by superlattice-based thin-film thermoelectrics. *Nat. Nanotechnol.* **4,** 235–238 (2009).
18. Boukai, A. I. *et al.* Silicon nanowires as efficient thermoelectric materials. *Nature* **451,** 168–171 (2008).
19. Ohta, H. *et al.* Giant thermoelectric Seebeck coefficient of a two-dimensional electron gas in SrTiO3. *Nat. Mater.* **6,** 129–134 (2007).

20. Koga, T., Sun, X., Cronin, S. B. & Dresselhaus, M. S. Carrier pocket engineering to design superior thermoelectric materials using GaAs/AlAs superlattices. *Appl. Phys. Lett.* **73,** 2950–2952 (1998).
21. Pei, Y. *et al.* Convergence of electronic bands for high performance bulk thermoelectrics. *Nature* **473,** 66–69 (2011).
22. Pei, Y. *et al.* Stabilizing the Optimal Carrier Concentration for High Thermoelectric Efficiency. *Adv. Mater.* **23,** 5674–5678 (2011).
23. Liu, W. *et al.* Convergence of Conduction Bands as a Means of Enhancing Thermoelectric Performance of n-Type $Mg_2Si_{1-x}Sn_x$ Solid Solutions. *Phys. Rev. Lett.* **108,** 166601 (2012).
24. Zhao, L. D. *et al.* All-scale hierarchical thermoelectrics: MgTe in PbTe facilitates valence band convergence and suppresses bipolar thermal transport for high performance. *Energy Environ. Sci.* **6,** 3346–3355 (2013).
25. Wang, H., Gibbs, Z. M., Takagiwa, Y. & Snyder, G. J. Tuning bands of PbSe for better thermoelectric efficiency. *Energy Environ. Sci.* **7,** 804–811 (2014).
26. Banik, A., Shenoy, U. S., Anand, S., Waghmare, U. V. & Biswas, K. Mg Alloying in SnTe Facilitates Valence Band Convergence and Optimizes Thermoelectric Properties. *Chem. Mater.* **27,** 581–587 (2015).
27. Tang, Y. *et al.* Convergence of multi-valley bands as the electronic origin of high thermoelectric performance in CoSb3 skutterudites. *Nat. Mater.* **14,** 1223–1228 (2015).
28. Heremans, J. P., Wiendlocha, B. & Chamoire, A. M. Resonant levels in bulk thermoelectric semiconductors. *Energy Environ. Sci.* **5,** 5510–5530 (2012).
29. Heremans, J. P. *et al.* Enhancement of Thermoelectric Efficiency in PbTe by Distortion of the Electronic Density of States. *Science* **321,** 554–557 (2008).
30. Zhang, Q. *et al.* High thermoelectric performance by resonant dopant indium in nanostructured SnTe. *Proc. Natl. Acad. Sci.* **110,** 13261–13266 (2013).
31. Lundstrom, M. *Fundamentals of Carrier Transport.* (Cambridge University Press, 2009).
32. Bohren, C. F. & Huffman, D. R. *Absorption and Scattering of Light by Small Particles.* (Wiley-VCH, 1998).
33. Schiff, L. I. *Quantum Mechanics.* (McGraw-Hill College, 1968).
34. Zebarjadi, M. *et al.* Effect of nanoparticle scattering on thermoelectric power factor. *Appl. Phys. Lett.* **94,** 202105 (2009).
35. Bahk, J.-H. *et al.* Thermoelectric power factor enhancement by ionized nanoparticle scattering. *Appl. Phys. Lett.* **99,** 072118 (2011).
36. Bahk, J.-H., Santhanam, P., Bian, Z., Ram, R. & Shakouri, A. Resonant carrier scattering by core-shell nanoparticles for thermoelectric power factor enhancement. *Appl. Phys. Lett.* **100,** 012102 (2012).
37. Bahk, J.-H., Bian, Z. & Shakouri, A. Electron energy filtering by a nonplanar potential to enhance the thermoelectric power factor in bulk materials. *Phys. Rev. B* **87,** 075204 (2013).
38. Mahan, G. D. Thermionic refrigeration. *J. Appl. Phys.* **76,** 4362–4366 (1994).
39. Shakouri, A. & Bowers, J. E. Heterostructure integrated thermionic coolers. *Appl. Phys. Lett.* **71,** 1234–1236 (1997).

40. Puneet, P. *et al.* Preferential Scattering by Interfacial Charged Defects for Enhanced Thermoelectric Performance in Few-layered n-type Bi_2Te_3. *Sci. Rep.* **3,** 3212 (2013).
41. Zebarjadi, M. *et al.* Power Factor Enhancement by Modulation Doping in Bulk Nanocomposites. *Nano Lett.* **11,** 2225–2230 (2011).
42. Yu, B. *et al.* Enhancement of Thermoelectric Properties by Modulation-Doping in Silicon Germanium Alloy Nanocomposites. *Nano Lett.* **12,** 2077–2082 (2012).
43. Liao, B., Zebarjadi, M., Esfarjani, K. & Chen, G. Cloaking Core-Shell Nanoparticles from Conducting Electrons in Solids. *Phys. Rev. Lett.* **109,** 126806 (2012).
44. Zebarjadi, M., Liao, B., Esfarjani, K., Dresselhaus, M. & Chen, G. Enhancing the Thermoelectric Power Factor by Using Invisible Dopants. *Adv. Mater.* **25,** 1577–1582 (2013).
45. Rowe, D., Ed., *CRC Handbook of Thermoelectrics.* (CRC-Press, 1995).
46. Sales, B. C., Mandrus, D. & Williams, R. K. Filled Skutterudite Antimonides: A New Class of Thermoelectric Materials. *Science* **272,** 1325–1328 (1996).
47. Zhao, W. *et al.* Enhanced Thermoelectric Performance in Barium and Indium Double-Filled Skutterudite Bulk Materials via Orbital Hybridization Induced by Indium Filler. *J. Am. Chem. Soc.* **131,** 3713–3720 (2009).
48. Shi, X. *et al.* Multiple-Filled Skutterudites: High Thermoelectric Figure of Merit through Separately Optimizing Electrical and Thermal Transports. *J. Am. Chem. Soc.* **133,** 7837–7846 (2011).
49. Dahal, T., Jie, Q., Lan, Y., Guo, C. & Ren, Z. Thermoelectric performance of Ni compensated cerium and neodymium double filled p-type skutterudites. *Phys. Chem. Chem. Phys.* **16,** 18170–18175 (2014).
50. Zhao, W. *et al.* Multi-localization transport behaviour in bulk thermoelectric materials. *Nat. Commun.* **6,** 7197 (2015).
51. Chen, G., Tien, C. L., Wu, X. & Smith, J. S. Thermal Diffusivity Measurement of GaAs/AlGaAs Thin-Film Structures. *J. Heat Transf.* **116,** 325–331 (1994).
52. Lee, S.-M., Cahill, D. G. & Venkatasubramanian, R. Thermal conductivity of Si–Ge superlattices. *Appl. Phys. Lett.* **70,** 2957–2959 (1997).
53. Borca-Tasciuc, T. *et al.* Thermal conductivity of symmetrically strained Si/Ge superlattices. *Superlattices Microstruct.* **28,** 199–206 (2000).
54. Capinski, W. S. *et al.* Thermal-conductivity measurements of GaAs/AlAs superlattices using a picosecond optical pump-and-probe technique. *Phys. Rev. B* **59,** 8105–8113 (1999).
55. Chen, G. Size and Interface Effects on Thermal Conductivity of Superlattices and Periodic Thin-Film Structures. *J. Heat Transf.* **119,** 220–229 (1997).
56. Chen, G. Thermal conductivity and ballistic-phonon transport in the cross-plane direction of superlattices. *Phys. Rev. B* **57,** 14958–14973 (1998).
57. Garg, J. & Chen, G. Minimum thermal conductivity in superlattices: A first-principles formalism. *Phys. Rev. B* **87,** 140302 (2013).
58. Poudel, B. *et al.* High-Thermoelectric Performance of Nanostructured Bismuth Antimony Telluride Bulk Alloys. *Science* **320,** 634–638 (2008).

59. Broido, D. A., Malorny, M., Birner, G., Mingo, N. & Stewart, D. A. Intrinsic lattice thermal conductivity of semiconductors from first principles. *Appl. Phys. Lett.* **91,** 231922 (2007).
60. Esfarjani, K., Chen, G. & Stokes, H. T. Heat transport in silicon from first-principles calculations. *Phys. Rev. B* **84,** 085204 (2011).
61. Tian, Z., Lee, S. & Chen, G. Heat Transfer in Thermoelectric Materials and Devices. *J. Heat Transf.* **135,** 061605–061605 (2013).
62. Biswas, K. *et al.* High-performance bulk thermoelectrics with all-scale hierarchical architectures. *Nature* **489,** 414–418 (2012).
63. Minnich, A. J. *et al.* Thermal Conductivity Spectroscopy Technique to Measure Phonon Mean Free Paths. *Phys. Rev. Lett.* **107,** 095901 (2011).
64. Johnson, J. A. *et al.* Direct Measurement of Room-Temperature Nondiffusive Thermal Transport Over Micron Distances in a Silicon Membrane. *Phys. Rev. Lett.* **110,** 025901 (2013).
65. Hu, Y., Zeng, L., Minnich, A. J., Dresselhaus, M. S. & Chen, G. Spectral mapping of thermal conductivity through nanoscale ballistic transport. *Nat. Nanotechnol.* **10,** 701–706 (2015).
66. Qiu, B. *et al.* First-principles simulation of electron mean-free-path spectra and thermoelectric properties in silicon. *Europhys. Lett.* **109,** 57006 (2015).
67. Bauer, G. E. W., Saitoh, E. & van Wees, B. J. Spin caloritronics. *Nat. Mater.* **11,** 391–399 (2012).
68. Boona, S. R., Myers, R. C. & Heremans, J. P. Spin caloritronics. *Energy Environ. Sci.* **7,** 885–910 (2014).
69. Jeon, K.-R. *et al.* Thermal spin injection and accumulation in CoFe/MgO/n-type Ge contacts. *Sci. Rep.* **2,** 962 (2012).
70. Hatami, M., Bauer, G. E. W., Zhang, Q. & Kelly, P. J. Thermal Spin-Transfer Torque in Magnetoelectronic Devices. *Phys. Rev. Lett.* **99,** 066603 (2007).
71. Jiang, W. *et al.* Direct Imaging of Thermally Driven Domain Wall Motion in Magnetic Insulators. *Phys. Rev. Lett.* **110,** 177202 (2013).
72. Uchida, K. *et al.* Observation of the spin Seebeck effect. *Nature* **455,** 778–781 (2008).
73. Jaworski, C. M. *et al.* Observation of the spin-Seebeck effect in a ferromagnetic semiconductor. *Nat. Mater.* **9,** 898–903 (2010).
74. Uchida, K. *et al.* Spin Seebeck insulator. *Nat. Mater.* **9,** 894–897 (2010).
75. Uchida, K. *et al.* Long-range spin Seebeck effect and acoustic spin pumping. *Nat. Mater.* **10,** 737–741 (2011).
76. Jaworski, C. M., Myers, R. C., Johnston-Halperin, E. & Heremans, J. P. Giant spin Seebeck effect in a non-magnetic material. *Nature* **487,** 210–213 (2012).
77. Flipse, J., Bakker, F. L., Slachter, A., Dejene, F. K. & Wees, B. J. van. Direct observation of the spin-dependent Peltier effect. *Nat. Nanotechnol.* **7,** 166–168 (2012).
78. Flipse, J. *et al.* Observation of the spin Peltier effect. *arXiv:1311.4772 Cond-Mat* (2013).
79. Xiao, J., Bauer, G. E. W., Uchida, K., Saitoh, E. & Maekawa, S. Theory of magnon-driven spin Seebeck effect. *Phys. Rev. B* **81,** 214418 (2010).
80. Adachi, H., Ohe, J., Takahashi, S. & Maekawa, S. Linear-response theory of spin Seebeck effect in ferromagnetic insulators. *Phys. Rev. B* **83,** 094410 (2011).

81. Adachi, H., Uchida, K., Saitoh, E. & Maekawa, S. Theory of the spin Seebeck effect. *Rep. Prog. Phys.* **76,** 036501 (2013).
82. Tikhonov, K. S., Sinova, J. & Finkel'stein, A. M. Spectral non-uniform temperature and non-local heat transfer in the spin Seebeck effect. *Nat. Commun.* **4,** (2013).
83. Kittel, C. & Fong, C. Y. *Quantum theory of solids.* (Wiley, 1987).
84. Wang, B., Wang, J., Wang, J. & Xing, D. Y. Spin current carried by magnons. *Phys. Rev. B* **69,** 174403 (2004).
85. Hess, C. Heat conduction in low-dimensional quantum magnets. *Eur. Phys. J. Spec. Top.* **151,** 73–83 (2007).
86. Uchida, K. *et al.* Longitudinal spin Seebeck effect: from fundamentals to applications. *J. Phys. Condens. Matter* **26,** 343202 (2014).
87. Hohensee, G. T., Wilson, R. B., Feser, J. P. & Cahill, D. G. Magnon-phonon coupling in the spin-ladder compound $Ca_9La_5Cu_{24}O_{41}$ measured by time-domain thermoreflectance. *Phys. Rev. B* **89,** 024422 (2014).
88. Boona, S. R. & Heremans, J. P. Magnon thermal mean free path in yttrium iron garnet. *Phys. Rev. B* **90,** 064421 (2014).
89. Hohenberg, P. & Kohn, W. Inhomogeneous Electron Gas. *Phys. Rev.* **136,** B864–B871 (1964).
90. Kohn, W. & Sham, L. J. Self-Consistent Equations Including Exchange and Correlation Effects. *Phys. Rev.* **140,** A1133–A1138 (1965).
91. Economou, E. N. *Green's Functions in Quantum Physics.* (Springer, 2006).
92. Sheng, P. *Introduction to Wave Scattering, Localization, and Mesoscopic Phenomena.* (Academic Press, 1995).
93. Datta, S. *Electronic Transport in Mesoscopic Systems.* (Cambridge University Press, 1997).
94. Tian, Z., Esfarjani, K. & Chen, G. Enhancing phonon transmission across a Si/Ge interface by atomic roughness: First-principles study with the Green's function method. *Phys. Rev. B* **86,** 235304 (2012).
95. Luckyanova, M. N. *et al.* Coherent Phonon Heat Conduction in Superlattices. *Science* **338,** 936–939 (2012).
96. Tian, Z., Esfarjani, K. & Chen, G. Green's function studies of phonon transport across Si/Ge superlattices. *Phys. Rev. B* **89,** 235307 (2014).
97. Huang, K. *Statistical Mechanics, 2nd Edition.* (Wiley, 1987).
98. Kadar, M. *Statistical Physics of Particles.* (Cambridge University Press, 2007).
99. Lee, S., Broido, D., Esfarjani, K. & Chen, G. Hydrodynamic phonon transport in suspended graphene. *Nat. Commun.* **6,** (2015).
100. Levine, I. *Quantum Chemistry.* (Prentice Hall, 2013).
101. Martin, R. *Electronic Structure: Basic Theory and Practical Methods.* (Cambridge University Press, 2008).
102. Bachelet, G. B., Hamann, D. R. & Schlüter, M. Pseudopotentials that work: From H to Pu. *Phys. Rev. B* **26,** 4199–4228 (1982).
103. Giannozzi, P. *et al.* QUANTUM ESPRESSO: a modular and open-source software project for quantum simulations of materials. *J. Phys. Condens. Matter* **21,** 395502 (2009).

104. Noffsinger, J. *et al.* EPW: A program for calculating the electron–phonon coupling using maximally localized Wannier functions. *Comput. Phys. Commun.* **181,** 2140–2148 (2010).
105. Esfarjani, K. & Stokes, H. T. Method to extract anharmonic force constants from first principles calculations. *Phys. Rev. B* **77,** 144112 (2008).
106. Baroni, S., de Gironcoli, S., Dal Corso, A. & Giannozzi, P. Phonons and related crystal properties from density-functional perturbation theory. *Rev. Mod. Phys.* **73,** 515–562 (2001).
107. Born, M. & Huang, K. *Dynamical Theory of Crystal Lattices.* (Clarendon Press, 1998).
108. Zhou, J., Liao, B. & Chen, G. First-principles calculations of thermal, electrical, and thermoelectric transport properties of semiconductors. *Semicond. Sci. Technol.* **31,** 043001 (2016).
109. Shankar, R. *Principles of Quantum Mechanics.* (Springer, 1994).
110. Ziman, J. M. *Electrons and Phonons: The Theory of Transport Phenomena in Solids.* (Clarendon Press, 1960).
111. Born, M. & Oppenheimer, R. Zur Quantentheorie der Molekeln. *Ann. Phys.* **389,** 457–484 (1927).
112. Bloch, F. Über die Quantenmechanik der Elektronen in Kristallgittern. *Z. Für Phys.* **52,** 555–600 (1929).
113. Bardeen, J., Cooper, L. N. & Schrieffer, J. R. Theory of Superconductivity. *Phys. Rev.* **108,** 1175–1204 (1957).
114. Marzari, N., Mostofi, A. A., Yates, J. R., Souza, I. & Vanderbilt, D. Maximally localized Wannier functions: Theory and applications. *Rev. Mod. Phys.* **84,** 1419–1475 (2012).
115. Marzari, N. & Vanderbilt, D. Maximally localized generalized Wannier functions for composite energy bands. *Phys. Rev. B* **56,** 12847–12865 (1997).
116. Giustino, F., Cohen, M. L. & Louie, S. G. Electron-phonon interaction using Wannier functions. *Phys. Rev. B* **76,** 165108 (2007).
117. Lambin, P. & Vigneron, J. P. Computation of crystal Green's functions in the complex-energy plane with the use of the analytical tetrahedron method. *Phys. Rev. B* **29,** 3430–3437 (1984).
118. Ashraff, J. A. & Loly, P. D. The triangular linear analytic method for two-dimensional spectral functions. *J. Phys. C Solid State Phys.* **20,** 4823 (1987).
119. Holstein, T. & Primakoff, H. Field Dependence of the Intrinsic Domain Magnetization of a Ferromagnet. *Phys. Rev.* **58,** 1098–1113 (1940).
120. Demokritov, S. O. *et al.* Bose–Einstein condensation of quasi-equilibrium magnons at room temperature under pumping. *Nature* **443,** 430–433 (2006).
121. Goldsmid, H. J. *Thermoelectric refrigeration.* (Plenum Press, 1964).
122. Zebarjadi, M., Esfarjani, K., Dresselhaus, M. S., Ren, Z. F. & Chen, G. Perspectives on thermoelectrics: from fundamentals to device applications. *Energy Environ. Sci.* **5,** 5147–5162 (2012).
123. Minnich, A. J., Dresselhaus, M. S., Ren, Z. F. & Chen, G. Bulk nanostructured thermoelectric materials: current research and future prospects. *Energy Environ. Sci.* **2,** 466–479 (2009).

124. Sootsman, J. R., Chung, D. Y. & Kanatzidis, M. G. New and Old Concepts in Thermoelectric Materials. *Angew. Chem. Int. Ed.* **48,** 8616–8639 (2009).
125. Snyder, G. J. & Toberer, E. S. Complex thermoelectric materials. *Nat. Mater.* **7,** 105–114 (2008).
126. Dresselhaus, M. S. *et al.* New composite thermoelectric materials for energy harvesting applications. *JOM* **61,** 86–90 (2009).
127. Bentien, A., Johnsen, S., Madsen, G. K. H., Iversen, B. B. & Steglich, F. Colossal Seebeck coefficient in strongly correlated semiconductor $FeSb_2$. *Europhys. Lett.* **80,** 17008 (2007).
128. Zhao, H. *et al.* Dramatic thermal conductivity reduction by nanostructures for large increase in thermoelectric figure-of-merit of $FeSb_2$. *Appl. Phys. Lett.* **99,** 163101–3 (2011).
129. Zhao, H. *et al.* Figure-of-merit enhancement in nanostructured $FeSb_{2-x}Ag_x$ with Ag1−ySby nanoinclusions. *Nanotechnology* **23,** 505402 (2012).
130. Sun, P., Oeschler, N., Johnsen, S., Iversen, B. B. & Steglich, F. $FeSb_2$: Prototype of huge electron-diffusion thermoelectricity. *Phys. Rev. B* **79,** 153308 (2009).
131. Sun, P., Oeschler, N., Johnsen, S., Iversen, B. B. & Steglich, F. Narrow band gap and enhanced thermoelectricity in $FeSb_2$. *Dalton Trans.* **39,** 1012–1019 (2010).
132. Sun, P. *et al.* Unchanged thermopower enhancement at the semiconductor-metal transition in correlated $FeSb_{2-x}Te_x$. *Appl. Phys. Lett.* **98,** 072105–3 (2011).
133. Mani, A., Janaki, J., Satya, A. T., Kumary, T. G. & Bharathi, A. The pressure induced insulator to metal transition in $FeSb_2$. *J. Phys. Condens. Matter* **24,** 075601 (2012).
134. Sun, Y. *et al.* Orientation control and thermoelectric properties of $FeSb_2$ films. *J. Phys. Appl. Phys.* **43,** 205402 (2010).
135. Koirala, M. *et al.* Thermoelectric property enhancement by Cu nanoparticles in nanostructured $FeSb_2$. *Appl. Phys. Lett.* **102,** 213111–5 (2013).
136. Petrovic, C. *et al.* Kondo insulator description of spin state transition in $FeSb_2$. *Phys. Rev. B* **72,** 045103 (2005).
137. Perucchi, A., Degiorgi, L., Hu, R., Petrovic, C. & Mitrović, V. F. Optical investigation of the metal-insulator transition in $FeSb_2$. *Eur. Phys. J. B* **54,** 175–183 (2006).
138. Bentien, A., Madsen, G. K. H., Johnsen, S. & Iversen, B. B. Experimental and theoretical investigations of strongly correlated $FeSb_{2-x}Sn_x$. *Phys. Rev. B* **74,** 205105 (2006).
139. Aeppli, G. & Fisk, Z. Kondo Insulators. *Comments Condens. Matter Phys.* **16,** 155 (1992).
140. Riseborough, P. S. Heavy fermion semiconductors. *Adv. Phys.* **49,** 257–320 (2000).
141. Mahan, G. D. in *Solid State Physics* (eds. Ehrenreich, H. & Spaepen, F.) **51,** 81–157 (Academic Press, 1997).
142. Zhang, Y., Dresselhaus, M. S., Shi, Y., Ren, Z. & Chen, G. High Thermoelectric Figure-of-Merit in Kondo Insulator Nanowires at Low Temperatures. *Nano Lett.* **11,** 1166–1170 (2011).

143. Tomczak, J. M., Haule, K., Miyake, T., Georges, A. & Kotliar, G. Thermopower of correlated semiconductors: Application to $FeAs_2$ and $FeSb_2$. *Phys. Rev. B* **82,** 085104 (2010).
144. Pokharel, M. *et al.* Phonon Drag Effect in Nanocomposite $FeSb_2$. *MRS Commun.* **3,** 31–36 (2013).
145. Pokharel, M. *et al.* Thermoelectric Properties of Bi-$FeSb_2$ Nanocomposites: Evidence for Phonon-Drag Effect. *MRS Online Proc. Libr.* **1490,** 115–120 (2013).
146. Lazarević, N. *et al.* Lattice dynamics of $FeSb_2$. *J. Phys. Condens. Matter* **24,** 255402 (2012).
147. Diakhate, M. S. *et al.* Thermodynamic, thermoelectric, and magnetic properties of $FeSb_2$: A combined first-principles and experimental study. *Phys. Rev. B* **84,** 125210 (2011).
148. Perdew, J. P. & Zunger, A. Self-interaction correction to density-functional approximations for many-electron systems. *Phys. Rev. B* **23,** 5048–5079 (1981).
149. Wallace, D. C. *Thermodynamics of crystals.* (Wiley, 1972).
150. Shiomi, J., Esfarjani, K. & Chen, G. Thermal conductivity of half-Heusler compounds from first-principles calculations. *Phys. Rev. B* **84,** 104302 (2011).
151. Casimir, H. B. G. Note on the conduction of heat in crystals. *Physica* **5,** 495–500 (1938).
152. Klemens, P. G. The Scattering of Low-Frequency Lattice Waves by Static Imperfections. *Proc. Phys. Soc. Sect. A* **68,** 1113 (1955).
153. Tian, Z., Esfarjani, K., Shiomi, J., Henry, A. S. & Chen, G. On the importance of optical phonons to thermal conductivity in nanostructures. *Appl. Phys. Lett.* **99,** 053122–053122–3 (2011).
154. Dresselhaus, M. S. *et al.* New Directions for Low-Dimensional Thermoelectric Materials. *Adv. Mater.* **19,** 1043–1053 (2007).
155. Hochbaum, A. I. *et al.* Enhanced thermoelectric performance of rough silicon nanowires. *Nature* **451,** 163–167 (2008).
156. Novoselov, K. S. *et al.* Electric Field Effect in Atomically Thin Carbon Films. *Science* **306,** 666–669 (2004).
157. Zuev, Y. M., Chang, W. & Kim, P. Thermoelectric and Magnetothermoelectric Transport Measurements of Graphene. *Phys. Rev. Lett.* **102,** 096807 (2009).
158. Wei, P., Bao, W., Pu, Y., Lau, C. N. & Shi, J. Anomalous Thermoelectric Transport of Dirac Particles in Graphene. *Phys. Rev. Lett.* **102,** 166808 (2009).
159. Wang, C.-R. *et al.* Enhanced Thermoelectric Power in Dual-Gated Bilayer Graphene. *Phys. Rev. Lett.* **107,** 186602 (2011).
160. Balandin, A. A. *et al.* Superior Thermal Conductivity of Single-Layer Graphene. *Nano Lett.* **8,** 902–907 (2008).
161. Seol, J. H. *et al.* Two-Dimensional Phonon Transport in Supported Graphene. *Science* **328,** 213–216 (2010).
162. Lindsay, L., Broido, D. A. & Mingo, N. Flexural phonons and thermal transport in graphene. *Phys. Rev. B* **82,** 115427 (2010).
163. Kim, J. Y., Lee, J.-H. & Grossman, J. C. Thermal Transport in Functionalized Graphene. *ACS Nano* **6,** 9050–9057 (2012).
164. Sevinçli, H., Sevik, C., Çağın, T. & Cuniberti, G. A bottom-up route to enhance thermoelectric figures of merit in graphene nanoribbons. *Sci. Rep.* **3,** 1228 (2013).

165. Radisavljevic, B., Radenovic, A., Brivio, J., Giacometti, V. & Kis, A. Single-layer MoS2 transistors. *Nat. Nanotechnol.* **6,** 147–150 (2011).
166. Yoon, Y., Ganapathi, K. & Salahuddin, S. How Good Can Monolayer MoS2 Transistors Be? *Nano Lett.* **11,** 3768–3773 (2011).
167. Cahangirov, S., Topsakal, M., Aktürk, E., Şahin, H. & Ciraci, S. Two- and One-Dimensional Honeycomb Structures of Silicon and Germanium. *Phys. Rev. Lett.* **102,** 236804 (2009).
168. Tsai, W.-F. *et al.* Gated silicene as a tunable source of nearly 100% spin-polarized electrons. *Nat. Commun.* **4,** 1500 (2013).
169. Liu, H. *et al.* Phosphorene: An Unexplored 2D Semiconductor with a High Hole Mobility. *ACS Nano* **8,** 4033–4041 (2014).
170. Li, L. *et al.* Black phosphorus field-effect transistors. *Nat. Nanotechnol.* **9,** 372–377 (2014).
171. Xia, F., Wang, H. & Jia, Y. Rediscovering black phosphorus as an anisotropic layered material for optoelectronics and electronics. *Nat. Commun.* **5,** 4458 (2014).
172. Low, T., Engel, M., Steiner, M. & Avouris, P. Origin of photoresponse in black phosphorus phototransistors. *Phys. Rev. B* **90,** 081408 (2014).
173. Engel, M., Steiner, M. & Avouris, P. Black Phosphorus Photodetector for Multispectral, High-Resolution Imaging. *Nano Lett.* **14,** 6414–6417 (2014).
174. Wang, H. *et al.* Black Phosphorus Radio-Frequency Transistors. *Nano Lett.* **14,** 6424–6429 (2014).
175. Ziletti, A., Carvalho, A., Campbell, D. K., Coker, D. F. & Castro Neto, A. H. Oxygen Defects in Phosphorene. *Phys. Rev. Lett.* **114,** 046801 (2015).
176. Liu, Q., Zhang, X., Abdalla, L. B., Fazzio, A. & Zunger, A. Switching a Normal Insulator into a Topological Insulator via Electric Field with Application to Phosphorene. *Nano Lett.* **15,** 1222 (2015).
177. Asahina, H., Shindo, K. & Morita, A. Electronic Structure of Black Phosphorus in Self-Consistent Pseudopotential Approach. *J. Phys. Soc. Jpn.* **51,** 1193–1199 (1982).
178. Jiang, J.-W. & Park, H. S. Negative poisson's ratio in single-layer black phosphorus. *Nat. Commun.* **5,** 4727 (2014).
179. Fei, R. *et al.* Enhanced Thermoelectric Efficiency via Orthogonal Electrical and Thermal Conductances in Phosphorene. *Nano Lett.* **14,** 6393–6399 (2014).
180. Ramasubramaniam, A. & Muniz, A. R. Ab initio studies of thermodynamic and electronic properties of phosphorene nanoribbons. *Phys. Rev. B* **90,** 085424 (2014).
181. Çakır, D., Sahin, H. & Peeters, F. M. Tuning of the electronic and optical properties of single-layer black phosphorus by strain. *Phys. Rev. B* **90,** 205421 (2014).
182. Elahi, M., Khaliji, K., Tabatabaei, S. M., Pourfath, M. & Asgari, R. Modulation of electronic and mechanical properties of phosphorene through strain. *Phys. Rev. B* **91,** 115412 (2015).
183. Koenig, S. P., Doganov, R. A., Schmidt, H., Neto, A. H. C. & Özyilmaz, B. Electric field effect in ultrathin black phosphorus. *Appl. Phys. Lett.* **104,** 103106 (2014).
184. Xiang, D. *et al.* Surface transfer doping induced effective modulation on ambipolar characteristics of few-layer black phosphorus. *Nat. Commun.* **6,** 6485 (2015).

185. Qiao, J., Kong, X., Hu, Z.-X., Yang, F. & Ji, W. High-mobility transport anisotropy and linear dichroism in few-layer black phosphorus. *Nat. Commun.* **5,** 4475 (2014).
186. Fei, R. & Yang, L. Strain-Engineering the Anisotropic Electrical Conductance of Few-Layer Black Phosphorus. *Nano Lett.* **14,** 2884–2889 (2014).
187. Morgan Stewart, H., Shevlin, S. A., Catlow, C. R. A. & Guo, Z. X. Compressive Straining of Bilayer Phosphorene Leads to Extraordinary Electron Mobility at a New Conduction Band Edge. *Nano Lett.* **15,** 2006–2010 (2015).
188. Qin, G. *et al.* Anisotropic intrinsic lattice thermal conductivity of phosphorene from first principles. *Phys. Chem. Chem. Phys.* **17,** 4854–4858 (2015).
189. Jain, A. & McGaughey, A. J. H. Strongly anisotropic in-plane thermal transport in single-layer black phosphorene. *Sci. Rep.* **5,** (2015).
190. Perdew, J. P. & Wang, Y. Accurate and simple analytic representation of the electron-gas correlation energy. *Phys. Rev. B* **45,** 13244–13249 (1992).
191. Park, C.-H., Giustino, F., Cohen, M. L. & Louie, S. G. Velocity Renormalization and Carrier Lifetime in Graphene from the Electron-Phonon Interaction. *Phys. Rev. Lett.* **99,** 086804 (2007).
192. Park, C.-H. *et al.* Electron–Phonon Interactions and the Intrinsic Electrical Resistivity of Graphene. *Nano Lett.* **14,** 1113–1119 (2014).
193. Parker, D., Chen, X. & Singh, D. J. High Three-Dimensional Thermoelectric Performance from Low-Dimensional Bands. *Phys. Rev. Lett.* **110,** 146601 (2013).
194. Castro, E. V. *et al.* Limits on Charge Carrier Mobility in Suspended Graphene due to Flexural Phonons. *Phys. Rev. Lett.* **105,** 266601 (2010).
195. Sze, S. M. & Ng, K. K. *Physics of Semiconductor Devices.* (Wiley-Interscience, 2006).
196. Uher, C. in *Thermal Conductivity* (ed. Tritt, T. M.) 21–91 (Springer US, 2004).
197. Sommerfeld, A. & Bethe, H. in *Handbuch der Physik* **24, Part 2,** 33 (Springer, 1933).
198. Makinson, R. E. B. The thermal conductivity of metals. *Math. Proc. Camb. Philos. Soc.* **34,** 474–497 (1938).
199. Klemens, P. The Lattice Component of the Thermal Conductivity of Metals and Alloys. *Aust. J. Phys.* **7,** 57–63 (1954).
200. Ziman, J. M. XVII. The effect of free electrons on lattice conduction. *Philos. Mag.* **1,** 191–198 (1956).
201. Ziman, J. M. The effect of free electrons on lattice conduction. *Philos. Mag.* **2,** 292–292 (1957).
202. Asheghi, M., Kurabayashi, K., Kasnavi, R. & Goodson, K. E. Thermal conduction in doped single-crystal silicon films. *J. Appl. Phys.* **91,** 5079–5088 (2002).
203. Ma, Y. *et al.* Enhanced Thermoelectric Figure-of-Merit in p-Type Nanostructured Bismuth Antimony Tellurium Alloys Made from Elemental Chunks. *Nano Lett.* **8,** 2580–2584 (2008).
204. Wang, X. W. *et al.* Enhanced thermoelectric figure of merit in nanostructured n-type silicon germanium bulk alloy. *Appl. Phys. Lett.* **93,** 193121 (2008).
205. Vining, C. B. A model for the high-temperature transport properties of heavily doped n-type silicon-germanium alloys. *J. Appl. Phys.* **69,** 331–341 (1991).

206. Bentien, A. *et al.* Thermal conductivity of thermoelectric clathrates. *Phys. Rev. B* **69,** 045107 (2004).
207. Bentien, A., Pacheco, V., Paschen, S., Grin, Y. & Steglich, F. Transport properties of composition tuned α- and β-$Eu_8Ga_{16-x}Ge_{30+x}$. *Phys. Rev. B* **71,** 165206 (2005).
208. Bentien, A., Johnsen, S. & Iversen, B. B. Strong phonon charge carrier coupling in thermoelectric clathrates. *Phys. Rev. B* **73,** 094301 (2006).
209. Kim, W. *et al.* Cross-plane lattice and electronic thermal conductivities of ErAs:InGaAs/InGaAlAs superlattices. *Appl. Phys. Lett.* **88,** 242107 (2006).
210. Hao, Q. *et al.* Theoretical studies on the thermoelectric figure of merit of nanograined bulk silicon. *Appl. Phys. Lett.* **97,** 063109 (2010).
211. May, A. F., Flage-Larsen, E. & Snyder, G. J. Electron and phonon scattering in the high-temperature thermoelectric $La_3Te_{4-z}M_z$ (M=Sb,Bi). *Phys. Rev. B* **81,** 125205 (2010).
212. Martinez, J. A., Provencio, P. P., Picraux, S. T., Sullivan, J. P. & Swartzentruber, B. S. Enhanced thermoelectric figure of merit in SiGe alloy nanowires by boundary and hole-phonon scattering. *J. Appl. Phys.* **110,** 074317 (2011).
213. Allen, P. B. & Mitrović, B. in *Solid State Physics* (ed. Henry Ehrenreich, F. S. and D. T.) **37,** 1–92 (Academic Press, 1983).
214. Sjakste, J., Vast, N. & Tyuterev, V. Ab initio Method for Calculating Electron-Phonon Scattering Times in Semiconductors: Application to GaAs and GaP. *Phys. Rev. Lett.* **99,** 236405 (2007).
215. Tyuterev, V. G., Obukhov, S. V., Vast, N. & Sjakste, J. Ab initio calculation of electron-phonon scattering time in germanium. *Phys. Rev. B* **84,** 035201 (2011).
216. Wang, Z. *et al.* Thermoelectric transport properties of silicon: Toward an ab initio approach. *Phys. Rev. B* **83,** 205208 (2011).
217. Perdew, J. P., Burke, K. & Ernzerhof, M. Generalized Gradient Approximation Made Simple. *Phys. Rev. Lett.* **77,** 3865–3868 (1996).
218. McConnell, A., Uma, S. & Goodson, K. E. Thermal conductivity of doped polysilicon layers. *J. Microelectromechanical Syst.* **10,** 360–369 (2001).
219. Chapman, P. W., Tufte, O. N., Zook, J. D. & Long, D. Electrical Properties of Heavily Doped Silicon. *J. Appl. Phys.* **34,** 3291–3295 (1963).
220. Efetov, D. K. & Kim, P. Controlling Electron-Phonon Interactions in Graphene at Ultrahigh Carrier Densities. *Phys. Rev. Lett.* **105,** 256805 (2010).
221. Fujimoto, J. G., Liu, J. M., Ippen, E. P. & Bloembergen, N. Femtosecond Laser Interaction with Metallic Tungsten and Nonequilibrium Electron and Lattice Temperatures. *Phys. Rev. Lett.* **53,** 1837–1840 (1984).
222. Elsayed-Ali, H. E., Norris, T. B., Pessot, M. A. & Mourou, G. A. Time-resolved observation of electron-phonon relaxation in copper. *Phys. Rev. Lett.* **58,** 1212–1215 (1987).
223. Brorson, S. D. *et al.* Femtosecond room-temperature measurement of the electron-phonon coupling constant γ in metallic superconductors. *Phys. Rev. Lett.* **64,** 2172–2175 (1990).
224. Chekalin, S. V. *et al.* Femtosecond spectroscopy of $YBa_2Cu_3O_{7-\delta}$: Electron-phonon-interaction measurement and energy-gap observation. *Phys. Rev. Lett.* **67,** 3860–3863 (1991).

225. Grimvall, G. *The Electron-Phonon Interaction in Metals.* (Elsevier Science Ltd, 1981).
226. Lanzara, A. *et al.* Evidence for ubiquitous strong electron–phonon coupling in high-temperature superconductors. *Nature* **412,** 510–514 (2001).
227. Butler, W. H. & Williams, R. K. Electron-phonon interaction and lattice thermal conductivity. *Phys. Rev. B* **18,** 6483–6494 (1978).
228. Huang, Q. *et al.* Tunnelling evidence for predominantly electron–phonon coupling in superconducting $Ba_{1-x}K_xBiO_3$ and $Nd_{2-x}Ce_xCuO_{4-y}$. *Nature* **347,** 369–372 (1990).
229. Carruthers, J. A., Geballe, T. H., Rosenberg, H. M. & Ziman, J. M. The Thermal Conductivity of Germanium and Silicon between 2 and 300 degrees K. *Proc. R. Soc. Lond. Ser. Math. Phys. Sci.* **238,** 502–514 (1957).
230. Holland, M. G. Phonon Scattering in Semiconductors From Thermal Conductivity Studies. *Phys. Rev.* **134,** A471–A480 (1964).
231. Steigmeier, E. F. & Abeles, B. Scattering of Phonons by Electrons in Germanium-Silicon Alloys. *Phys. Rev.* **136,** A1149–A1155 (1964).
232. Goff, J. F. & Pearlman, N. Thermal Transport Properties of n-Type Ge at Low Temperatures. *Phys. Rev.* **140,** A2151–A2169 (1965).
233. Gaur, N. K. S. & Verma, G. S. Phonon-Electron Scattering in n-Type Ge at Low Temperatures. *Phys. Rev.* **159,** 610–624 (1967).
234. Poujade, A. M. & Albany, H. J. Carrier-Concentration Dependence of Electron-Phonon Scattering in Te-Doped GaSb at Low Temperature. *Phys. Rev.* **182,** 802–807 (1969).
235. Crosby, C. R. & Grenier, C. G. Thermal Conductivity of Heavily Doped p-Type InSb at Liquid-Helium Temperatures. *Phys. Rev. B* **4,** 1258–1266 (1971).
236. Sharma, P. C. & Verma, G. S. Electron-Phonon Scattering in Te-Doped GaSb at Low Temperatures. *Phys. Rev. B* **4,** 498–502 (1971).
237. Sood, K. C. & Verma, G. S. Phonon-Electron Scattering in Phosphorus-Doped Germanium. *Phys. Rev. B* **5,** 3165–3170 (1972).
238. Singh, M. & Verma, G. S. Scattering of Phonons by Bound and Free Electrons in Sb-Doped Ge in the Temperature Range 6-80 °K. *Phys. Rev. B* **7,** 2626–2629 (1973).
239. Singh, M. Effect of hole-phonon interaction on the phonon conductivity of highly doped mercury telluride. *Phys. Rev. B* **23,** 2983–2987 (1981).
240. Sota, T., Suzuki, K. & Fortier, D. Low-temperature thermal conductivity of heavily doped n-type Ge. *Phys. Rev. B* **31,** 7947–7952 (1985).
241. Morelli, D. T., Heremans, J. P., Beetz, C. P., Yoo, W. S. & Matsunami, H. Phonon-electron scattering in single crystal silicon carbide. *Appl. Phys. Lett.* **63,** 3143–3145 (1993).
242. Bansal, D. *et al.* Electron-phonon coupling and thermal transport in the thermoelectric compound $Mo_3Sb_{7-x}Te_x$. *Phys. Rev. B* **92,** 214301 (2015).
243. Liao, B. *et al.* Significant reduction of lattice thermal conductivity by electron-phonon interaction in silicon with high carrier concentrations: a first-principles study. *Phys. Rev. Lett.* (2015).
244. Daly, B. C., Kang, K., Wang, Y. & Cahill, D. G. Picosecond ultrasonic measurements of attenuation of longitudinal acoustic phonons in silicon. *Phys. Rev. B* **80,** 174112 (2009).

245. Maznev, A. A. *et al.* Lifetime of sub-THz coherent acoustic phonons in a GaAs-AlAs superlattice. *Appl. Phys. Lett.* **102,** 041901 (2013).
246. Maznev, A. A., Hofmann, F., Cuffe, J., Eliason, J. K. & Nelson, K. A. Lifetime of high-order thickness resonances of thin silicon membranes. *Ultrasonics* **56,** 116–121 (2015).
247. Callen, H. B. *Thermodynamics and an introduction to thermostatistics.* (Wiley, 1985).
248. Johnson, M. & Silsbee, R. H. Thermodynamic analysis of interfacial transport and of the thermomagnetoelectric system. *Phys. Rev. B* **35,** 4959–4972 (1987).
249. Saslow, W. M. Spin pumping of current in non-uniform conducting magnets. *Phys. Rev. B* **76,** 184434 (2007).
250. Saslow, W. M. & Rivkin, K. Irreversible thermodynamics of non-uniform insulating ferromagnets. *J. Magn. Magn. Mater.* **320,** 2622–2628 (2008).
251. Sears, M. R. & Saslow, W. M. Thermal equilibration and thermally induced spin currents in a thin-film ferromagnet on a substrate. *Phys. Rev. B* **85,** 035446 (2012).
252. Kovalev, A. A. & Tserkovnyak, Y. Thermomagnonic spin transfer and Peltier effects in insulating magnets. *EPL Europhys. Lett.* **97,** 67002 (2012).
253. Stancil, D. D. & Prabhakar, A. *Spin waves theory and applications.* (Springer, 2009).
254. Kajiwara, Y. *et al.* Transmission of electrical signals by spin-wave interconversion in a magnetic insulator. *Nature* **464,** 262–266 (2010).
255. Hoffman, S., Sato, K. & Tserkovnyak, Y. Landau-Lifshitz theory of the longitudinal spin Seebeck effect. *Phys. Rev. B* **88,** 064408 (2013).
256. Sanders, D. J. & Walton, D. Effect of magnon-phonon thermal relaxation on heat transport by magnons. *Phys. Rev. B* **15,** 1489–1494 (1977).
257. Schreier, M. *et al.* Magnon, phonon, and electron temperature profiles and the spin Seebeck effect in magnetic insulator/normal metal hybrid structures. *Phys. Rev. B* **88,** 094410 (2013).
258. Montagnese, M. *et al.* Phonon-Magnon Interaction in Low Dimensional Quantum Magnets Observed by Dynamic Heat Transport Measurements. *Phys. Rev. Lett.* **110,** 147206 (2013).
259. Agrawal, M. *et al.* Direct Measurement of Magnon Temperature: New Insight into Magnon-Phonon Coupling in Magnetic Insulators. *Phys. Rev. Lett.* **111,** 107204 (2013).
260. Chen, G. Potential-step amplified nonequilibrium thermal-electric converters. *J. Appl. Phys.* **97,** 083707 (2005).
261. Wilson, R. B., Feser, J. P., Hohensee, G. T. & Cahill, D. G. Two-channel model for nonequilibrium thermal transport in pump-probe experiments. *Phys. Rev. B* **88,** 144305 (2013).
262. Meier, F. & Loss, D. Magnetization Transport and Quantized Spin Conductance. *Phys. Rev. Lett.* **90,** 167204 (2003).
263. Forster, D. *Hydrodynamic Fluctuations, Broken Symmetry, And Correlation Functions.* (Westview Press, 1995).
264. Castella, H., Zotos, X. & Prelovšek, P. Integrability and Ideal Conductance at Finite Temperatures. *Phys. Rev. Lett.* **74,** 972–975 (1995).

265. Zotos, X. Finite Temperature Drude Weight of the One-Dimensional Spin-1/2 Heisenberg Model. *Phys. Rev. Lett.* **82,** 1764–1767 (1999).
266. Slonczewski, J. C. Conductance and exchange coupling of two ferromagnets separated by a tunneling barrier. *Phys. Rev. B* **39,** 6995–7002 (1989).
267. Alvarez, J. V. & Gros, C. Low-Temperature Transport in Heisenberg Chains. *Phys. Rev. Lett.* **88,** 077203 (2002).
268. Kosevich, Y. A. & Gann, V. V. Magnon localization and Bloch oscillations in finite Heisenberg spin chains in an inhomogeneous magnetic field. *J. Phys. Condens. Matter* **25,** 246002 (2013).
269. Dyson, F. J. General Theory of Spin-Wave Interactions. *Phys. Rev.* **102,** 1217–1230 (1956).
270. Sinha, K. P. & Upadhyaya, U. N. Phonon-Magnon Interaction in Magnetic Crystals. *Phys. Rev.* **127,** 432–439 (1962).
271. Callaway, J. & Boyd, R. Scattering of Spin Waves by Magnetic Defects. *Phys. Rev.* **134,** A1655–A1662 (1964).
272. Kittel, C. *Elementary statistical physics.* (Wiley, 1961).
273. Harris, A. B. & Meyer, H. Calorimetric Determination of Energy Levels in Rare-Earth and Yttrium-Iron Garnets. *Phys. Rev.* **127,** 101–118 (1962).
274. Douglass, R. L. Spin-Wave Spectrum of Yttrium Iron Garnet. *Phys Rev* **120,** 1612–1614 (1960).
275. Douglass, R. L. Heat Transport by Spin Waves in Yttrium Iron Garnet. *Phys. Rev.* **129,** 1132–1135 (1963).
276. Guillot, M., Tchéou, F., Marchand, A., Feldmann, P. & Lagnier, R. Specific heat in Erbium and Yttrium Iron garnet crystals. *Z. Für Phys. B Condens. Matter* **44,** 53–57 (1981).
277. Roschewsky, N. *et al. Time resolved spin Seebeck effect experiments as a probe of magnon-phonon thermalization time.* (2013).
278. Spencer, E. G. & LeCraw, R. C. Spin-Lattice Relaxation in Yttrium Iron Garnet. *Phys. Rev. Lett.* **4,** 130–131 (1960).
279. Spencer, E. G. & LeCraw, R. C. Ferromagnetic relaxation in yttrium-iron garnet and the relation to applications. *Proc. IEE - Part B Electron. Commun. Eng.* **109,** 66–70 (1962).
280. C. Vittoria, P. Lubitz, P. Hansen & W. Tolksdorf. FMR linewidth measurements in bismuth-substituted YIG. *J. Appl. Phys.* **57,** 3699–3700
281. Tishin, A. M. & Spichkin, Y. I. *The magnetocaloric effect and its applications.* (Institute of Physics Pub., 2003).